# INAUGURAL – DISSERTATION

zur
Erlangung der Doktorwürde
der
Naturwissenschaftlich - Mathematischen Gesamtfakultät
der
Ruprecht - Karls - Universität
Heidelberg

vorgelegt von
Martin Schmidt, MSci
aus Berlin

Tag der mündlichen Prüfung: 31. Oktober 2007

# Exploring synthetic and biological polymer composites with polarization-modulated mid-infrared synchrotron radiation

Gutachter: Prof. Dr. Michael Grunze
Prof. Dr. Joachim P. Spatz

# Abstract

The innovative application of physical methods is required in order to gain comprehensive qualitative as well as quantitative insights into the structures and the properties of complex materials and systems. In this work, the novel hyphenation of synchrotron-based Fourier-transform infrared microspectroscopy with polarization modulation was implemented. The in this combination so far unique microprobe was designed for the non-destructive *in situ* study of the composition and the structural anisotropy in small or heterogeneous samples. A key feature demonstrated is the ability of the instrument to spatially resolve infrared linear dichroism down to the diffraction limit by using infrared synchrotron radiation. Another characteristic of great potential was shown to be the capability of obtaining orientation information in reference-free measurements. The reference-free and near-diffraction-limited mapping of infrared linear dichroism in fiber-reinforced polypropylene model composites was demonstrated. Measurements on single wood fibers illustrated the capabilities of the method to investigate (bio)polymeric multicomponent and multiphase systems. It was shown that the method can provide new insights into synthetic and biological polymer composites. It is more widely applicable to investigations of complex synthetic and biological materials.

For a complete understanding of the structure and the function of biological macromolecules and complex biological systems it is necessary to measure them in their native environment. Therefore, a microfluidic infrared transmission cuvette for measurements of biological systems in aqueous medium was implemented in this work. This cuvette was used for the *in situ* study of wood polymers in the presence of liquids. Furthermore, it was suitable for the *in situ* measurement of living cells by infrared microspectroscopy. The microfluidic cuvette was shown to be a versatile device which may be used as a miniincubator and an infrared measurement chamber with varied possible further applications.

# Zusammenfassung

Um umfassende qualitative und quantitative Erkenntnisse über die Struktur und Eigenschaften komplexer Materialien und Systeme zu gewinnen, ist der innovative Einsatz physikalischer Methoden gefordert. In der vorliegenden Arbeit wurde eine neuartige Instrumentierung entwickelt und angewendet, die die Polarisationsmodulation mit der Fourier-Transform Infrarotmikrospektroskopie sowie infraroter Synchrotronstrahlung verbindet. Die in dieser Kombination bislang einzigartige Mikrosonde wurde für die zerstörungsfreie In-situ-Untersuchung der Zusammensetzung und Struktur von mikroskopischen oder heterogenen anisotropen Proben entwickelt. Es wurde gezeigt, dass das Instrument durch die Nutzung infraroter Synchrotronstrahlung in der Lage ist, den Lineardichroismus örtlich bis hin zur Beugungsbegrenzung aufzulösen. Es wurde weiterhin veranschaulicht, dass die Fähigkeit, Informationen zur molekularen Ausrichtung in referenzfreien Messungen zu erhalten, von großer Bedeutung ist. Der Lineardichroismus in Polypropylen-Faserverbundstoffen konnte so durch referenzfreies Messen nahe der Beugungsbegrenzung abgebildet werden. Untersuchungen an einzelnen Holzfasern zeigten die Fähigkeit der Methode auf, (bio)polymere Systeme, die aus verschiedenen Bestandteilen und Phasen aufgebaut sind, zu erforschen. Es wurde nachgewiesen, dass die Methode neue Einblicke in künstliche und biologische Verbundstoffe ermöglicht. Ein erweiterter Einsatz der Methode zur Untersuchung komplexer künstlicher und biologischer Materialien ist möglich.

Es ist unerlässlich, biologische Makromoleküle und komplexe biologische Systeme in ihrer natürlichen Umgebung zu untersuchen, um ein vollkommenes Verständnis ihrer Struktur und Funktionen zu gewinnen. Aus diesem Grund wurde in dieser Arbeit eine mikrofluidische Infrarottransmissionsküvette für Messungen an biologischen Systemen in wässrigem Medium entwickelt. Diese Küvette wurde für die In-situ-Untersuchung von Holzpolymeren in Flüssigkeiten verwendet. Es wurde außerdem gezeigt, dass die Küvette für die In-situ-Untersuchung lebender Zellen mittels Infrarotmikrospektroskopie geeignet ist. Die mikrofluidische Küvette ist somit als Mikroinkubator und Infrarotprobenkammer vielseitig einsetzbar.

# Contents

# 1 Introduction

Materials have played a key role in the course of civilization. They have had a profound influence on the evolution of modern human society and they are central to many modern technologies. The development of new structures and devices based on innovative designs of materials will be pivotal for future growth and prosperity.[1] Novel tailored materials are of potential use in industrial, medical, environmental, and many other technological applications. This means that the implications of materials research and science have a broad impact beyond the intellectual merit. Nevertheless, a fundamental understanding is needed in order to be able to control material parameters and to design advanced materials. There are basically four elements to be understood and controlled: the structure and chemical composition; the synthesis and processing; the properties; and the performance of a material. In *Flemings's tetrahedron* these four elements are placed at the tetrahedron's apices to illustrate the interrelationships of the elements with each other (see Figure 1.1).[1,2] Investigations of the relationships between the structural elements of materials and their properties can be particularly instructive, for insights into structure-property correlations may enable one to fashion the characteristics of materials.[3] It should be noted that the structural arrangement of internal components encompasses several levels, essentially spanning the atomic and molecular, nano-, micro-, meso-, and macroscopic length scales. The wide range of length scales makes access to a comprehensive understanding of composition and structure a great challenge.

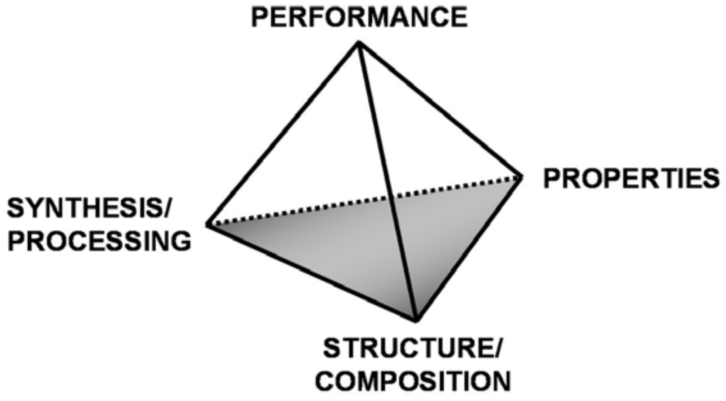

**Figure 1.1.** Flemings's tetrahedron, illustrating the interrelationships of performance, process, structure and properties.

Combining two or more materials can produce an altogether different material. Based on the principle of combined action this material may display a combination of the best characteristics of each of the component materials, or unusual ranges of properties.[3] It is termed a composite material. Prominent members of this family of materials are particle- and fiber-reinforced composites. These multicomponent and multiphase systems consist of a reinforcement material forming the dispersed phase and an embedding matrix. On account of the synergistic effect they are abundantly used in natural as well as man-made or engineered systems. Frequently, polymers are constituents of composites. Indeed, most naturally occurring tissues are built with biopolymeric fibers.[4] Cellulose fibers found in plant cell walls and collagen fibers found in bone, skin, tendon, cornea, or cartilage are two notable examples. Biological materials are often structurally complex composites and show a hierarchical organization from the nanometer to the macroscopic scale.[4-9] Each level of structural organization is being underpinned by the level beneath. The macroscopic material properties eventually emerge from all of the underlying levels. Commonly there is anisotropy, i.e. directionality, in these structures and hence in the properties. A comprehensive understanding of these optimized biological materials requires the exploration of their complex organization. The ability to relate organization to material function is a particularly crucial element. In addition, the study of these systems is relevant also from a technological point of view because it can lead to new materials concepts and design solutions.[7] The application of biotemplating[10] and biomimicry[11,12] in fact seeks to produce optimized materials based on or inspired by biological materials respectively. In order to understand how the properties are governed by the chemical composition and structure it is necessary to examine how a material responds to an imposed stimulus. Analysis of deformation in response to an exerted force can provide correlations of mechanical behaviour and performance with structure.[8] For instance the investigation of a modular elongation in natural adhesives and fibers has provided insights into the molecular mechanistic origin of mechanical properties.[13] Studies on the role of interface polymers in biological fiber composites for tight binding between fibers and matrix are cited as another example.[14]

Single cells are fundamental building blocks of biological tissues. The cellular architecture itself is highly complex and implies the organization of various components and compartments on different hierarchical levels. Cells found in tissues produce and provide the basic materials such as collagen or cellulose, and fulfill more and diverse functions like mechanical sensing and adaptation.[15] The ability of these cells to sense and to respond to external mechanical stimuli from neighbouring cells or from the extracellular matrix is critical for normal cell behaviour.[16] Mechanical forces play a main role in the regulation of cell adhesion and in the organization of the cytoskeleton.[17] The cytoskeleton forms an intracellular scaffold which strongly influences the viscoelasticity of eukaryotic cells and in consequence their shape and behaviour.[18] This scaffold is a macromolecular assembly composed of actin microfilaments, microtubules, intermediate filaments, and their associated proteins. Filamentous actin is significantly involved in cellular processes such as motility, differentiation, proliferation, and in adhesion through the connection with focal adhesion sites.[19] Actin filaments and associated molecules form adaptable viscoelastic structures, including networks and anisotropic stress fiber systems, and they actively respond to stimuli.[15] Biophysical approaches have been applied to gain insights into the organization of these heterogeneous and dynamic structures.[16-23] A very recent study on the phagocytosis, i.e. ingestion, of polystyrene microspheres by single cells presents a further tool to explore the dynamics and rearrangements of the cytoskeleton.[24] Intriguingly, colloidal crystallites were observed which were “engineered” by the cells through assembly of the microspheres. This is a striking example that the explicit study of cell structure and function ultimately requires single living cells. By extracting basic physical parameters, quantitative biophysical methods may hold the key to gain insights into the cytoskeletal polymer dynamics and the organization in these complex composite systems.[15]

In order to gain qualitative as well as quantitative insights into the structures and the properties of single cells, biological tissues and materials, the innovative application of physical methods is required.[5,15] It is crucial to extract information at a variety of levels, including ultrastructural details. In particular, *in situ* investigations on the molecular level pose a major challenge. Fluorescence light, atomic force and electron microscopy techniques, diffraction methods, and spectroscopy can be used in a complementary fashion to characterize complex composite systems. Infrared (IR) spectroscopy probes molecular vibrations. Since the pioneering work of William W. Coblentz it has been used as a chemical as well as a structural diagnostic method.[25] Indeed, it is a powerful tool for the structural and compositional characterization of polymers.[26,27] IR spectroscopy provides a wealth of spectral information on submolecular functional groups in polymeric building blocks and yields insights into the chemical structure and properties of polymeric materials. Importantly, it is a very efficient technique to characterize *in situ* multiphase and multicomponent macromolecular systems.[28] Polarized IR spectroscopy can explore spatial arrangements of local submolecular structures and probe molecular orientation. It therefore offers a means to quantify anisotropy, order and disorder in polymer systems.[26-29]

IR spectroscopy is a non-invasive and non-destructive as well as a label- and stain-free method. It was shown to be a powerful technique for the *in situ* characterization of cellular organisms.[30-34] The emergence in the late 1940s and the resurgence in the early 1980s of IR microspectroscopy have made possible the IR microanalysis of small isolated samples and of localized areas in larger heterogeneous samples by providing spatial resolution.[35-37] In contrast to the source-limited case of conventional thermal sources, diffraction-limited IR microspectroscopy can be performed using synchrotron radiation.[38] Thus, exploiting the high brilliance of the synchrotron source, sensitive measurements with high temporal and spatial resolution have become feasible.[39-43] Synchrotron-based IR microspectroscopy has been applied to synthetic polymer composites,[44,45] bone,[46] plant growth and development,[47] brain tissue,[48] and dried single cells.[49] Importantly, synchrotron-based IR microspectroscopy can be used to measure single living cells in a non-invasive and marker-free fashion,[50-53] and also in conjunction with fluorescence microscopy.[46] It has been shown that infrared synchrotron radiation induces no radiation damage in cells and that it is not cytotoxic.[54,55] Thus, synchrotron-based IR microspectroscopy is a powerful tool for investigations of complex composite systems.

In view of the challenges in the characterization of natural composites identified above, the following aims for this dissertation are inferred. First: to implement a combination of synchrotron-based Fourier-transform IR microspectroscopy with polarization modulation[29,56-58] as a novel microprobe for the non-destructive *in situ* study of small or heterogeneous anisotropic samples. Second: to test the performance and to identify the distinct advantages of this new method. Third: to explore and to exploit the capabilities of the method in studies of synthetic and biological polymer composites. Fourth: to work towards the application of this method to single living cells. The specific goal here is to gain an understanding of the complex cytoskeletal arrangement and dynamics in terms of a basic order parameter derived from the polarized spectroscopic measurements. This last task entails the development of a dedicated microfluidic cuvette with peripheral elements for the simultaneous culturing of cells, probing by IR radiation and observation with visible light under controlled environmental conditions. Moreover, preliminary experiments are required to establish a suitable model system for the *in situ* monitoring by IR spectroscopy of the cytoskeletal response triggered by an external stimulus.

# 2 Theoretical Background

## 2.1 Infrared Radiation

The wave-like description regards electromagnetic radiation as a self-propagating wave in space. In vacuum the electromagnetic wave propagates at a constant speed, i.e. the speed of light, $c$, with the electric field, $\mathbf{E}(z,t)$, and the magnetic field, $\mathbf{B}(z,t)$, oscillating in phase transversely to the propagation direction (the $z$ axis), and mutually perpendicular to one another. This electromagnetic field is characterized by its wavelength, $\lambda$, and its frequency, $\nu$, which are related by $c = \lambda\nu$. When the oscillation of the wave's electric field vector proceeds in one plane the electromagnetic radiation is *linearly polarized* in this polarization plane. Such an electromagnetic wave can be described considering the electric field vector:

$$\mathbf{E}(z,t) = \mathbf{E_0}\cos(2\pi\nu t - \frac{2\pi}{\lambda}z + \phi_0),$$

where $z$ is the position, $t$ is time, $\mathbf{E_0}$ is the amplitude, and $\phi_0$ is an arbitrary phase angle. The particle-like description of electromagnetic radiation introduces packets or quanta of electromagnetic energy called *photons*. The energy, $E$, of each photon is given by the relation $E = h\nu$, where $h$ is Planck's constant. The wavenumber, $\tilde{\nu}$, conventionally used in infrared spectroscopy, is defined as $\tilde{\nu} = 1/\lambda = \nu/c$ and is therefore related to the energy by $E = hc\tilde{\nu}$. Wavenumbers are reported in reciprocal centimetres ($\text{cm}^{-1}$).

The electromagnetic spectrum encompasses, in the order of increasing energy, radio waves, microwaves, terahertz and infrared radiation, visible and ultraviolet light, X-rays, and $\gamma$-rays. As its name suggests infrared radiation, discovered by William Herschel in 1800,[59-61] lies to the low energy end of the visible light. The infrared spectrum covers the wavenumber range from 14300 to 10 $\text{cm}^{-1}$.[62] Specifically, the mid-infrared range stretches from 4000 to 400 $\text{cm}^{-1}$, corresponding to 2.5 to 25 μm when expressed in wavelength, or ~ 0.5 to 0.05 eV in energy.

## 2.2 Sources of Mid-Infrared Radiation

The conventional laboratory source for broadband or polychromatic mid-infrared spectroscopy is a thermal source called globar. It consists of a ceramic SiC rod which is heated by a high current at low voltage and operates at about 1200 to 1500 K. Its emission spectrum resembles that of black-body radiation given by the Planck distribution.[62] The deviation from the ideal black-body behaviour is described by Kirchhoff's law and is due to the fact that the emission factor is smaller than unity. It should be noted that a typical globar rod has a diameter of around 5 to 10 mm and a length of about 20 to 50 mm. This means that the source size and the opening angle or divergence of the produced radiation are considerably large.

Power, defined as photons per time and bandwidth, is an important source characteristic. However, the concept of brilliance is more relevant in cases where the throughput or etendue of an experiment, i.e. the product of area and solid angle, is strongly limited.[39] Such throughput-limited experiments include infrared microspectroscopy and infrared sample geometries with cryostats and high-pressure cells. In the infrared spectral region the signal-to-noise ratio (S/N) is often limited by detector noise.[39,63,64] S/N of a given experiment is the ratio of the source power (SP) over the noise power. SP has the following general expression:[43]

$$\mathrm{SP}(\tilde{\nu}) = B(\tilde{\nu})\Theta\xi\Delta\tilde{\nu},$$

where $B(\tilde{\nu})$ is the source brilliance, $\Theta$ is the limiting experimental throughput, $\xi$ is the optical efficiency of the instrument, and $\Delta\tilde{\nu}$ is the resolution bandwidth. This means that the brilliance, defined as power over source area and solid angle, is a key factor determining the value of S/N. Moreover, the brilliance is at best being conserved in an optical system according to the Helmholtz or Lagrange invariant.[39]

Therefore, infrared synchrotron radiation presents an attractive alternative source of infrared radiation. It can be used to overcome the limited source brilliance of the thermal globar source and to thus enhance the performance of throughput-limited infrared spectroscopy.[38,39] Synchrotron radiation is electromagnetic radiation generated when relativistic charged particles are accelerated by changing their velocity or the direction of their movement, typically by means of magnetic fields. Electron storage rings are facilities providing synchrotron radiation. Here, electrons from an electron gun are accelerated by a linear accelerator and a booster synchrotron to very nearly the speed of light, and then stored in the so-called storage ring at energies usually on the order of GeV. This ultra-high vacuum electron storage ring uses magnetic fields to bend electrons into a closed orbit. Synchrotron radiation is emitted by the relativistic electrons as they transit these magnetic guide structures, i.e. the dipole or bending magnets, due to the transverse acceleration. Such synchrotron radiation emitted from the homogeneous field of a bending magnet is called bending magnet radiation. In contrast to Hertz dipole radiation, the synchrotron radiation is emitted into a narrow cone pointing in the direction of the velocity because of relativistic corrections due to the electrons moving close to the speed of light (see Figure 2.1).[39] The synchrotron light emitted is given by the incoherent superposition of the emission from single electrons. Thus, the intensity of the emitted light is proportional to the number of stored electrons circulating in the storage ring and hence the electron beam current.[39,40] Synchrotron radiation from a storage ring is a calculable absolute source used as a standard for reference and calibration.[64,65]

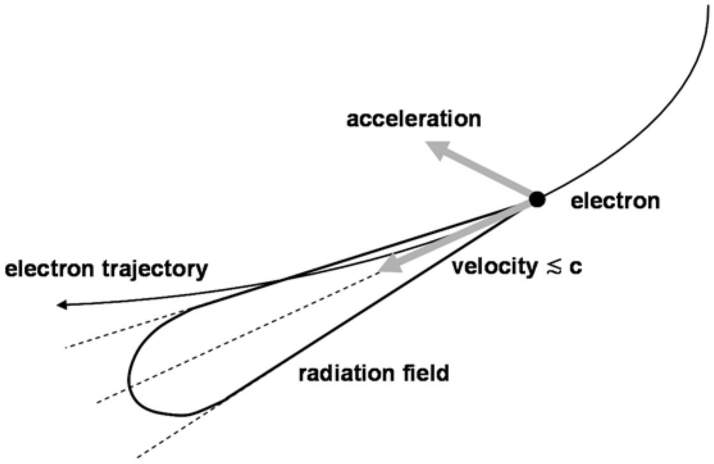

**Figure 2.1.** Schematic of synchrotron radiation produced by a relativistic electron.

In the infrared spectral region the synchrotron radiation source is essentially performing as a diffraction-limited point source.[66-69] The effective source size is on the order of ~ 100 μm.[39,42,43] The natural opening angle, $\theta_{\text{nat}}$, for synchrotron radiation is given by the following equation:[39,64]

$$\theta_{\text{nat}}(\text{rad}) = 1.66\left(\frac{\lambda}{\rho}\right)^{1/3},$$

where $\lambda$ is the wavelength and $\rho$ is the radius of the storage ring. In the infrared spectral region $\theta_{\text{nat}}$ is on the order of tens of milliradians.[64,68] This opening angle or beam divergence is large compared to ultraviolet or X-ray synchrotron radiation, but very small with respect to the thermal globar source. Importantly, in the infrared the synchrotron source is roughly three orders of magnitude more brilliant than the globar source.[39,40] This advantage means that infrared spectroscopy can readily be performed at the diffraction limit using synchrotron radiation.[38,69] It is also important to note that the brilliance advantage is not because the synchrotron produces more power, but because of the small source size and the small opening angle. Consequently, sample heating from infrared synchrotron radiation is minimal (~ 0.5 K) which induces no sample damage or cytotoxicity.[54,55,70] In contrast to brilliant infrared lasers, synchrotron radiation is also broadband. This combination of the broadband nature with the brilliance is of great significance for infrared spectroscopy.[40,69]

As a highly collimated source, synchrotron radiation is ideally suited for coupling with interferometers of Fourier-transform infrared spectrometers[63] and for infrared spectral ellipsometry.[71] It has also well defined polarization characteristics with the light being linearly polarized in the orbit plane and having circular components above and below the orbit plane. In addition to bending magnet radiation, the relativistic electrons emit also the so-called edge radiation produced by the longitudinal velocity change occurring when the electrons enter or exit the dipoles of a storage ring.[39] This radiation was shown to have complex polarization characteristics.[72] Synchrotron radiation has a defined time structure and is pulsed on a sub-nanosecond timescale. This is due to accelerating fields inside the so-called radio-frequency cavity used to restore the energy which is lost by the orbiting electrons through radiation emission. The oscillating fields lead to electron bunching and thus to a pulsed source. This property was exploited for sub-nanosecond time-resolved broadband infrared spectroscopy.[73] It is also worth noting that the electron beam current is a slowly decaying function. This means that also the light intensity decreases with time and therefore needs to be normalized. Moreover, unstable beam orbits can generate noise problems and deteriorate the achievable S/N.[39]

## 2.3 Infrared Spectroscopy

Optical spectroscopy explores the interaction between light and matter. Vibrational spectroscopy involves different methods such as infrared, Raman, coherent anti-Stokes Raman, sum-frequency, high-resolution electron energy loss, and inelastic neutron scattering spectroscopy. Infrared spectroscopy is based on the absorption of infrared radiation leading to the excitation of molecular vibrations. The total energy of a molecule is given by the sum of the translational, rotational, vibrational and electronic energies. A molecule with $N$ atoms has $3N$ degrees of motional freedom, three of which represent translational motion and three represent rotational motion.[74] There are then $3N - 6$ vibrational degrees of freedom ($3N - 5$ for a linear molecule) corresponding to the number of normal vibrations of the molecule. The vibrations of a molecule can be described as linear superpositions of the normal vibrations. The vibrational spectra of molecules result from transitions between quantized vibrational energy states, and they depend on the masses of the atoms, their geometrical arrangement, and the strength of their chemical bonds.[62] They hence contain information on chemical composition and molecular structure.

The simplest model of a vibrating diatomic molecule is a harmonic oscillator obeying Hooke's law. This means the force, $F$, which is necessary to displace the atoms from their equilibrium position by a certain distance, $x$, is proportional to the force constant, $k$:

$$F = -kx.$$

And the potential energy, $V$, of a harmonic oscillator is given by the following parabola:

$$V = \frac{1}{2}kx^2.$$

The quantum mechanical solution for the vibrational energy states, $E_\upsilon$, of the harmonic oscillator is given by the following equation:[62]

$$E_\upsilon = (\upsilon + 1/2)h\nu,$$

where $\upsilon$ is the vibrational quantum number ($\upsilon = 0, 1, 2, \ldots$), $h$ is Planck's constant, and $\nu$ the fundamental frequency of the vibration. By defining the reduced mass, $\mu$, of the diatomic molecule with masses $m_1$ and $m_2$ by:

$$\frac{1}{\mu} = \frac{1}{m_1} + \frac{1}{m_2},$$

$\nu$ can be expressed as follows:

$$\nu = \frac{1}{2\pi}\sqrt{\frac{k}{\mu}}.$$

Quantum theory and quantization lead to discrete energy levels which are equidistant due to the harmonicity. Moreover, it can be seen that the minimum energy, the so-called zero point energy, associated with a molecular vibration is a half quantum, ½ $h\nu$, as due to Heisenberg's uncertainty principle atoms can never be at rest. A molecular vibration is infrared active, i.e. a transition between vibrational energy states due to absorption or emission of infrared radiation is allowed, only if its molecular electric dipole moment, $\boldsymbol{\mu}$, changes during the vibration. Another selection rule of infrared spectroscopy states:

$$\Delta\upsilon = \pm 1.$$

The population of the vibrational energy states at equilibrium is determined by Boltzmann statistics. At room temperature almost all the molecules are in their vibrational ground states initially. This means the fundamental transition 1 ← 0 is the dominant spectral transition. According to the Bohr frequency condition, interaction of infrared radiation with a vibrating molecule occurs only if the electric field vector of the radiation oscillates with the same frequency as the molecular dipole moment. Therefore, the energy difference for the excitation from the vibrational ground state to the vibrational first excited state due to the absorption by infrared radiation is given by:

$$\Delta E = E_1 - E_0 = h\nu_{\text{photon}} = \frac{h}{2\pi}\sqrt{\frac{k}{\mu}}\,.$$

The dependence of the resonance or vibrational frequencies to $k$ and $\mu$ is important for spectroscopy because $k$ directly relates to bond strengths and $\mu$ to the masses of the vibrating atoms. Importantly, the absorption of infrared radiation is dependent on the orientation between the electric field vector of the radiation and the dipole-transition moment vector. This dependence is exploited in polarized infrared spectroscopy and is discussed in Chapter 2.6.

Real molecules are not perfect harmonic oscillators. Especially for large values of the vibrational quantum number or high vibrational excitations the harmonic oscillator is a poor approximation. Therefore, $E_\upsilon$ must be described using an anharmonic or Morse-type potential function:[62,74]

$$E_\upsilon = h\nu(\upsilon + 1/2) - h\nu x_e(\upsilon + 1/2)^2\,,$$

where $x_e$ is the anharmonicity constant. Thus, there are a finite number of bound levels which are no longer equidistant but converge towards high quantum numbers making bond dissociation possible (see Figure 2.2). Anharmonicity also relaxes the selection rule, $\Delta\upsilon = \pm 1$, leading to weakly allowed transitions corresponding to overtones and combination bands.

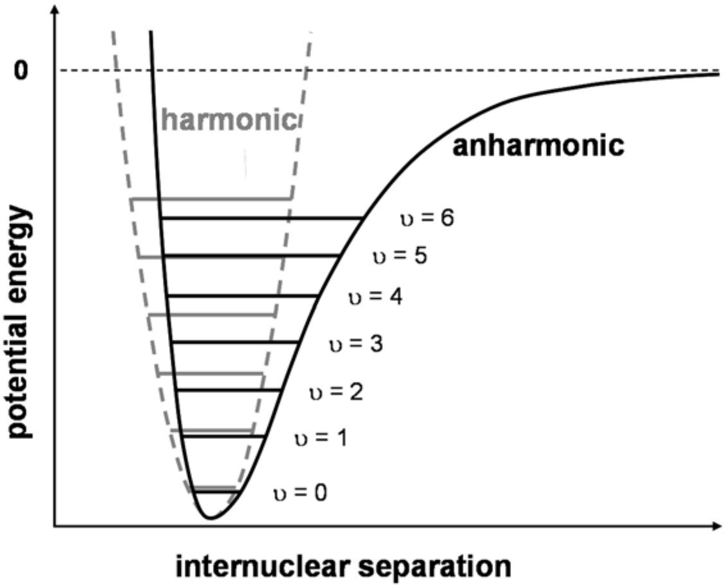

**Figure 2.2.** Plot of the potential energy of a diatomic molecule as a function of the atomic displacement during a vibration for a harmonic oscillator and for an anharmonic oscillator.

More complex molecules may have many bonds, and vibrations can be coupled. There are two main types of vibrations: stretching vibrations which change bond lengths, and bending and torsional vibrations which change bond angles. Vibrations that are primarily localized on a specific bond or functional group exhibit a definite range of frequencies which are characteristic of this bond or functional group. Such vibrational modes which are indicative of chemical functional groups may be employed for the elucidation of the molecular structure. The so-called fingerprint bands involve significant motion of several atoms and are useful to distinguish between different molecules. In fact, the vibrational spectrum of a given molecule is unique and may thus be used to identify that molecule.[63]

Infrared spectroscopy permits quantitative analytical investigations. The transmittance of a sample, $T$, is defined as the ratio of the transmitted light intensity, $I$, to the incident intensity, $I_0$:

$$T = \frac{I}{I_0} .$$

According to the Bouguer-Beer-Lambert law:

$$I = I_0 10^{-\varepsilon c l} ,$$

where $\varepsilon$ is the molar absorption coefficient, $c$ the molar concentration and $l$ the length of the sample. The absorbance of the sample, $A$, is defined as:

$$A = -\log T = -\log \frac{I}{I_0} = \varepsilon c l .$$

Hence, the absorbance is proportional to the concentration and the length or the thickness of the sample. An infrared absorption spectrum of a sample is typically reported as the absorbance as a function of wavenumber.

## 2.4 Fourier-Transform Infrared Spectroscopy

In order to record a spectrum it is necessary to analyze or decompose and to detect the intensities of the spectral frequency components of the radiation. Conventional spectrometers use a dispersing element to separate radiation with different frequencies into different spatial directions and a monochromator to select a narrow band of frequencies for detection. In early infrared spectroscopy prism instruments were used, where frequency separation is based on refraction and dispersion. Around 1950, they were replaced by spectrometers using diffraction gratings.[62] These spectrometers have in turn been superseded by the nowadays prevalent Fourier-transform infrared spectrometers. The invention of the two-beam interferometer by Michelson in the 19th century was an early contribution to the emergence of Fourier-transform infrared spectroscopy.[75] However, the actual conception and realization of this technique is based on seminal works by Fellgett[76,77] and Jacquinot[78,79] in the 1950s. Through the introduction of the fast Fourier-transform algorithm,[80] the digital computer, and small gas lasers the technique reached broad acceptance and utility.

There are three significant advantages associated with Fourier-transform infrared spectroscopy[63] which form the basis for the improved performance over dispersive infrared spectrometers using monochromators:

*Fellgett (multiplex) advantage*: Information from all spectral elements is measured simultaneously. This advantage of spectral multiplexing is particularly significant for infrared spectroscopy where detector noise is usually much higher than the noise from other sources.[62] The multiplex recording contains the detector noise only once and not spectrally selective, independently of the number of spectral channels. It is worth noting here, however, that dispersive spectrometers using focal plane array detectors have been implemented recently.[81-86] In contrast to conventionally used single element detectors, array detectors derived from military missile technology have multiple detector elements. They thus also offer multichannel capabilities by simultaneous detection. These novel spectrometers offer high sensitivity and high temporal resolution (< 100 μs), and may well initiate a renaissance of dispersive spectrometers and a paradigm shift in infrared spectroscopy once more.

*Jacquinot (throughput) advantage*: There is an increased radiative throughput due to the absence of slits. The multiplex and the throughput advantage both provide better S/N or shorter measurement times.

*Connes advantage*: Wavenumber determination is laser-calibrated and therefore highly accurate. This advantage together with the higher achievable S/N permits the measurement of highly accurate difference spectra.

The two-beam interferometer based on Michelson's design is the heart of a Fourier-transform infrared spectrometer since it is the device for analyzing the frequencies present in a composite signal.[87] It consists of a fixed plane mirror, a moving plane mirror and a beamsplitter (see Figure 2.3). The collimated infrared beam from the source is partially transmitted to the moving mirror and partially reflected to the fixed mirror by the beamsplitter. Ideally, the beamsplitter reflects and transmits light equally. The two coherent infrared beams are then reflected back to the beamsplitter by both mirrors. The transmitted beam from the fixed mirror and the reflected beam from the moving mirror then reach the detector simultaneously. The two combined beams interfere constructively or destructively depending on the wavelength of the light and the varying optical path difference or phase difference introduced by the moving mirror. The interferometer hence converts the presence of any particular wavenumber component in the signal into a variation in intensity of the radiation reaching the detector. This variation in the intensity of the beam emerging from the interferometer and passing to the detector as a function of path difference ultimately yields the spectral information in a Fourier-transform spectrometer. The optical path difference is called the retardation, $\delta$, and is given in units of cm.

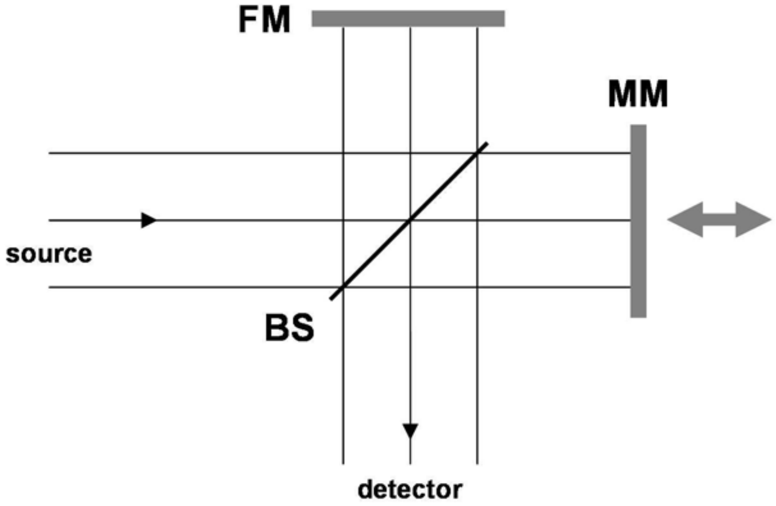

**Figure 2.3.** Schematic diagram of a Michelson interferometer, consisting of three major components: a fixed mirror (FM), a moving mirror (MM) and a beamsplitter (BS).

The detector signal, i.e. the intensity as a function of retardation, $I(\delta)$, is the so-called interferogram. For a monochromatic radiation source the equation representing the interferogram is:[63]

$$I(\delta) = B(\tilde{\nu}) \cos(2\pi\tilde{\nu}\,\delta),$$

where $B(\tilde{\nu})$ is the single-beam spectral intensity. When radiation of more than one wavenumber is emitted by the source the measured interferogram results from the superposition of the interferograms corresponding to each wavenumber. For continuum or broadband spectral sources the interferogram can be represented by the integral:[63]

$$I(\delta) = \int_{-\infty}^{\infty} B(\tilde{\nu}) \cos(2\pi\tilde{\nu}\,\delta) d\tilde{\nu}.$$

$I(\delta)$ is the cosine Fourier transform of $B(\tilde{\nu})$. And $B(\tilde{\nu})$ is given by:

$$B(\tilde{\nu}) = \int_{-\infty}^{\infty} I(\delta)\cos(2\pi\tilde{\nu}\,\delta)d\delta = 2\int_{0}^{\infty} I(\delta)\cos(2\pi\tilde{\nu}\,\delta)d\delta.$$

Therefore, the spectrum, i.e. the variation of intensity with wavenumber, is calculated from the interferogram by computing the Fourier transform of $I(\delta)$, hence also the name of this spectroscopic technique. In practice, the detector signal is digitized and a discrete Fourier transform is used as a digital approximation of the continuous Fourier series. Figure 2.4 shows the interferograms of monochromatic and broadband radiation with their corresponding spectra. At zero optical retardation or at the zero path difference, all the sinusoidal components of the broadband radiation interfere totally constructive, producing the so-called centerburst on the interferogram.

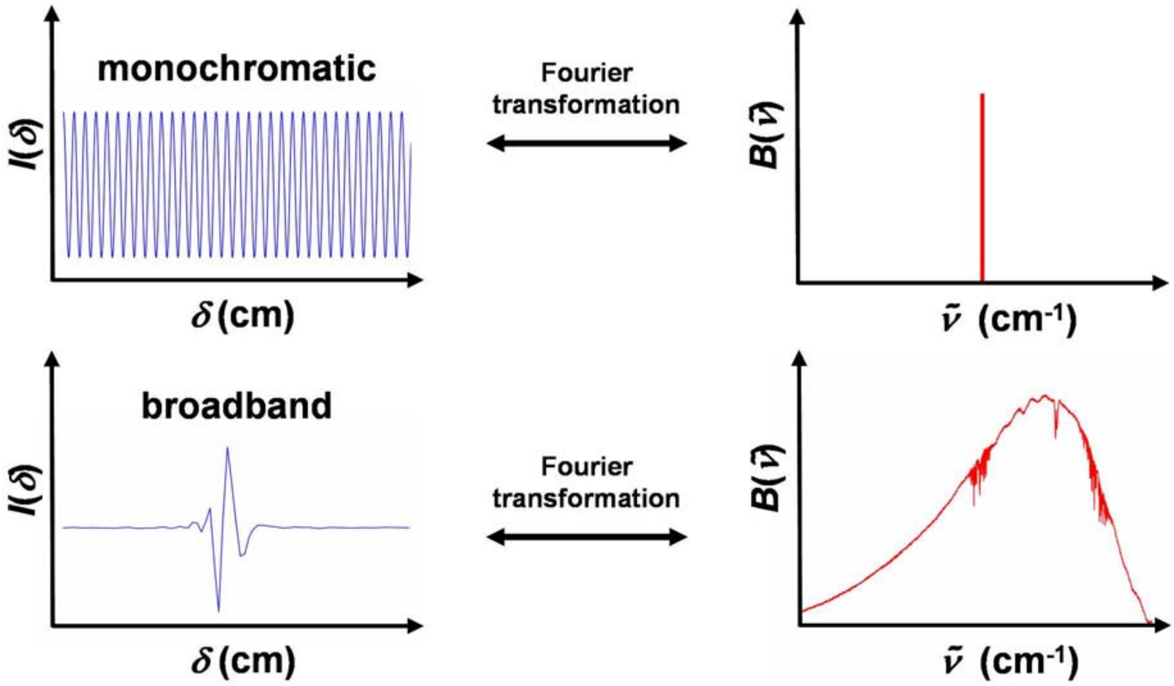

**Figure 2.4.** Schematic representation of interferograms (blue) of monochromatic and broadband radiation with their corresponding spectra (red).

In the continuous rapid-scan mode the moving mirror moves continuously at a constant velocity, $v$. The optical path difference at time $t$ is then given by:

$$\delta = 2vt.$$

The interferogram data points are digitized at the zero crossings of a He-Ne laser signal as the moving mirror is scanned. The laser signal ensures that $I(\delta)$ is measured at precisely equal intervals of mirror positions providing also an internal wavelength calibration. Because of the continuous movement of the mirror the interferogram varies as a function of time. Each wavenumber component is thus modulated according to:[63]

$$f_{\tilde{\nu}} = 2v\tilde{\nu}.$$

These modulation frequencies, $f_{\tilde{\nu}}$, called Fourier frequencies, are in the audio range and can be easily amplified without the need for modulating the beam with a chopper. For the mid-infrared the modulation frequencies are typically in the range of a few kHz. According to the Nyquist criterion, the interferogram must be digitized using a sampling frequency greater than or equal to twice the highest frequency reaching the detector in order to be digitized unambiguously without any loss of information. Given a large centerburst and very small intensity variations well displaced from zero retardation, the dynamic range of interferograms can be large. This means the analog-to-digital converter needs to have a high dynamic range as well to be able to accurately resolve interferograms. It may be necessary to reduce the dynamic range and to suppress the centerburst of an interferogram in order to be able to detect very weak absorption bands. This can for example be achieved through the use of differential spectroscopy where the beam is rapidly modulated between two parent states, e.g. by polarization modulation.[63] To increase S/N of interferograms measured in the rapid-scan mode a method of coherent signal averaging of successive interferograms called coherent addition or coadding is used.[63]

The spectral resolution, $\Delta\tilde{\nu}$, depends inversely on the maximum retardation introduced by the interferometer, $\delta_{\max}$:

$$\Delta\tilde{\nu} = (\delta_{\max})^{-1}.$$

In practice, the interferogram is inevitably truncated at finite optical path difference. Mathematically, this corresponds to a multiplication of the interferogram of infinite extension by a boxcar function. By Fourier transformation the true spectrum is thus convolved with a sinc function leading to leakage of the spectral intensity and to side lobes as spectral artifacts. Weighting functions known as apodization functions are applied to the interferogram in order to suppress these side lobes. Poorly collimated beams in the interferometer deteriorate the achievable spectral resolution.[62,63] Therefore, a circular aperture called the Jacquinot stop is used to limit the beam divergence of the globar radiation entering the interferometer. This aperture is made redundant using well collimated infrared synchrotron radiation. Adding zeros to the end of an interferogram before performing the discrete Fourier transform, so-called zero filling, has the effect of interpolating data points in the spectrum and to increase photometric accuracy. An actual measured interferogram is not perfectly symmetrical and contains sine components in addition to the cosine wave interferogram due to optical, electronic or sampling effects. This yields a complex spectrum rather than a real spectrum. Phase correction is applied in order to remove these sine components from an interferogram and to obtain the real spectrum.[63,88,89]

The radiation detector is the final essential component of every spectrometer. Mid-infrared detectors can be divided into two types: thermal detectors and quantum detectors.[62,63] Thermal detectors operate by sensing the change of temperature of an absorbing material. Pyroelectric detectors are capable of detecting radiation modulated in the audio-frequency regime. The heat-sensing element is a ferroelectric material. Usually deuterated triglycine sulfate (DTGS) is used. Below the Curie temperature it exhibits a spontaneous electrical polarization. The degree of polarization changes if the temperature of the material is changed. This change can be observed as an electrical signal, either as a voltage or a current. Quantum detectors depend on the interaction of infrared radiation with the electrons in a semiconductor. The most common quantum detectors in the mid-infrared are based on mercury-cadmium-telluride (MCT) alloys. Detection occurs when electrons from the valence band are excited to the conduction band through absorption of infrared photons of sufficient energy. The detector’s long wavelength cut-off is determined by the band gap. There are both photoconducting and photovoltaic MCT detectors. According to the Fermi-Dirac distribution MCT detectors are maintained at liquid nitrogen temperatures (77 K) to reduce noise from the thermal background and to achieve good sensitivity. Compared to pyroelectric DTGS detectors, MCT detectors are about two orders of magnitude more sensitive and also much faster, being responsive to modulation frequencies up to about 1 MHz.[63]

## 2.5 Infrared Microspectroscopy

Infrared microspectroscopy combines infrared spectral analysis with the spatial resolution of a microscope.[36,37] The coupling of infrared microscopes to Fourier-transform infrared spectrometers in the early 1980s made the technique practical, and it has since gained wide acceptance. An infrared microscope (see Figure 2.5 for a schematic diagram) for transmission measurements uses a condenser to focus the light from the source onto the sample. The objective collects the light that is transmitted by the sample. This way a magnified image of the illuminated sample is formed at the primary image plane, and this image is then reimaged onto a suitable detector.[37] Compared to a conventional optical microscope, an infrared microscope has the following specific features: infrared radiation from the interferometer serves as the source; only reflecting optics is used; an aperture at the primary image plane (i.e. a field stop) is used for sample definition; and an infrared sensitive detector is needed. Infrared microscopes incorporate a white-light microscope in the optical path which is parfocal and collinear. This allows one to view and to manipulate the sample at high magnification. This way also the spatially resolved infrared spectral information can be correlated with a visible image. In some high performance infrared microscopes an additional aperture is placed before the sample to limit the sample area illuminated by the infrared source. This is the so-called redundant or dual aperturing.[36] Such infrared microscopes using apertures for both the illumination and detection systems are referred to as having a confocal optical arrangement.[69] For condensing and collecting the radiation on-axis Schwarzschild or Cassegrain objectives are used. It should be noted that Schwarzschild objectives have a central obscuration of about 25%. Certain infrared microscopes employ infinity corrected objectives allowing one to put accessories such as polarizers or filters in the beam without affecting the position of the image plane in the microscope. Because of the photometric as well as the visual use, high numerical apertures, $NA$, are desirable even for moderate magnification objectives in order to increase the energy throughput and also the spatial resolution.[36] $NA$ characterizes the range of angles over which the objective can accept light and is defined by:

$$NA = n\sin\theta,$$

where $n$ is the index of refraction in which the objective is working, and $\theta$ is the maximum angle of light that can enter or exit the objective with respect to the central optical axis, i.e. half the maximum opening angle. Numerical apertures of about 0.6 to 0.65 are typically employed to provide a moderate working distance and to thus allow one to use accessories such as liquid cells.

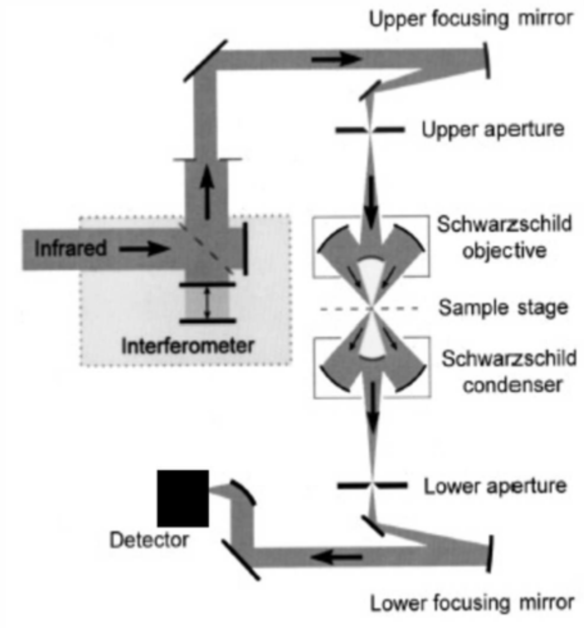

**Figure 2.5.** Schematic diagram of an infrared microspectrometer, adapted from Ref. 69.

The detector area becomes an important parameter in infrared microspectroscopy because reducing the detector area improves S/N.[37] A small area high-sensitivity liquid-nitrogen-cooled MCT detector is the standard detector employed in infrared microscopes. A typical detector size for infrared microscopes is 250 × 250 μm$^2$. Most infrared microscopes are routinely equipped with automated mapping stages. Reflection measurements can be performed by using a mirror as an aperture-dividing beamsplitter and employing only one objective, where half of the objective is used to condense the radiation onto the sample and the other half is used to collect the reflected radiation. More recently, microscopes have been developed for high speed Fourier-transform infrared spectroscopic imaging which work without apertures and employ array detectors instead of single element detectors.[90,91]

The theoretical spatial resolution, $r$, for a conventional microscope is dictated by the diffraction limit and may be expressed with respect to the wavelength of the light, $\lambda$, and the numerical aperture, $NA$, as:

$$r = \frac{0.61\lambda}{NA}\,.$$

For infrared microscopes the effects of the particular aperturing mode and also of the central obscuration of the Schwarzschild objectives must be considered. It was found that dual aperture single point detector systems provide the best spatial resolution.[92,93] Importantly, the theoretical spatial resolution cannot be obtained using the thermal globar source. Indeed, the performance is limited by the low source brilliance and the practical limit is about 20 to 25 μm.[68,69,94] By contrast, diffraction-limited spatial resolution can be achieved using brilliant infrared synchrotron radiation.[38,69,94]

## 2.6 Polarized Infrared Spectroscopy and Polarization Modulation

### 2.6.1 Conventional Infrared Linear Dichroism Measurements

The absorption of infrared radiation by an oriented sample is sensitive to the state of polarization of the incident radiation.[26,29,62,63,87,95] Therefore, polarized infrared spectroscopy provides a means to study molecular orientations because optical anisotropies are directly related to anisotropy in the sample. Absorption of linearly polarized light will be at a maximum when the electric field vector of the incident radiation, **E**, is parallel to the dipole-transition moment vector, **M**, of a particular vibrational mode, where **M** gives the variation of the dipole moment with the change of the normal coordinates. There will be no absorption if **E** is perpendicular to **M**. More generally, absorption will occur if **M** has a non-zero component parallel to **E**, and the angular dependence follows Malus' law. It is found that the intensity of the absorbed light, $I_a$, is proportional to the square of the scalar product of **E** and **M**:[96]

$$I_a \propto (\mathbf{E}\cdot\mathbf{M})^2 = (\mathrm{EM})^2 \cos^2\theta,$$

where $\theta$ is the angle between the electric field vector and the dipole-transition moment.

The differential or anisotropic absorption between orthogonal states of linearly polarized infrared light is termed infrared linear dichroism (IRLD) or more generally vibrational linear dichroism (VLD). Parameters commonly used to characterize vibrational linear dichroism or the degree of optical anisotropy are the dichroic difference,

$$\Delta A = A_{\|} - A_{\perp},$$

and the dichroic ratio,

$$R = A_{\|}/A_{\perp},$$

where $A_{\|}$ and $A_{\perp}$ are the absorbances of the sample for light polarized in planes parallel and perpendicular with respect to a reference direction. The parameter $R$ is related to the second Legendre polynomial, $P_2$, of the orientation distribution function, which describes the orientation of structural units of a sample with uniaxial symmetry, as follows:[26,29,95]

$$P_2\langle\cos\theta\rangle = \frac{R-1}{R+2} = \frac{1}{2}\left(3\langle\cos^2\theta\rangle - 1\right),$$

where $\theta$ is the angle between the segmental axis and the reference direction. $P_2$ is also referred to as the order parameter or Herman's orientation function. It is equal to one if all dipole-transition moments are perfectly oriented parallel to the reference direction, -0.5 for a perfect orientation at $\theta = 90°$, and it becomes zero for an isotropic sample or for a perfect orientation at $\theta = 54.7°$. Importantly, IRLD measurements can characterize sample orientation on the (sub)molecular level. They can be used to selectively determine the orientation of specific functional groups, a given phase or a certain component in a multiphase and multicomponent system.[28,29]

In the case of a conventional static polarization measurement the direction of the electric field vector is selected by a linear polarizer. The recording of the polarized spectra at normal incidence is the most straightforward way to measure the IRLD for samples having uniaxial symmetry.[29] In a static measurement the dichroic difference or the dichroic ratio are obtained from sequentially recording two independent absorbance spectra, $A_{\parallel}$ and $A_{\perp}$, corresponding to parallel and perpendicular polarization directions with respect to a reference direction. This static approach however suffers from instrumental and sample fluctuations during the experiment and therefore lacks the sensitivity to determine small dichroic signals. It is also relatively time-consuming due to the sequential measurements, and it requires the availability of a suitable reference for the collection of the background single beam spectrum. In practice, the two absorbance spectra $A_{\parallel}$ and $A_{\perp}$ can be obtained by a 90° rotation of either the polarizer or the sample.[29] In the case of the rotation of the polarizer the same part of the sample is illuminated for both polarization states. However, a total of four single beam spectra must be recorded because two reference spectra are required due to the fact that the beamsplitter of the Fourier-transform infrared spectrometer is polarization sensitive. In the case of the rotation of the sample only three single beam spectra are required as only one reference spectrum is needed. But it may be difficult to make sure that exactly the same area is illuminated as the sample is rotated. Dichroic infrared measurements on small or heterogeneous anisotropic samples can be performed using polarized infrared microspectroscopy.[97] In this case accurate repositioning after sample rotation is even more complicated. One concern with regard to infrared microscopes may be the question if the instrument itself perturbs the polarization independent of the sample. It is found however that the polarization purity is sufficient and that polarization scrambling is negligible in current infrared microscopes.[97] It should also be noted that microspectroscopic measurements are performed at near-normal incidence due to the opening angles introduced by the objectives.

### 2.6.2 Polarization Modulation Fourier-Transform Infrared Spectroscopy

Polarization modulation (PM) infrared spectroscopy is a special polarized infrared spectroscopic technique which allows one to measure spectral dichroism with high sensitivity. It has been profitably applied to infrared reflection-absorption spectroscopy (IRRAS),[98-105] and to studies of vibrational circular dichroism (VCD)[56,106-108] and vibrational linear dichroism.[28,29,56-58,87,109-116] The sensitivity of this method comes from the fact that the dichroic difference ($\Delta A$) spectrum is measured directly by modulating the polarization of the incident infrared beam at high frequency with a photoelastic modulator (PEM).[29] PM makes use of the so-called ac advantage which says that a small difference signal can be measured more accurately as the amplitude of a periodically varying ac signal than as the difference between two time-independent dc signals.[56,63]

The key component in a PM setup is the photoelastic modulator.[117] The PEM is the device used for varying or modulating the polarization of a beam of light at a fixed resonant frequency in the low frequency ultrasound range (e.g. 50 kHz). The operation of the PEM is based on the phenomenon of photoelasticity. By means of piezoelectric transducers the intrinsically optically isotropic PEM crystal is periodically stressed by compression and stretching which generates an oscillating birefringence. Linearly polarized radiation from a polarizer enters the PEM such that the electric field vector has an angle of 45° with respect to the PEM optical axis. The electric field vector splits into two orthogonally polarized components of equal amplitude. The birefringence introduces a phase shift between these two components. The phase difference created by the PEM is also called retardation and it oscillates as a function of time. When the peak retardation is one half of the wavelength of the light, i.e. $\lambda/2$, the PEM modulates the light beam between two perpendicular, linearly polarized states at its 2nd harmonic. The PEM then acts as an oscillating half-wave plate or polarization rotator (see Figure 2.6).[62,87] In contrast to a conventional static half-wave plate however, the PEM produces a high-frequency linear polarization modulation thus permitting sensitive measurements of the IRLD.

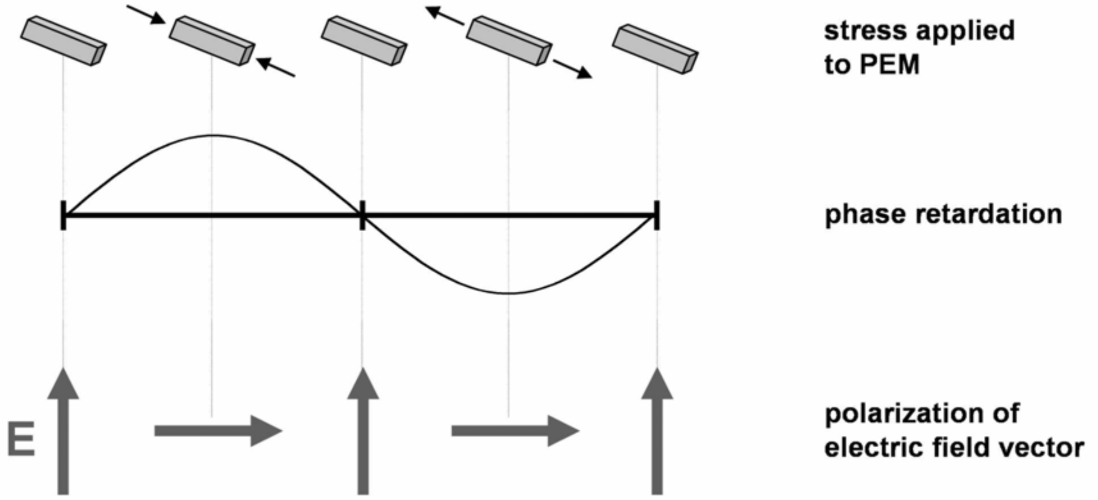

**Figure 2.6.** Periodically applied stress to the photoelastic modulator (PEM) generates an oscillating birefringence. When the peak retardation is equal to $\lambda/2$, the PEM modulates incident linearly polarized light between two perpendicular, linearly polarized states at its 2nd harmonic. The PEM then acts as an oscillating polarization rotator.

In the continuous scan mode the interferometer modulates the infrared radiation at the Fourier frequencies. Therefore, at the output of the interferometer the infrared beam has an intensity modulation which depends on the wavenumber of the radiation and the velocity of the moving mirror in the interferometer. The beam is then polarized with a linear polarizer and passes through the PEM. The PEM introduces the linear polarization modulation at its second harmonic. The polarization modulation therefore imposes a high-frequency signal on the normal interferogram Fourier frequencies. This means that a double-modulated infrared beam reaches the detector. The detected signal contains two components, $I_{\mathrm{sum}}$ and $I_{\mathrm{diff}}$. $I_{\mathrm{sum}}$ carries only the intensity modulation induced by the interferometer and gives the static sum reference or background spectrum. $I_{\mathrm{diff}}$ contains the polarization modulation induced by the PEM and produces the differential spectrum between the polarization directions. The double-modulated raw detector signal is demodulated giving the two signals, $I_{\mathrm{sum}}$ and $I_{\mathrm{diff}}$, by using electronic filtering and either a lock-in amplifier or a dedicated synchronous sampling demodulator[100,101] with the demodulation frequency tuned to the second harmonic of the PEM. For a lock-in amplifier the electronic detection bandwidth is up-limited to the second harmonic of the PEM, whereas for the synchronous sampling demodulator contributions from higher harmonics of the second harmonic of the modulator frequency are also registered.[100,101] In the case of the synchronous sampling demodulator there is less need to separate well the low-frequency signal due to the interferometer (Fourier frequencies) and the high-frequency contribution from the PM thus allowing one to measure at faster scanning speeds and hence in a shorter time. The difference and the sum outputs are amplified and then digitized, and the two interferograms are Fourier-transformed to give the difference and the sum single beam spectra. Importantly, the advantages of polarization modulation over the static approach can only be fully realized by using simultaneous dual-channel data collection.[87] In this case, both the differential absorption and the static sum background are acquired simultaneously at the same sample position in a single experiment. The difference spectrum is normalized over the static sum reference spectrum yielding the normalized experimental linear dichroic spectrum. For this spectrum instrumental fluctuations and atmospheric changes over time become negligible in comparison to conventional polarized measurements without polarization modulation.

The normalized experimental linear dichroic spectrum can be further processed to obtain the dichroic difference, $\Delta A$.[58] It should be noted that the PEM induces not only a time-dependent but also a wavenumber-dependent phase retardation. Therefore, polarization modulation introduces an artifact in the spectral shape due to the wavenumber-dependent modulator efficiency, i.e. the wavenumber-dependent phase retardation amplitude. This effect depends on the modulator's particular driving voltage set to achieve $\lambda/2$ retardation for a chosen wavenumber. The experimental linear dichroic spectrum contains Bessel function factors that account for the wavenumber-dependent effectiveness of the modulator to produce linearly polarized radiation.[56] There will be discrepancies between experimental and theoretical values of the Bessel functions due to experimental artifacts such as residual birefringence of the photoelastic modulator and polarization artifacts of the optical setup and the detector.[99,102,110] This means an experimental calibration procedure is needed in order to account for the PEM efficiency. Such an experimental calibration and normalization procedure for polarization modulation IRLD measurements in transmission has been established.[58] The calibration measurements are performed by replacing the sample by a second linear polarizer which is oriented either parallel or perpendicular to the polarizer positioned in front of the PEM.[29] The polarizer represents a sample that completely transmits one polarization and that totally absorbs the other one. The dichroic difference, $\Delta A$, can then be calculated from both the sample and calibration data.[58]

Polarization modulation IRLD experiments are almost exclusively performed on macroscopic samples in optical benches on infrared spectrometers. However, in one case this technique was coupled with an infrared microscope to obtain spatial resolution.[118] The reported resolution limit was reached when using a square aperture of 30 x 30 $\mu m^2$, and a square aperture of 20 x 20 $\mu m^2$ gave insufficient S/N. In an application to study isotactic polypropylene films the sampling area used was 200 x 200 $\mu m^2$.[119]

## 2.7 Infrared Microfluidic Cuvettes

There are standard infrared transmission flow cells which are commercially available.[120] In addition, custom-built fluidic cuvettes for specialized applications have been reported.[121] Miniaturization through microfabrication can produce infrared microflow cells. Dedicated microfluidic cells have been implemented as micromixing devices for infrared reaction monitoring[122-127] and for hyphenation with capillary electrophoresis.[128,129] Maximum versatility of fluidic cuvettes for optical methods is achieved with substrate materials having a broad wavelength transmission range. Calcium fluoride ($CaF_2$) is an ideal substrate candidate because it has a broad transmission range from the ultraviolet (~ 130 nm) to the infrared (~ 11 µm) where it also covers the infrared fingerprint region. $CaF_2$ is a transparent colourless crystal with a fluorite-type crystalline structure. It is suited for microfabrication because it can be micromachined,[130,131] chemically etched,[129] and structured and bonded by photoresists.[123,126,129] Moreover, it can be surface-activated by electron[132] or laser irradiation.[133]

For a full understanding of biological macromolecules and complex biological systems it is necessary to measure them in their native environment. This *in situ* approach can lead to insights into the relationship between structure and function and allows one to observe dynamic structural changes. Water is the natural solvent for biological systems. It should be noted that water has strong absorption bands in important regions of the mid-infrared spectral range.[121,134,135] The bending mode of liquid $H_2O$ is around 1640 $cm^{-1}$ and it is superimposed on the so-called amide I absorption band of proteins. Therefore, the path length of an infrared cuvette should be below 10 μm in order to achieve an acceptable S/N for proteinaceous biological samples in this important spectral region.[121,135] The influence of water absorption has to be compensated for to extract the chemical and structural information of the biological molecules. However, accurate water subtraction is difficult.[135] Firstly, the required path length stability or reproducibility is in the nanometer range. This mechanical stability is very difficult to maintain due to changes in temperature, pressure fluctuations in flow systems, and possible repetitive mounting and demounting of the cuvette. Secondly, an accurate compensation between sample and reference is complicated because the sample occupies some solvent volume which means the water concentration and absorption is changed. Also, possible wedge errors in the cuvette geometry can introduce inherent differences between the sample and the reference path lengths.

A dedicated miniaturized sampling device has to be implemented in order to be able to study single living biological cells *in situ* by infrared microspectroscopy in aqueous medium. In addition to the required low path length of below 10 μm, the physiological conditions have to be maintained by controlling *p*H and temperature. Also, the used components should not be cytotoxic and the cuvette substrate should not be water soluble. A microfluidic environment seems desirable to be able to supply fresh *p*H-buffered medium and to remove waste. The flow system may also be used to vary the environmental conditions by e.g. introducing drugs or changing *p*H and by inducing a shear stress. The microdevice should ideally allow one to culture the biological cells, observe them with visible light and measure them with infrared radiation. The possibility of visual inspection during measurement is important to be able to correlate the spectral infrared information with visible images of the cells. A temperature-controlled miniincubator for infrared microspectroscopy was reported in the literature.[55] However, there was little information given on the system. It seems there was no microflow provided and that the sampling geometry was a “double pass transmission”, i.e. the infrared beam passes through the sample and is then reflected back from the surface of the substrate and passes the sample again, rather than a simple transmission.[52] This reflection-absorption or so-called transflection geometry may introduce artifacts that must be corrected by computational processing of the acquired spectra.[136]

# 3 Experimental Setup

## 3.1 Infrared Spectroscopic Beamline at BESSY II

BESSY II is a third generation synchrotron radiation facility. The electron storage ring is operated at an electron energy of 1.7 GeV. It provides highly brilliant radiation from the terahertz region to hard X-rays, especially in the vacuum ultraviolet and soft X-ray region. The IRIS beamline at BESSY is a high-performance, infrared-dedicated beamline which combines a very stable frontend for the extraction of infrared synchrotron radiation with a versatile multistation experimental area. It was commissioned as a multipurpose infrared beamline for materials science and biological investigations in 2001.[137,138] It is equipped with two Fourier-transform infrared spectrometers, one infrared microscope, an infrared spectral ellipsometer and a terahertz port. The IRIS beamline is a large acceptance infrared beamline which delivers bending magnet radiation from a homogeneous dipole field and it is comprised of a modified dipole chamber, the frontend and the beamline (see Figure 3.1 for a layout of the beamline). It provides useful infrared intensities over the energy range from over 10,000 cm$^{-1}$ down to 50 cm$^{-1}$ and lower.[138] In the dedicated “low alpha mode”, where the normal electron bunch length is shortened, BESSY becomes a coherent synchrotron radiation source of high intensity far-infrared radiation by a controlled steady-state process.[139]

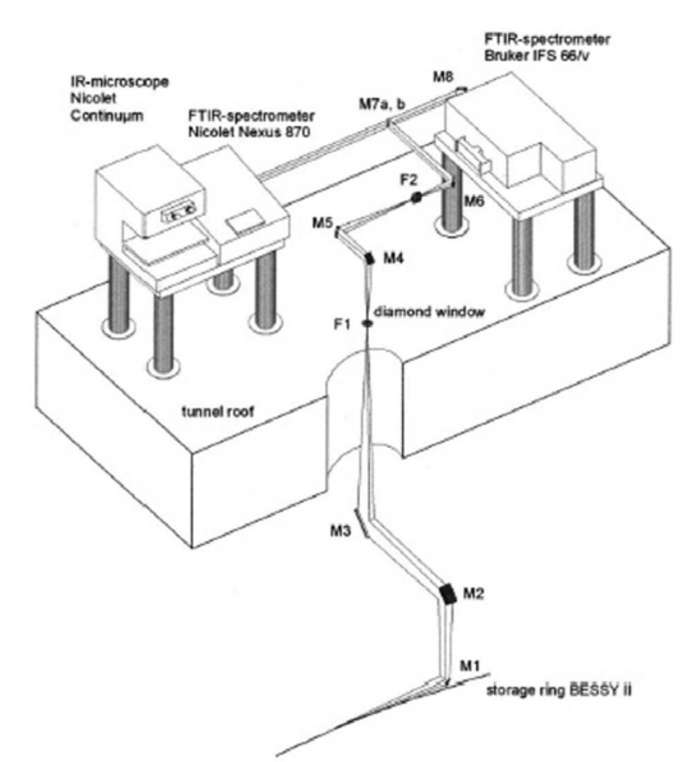

**Figure 3.1.** Layout of the infrared-dedicated IRIS beamline at BESSY II.

Infrared synchrotron radiation is emitted with a large opening angle compared to vacuum ultraviolet and X-ray synchrotron radiation. This makes specially designed frontends and beamlines necessary.[137] Specifically, large vertical and horizontal acceptance angles, a first optical element very near the source, and protection of the first element from the high heat load are essential requirements. The first optical element is a plane extraction mirror which diverts the radiation upwards by 90°. It provides horizontal and vertical collecting angles of about 60 x 30 $\mathrm{mrad}^2$. This mirror is split into two halves which are positioned above and below the narrow high-energy radiation fan in the ring plane. Therefore, the high-energy portion of the beam can pass through to a water cooled absorber at the rear of the dipole chamber. The second and third mirrors are both cylindrical and focus the radiation vertically and horizontally to an intermediate focus which is outside the radiation shielding wall and just behind a wedge window of polycrystalline chemical vapour deposition diamond. The concrete radiation shielding is required for the operation of the experimental stations on top of the storage ring tunnel. By mounting the experiments on the massive storage ring tunnel roof the mechanical stability required for vibration-sensitive infrared measurements can be achieved. The diamond window has a broadband infrared transmission, but it should be noted that diamond has intrinsic multi-phonon absorption bands which appear in the mid-infrared spectrum.[140] This window separates the ultrahigh vacuum system of the frontend from the remainder of the beamline which has a secondary high- or fore-vacuum environment. The fourth and fifth mirrors are also both cylindrical and transfer the radiation and refocus it at the second focus. All these mirrors have an unprotected aluminium coating. The sixth mirror is a toroidal mirror which is used to collimate the beam. There are finally two interchangeable plane mirrors, one of which is used to direct the collimated beam through a KBr window to the optical bench of the infrared microscope. The infrared microscope is a Nicolet Continuμm and it is coupled to a Nicolet Nexus 870 Fourier-transform infrared spectrometer. The spectrometer and microscope are operated in purged air in order to suppress absorptions from gaseous water and carbon dioxide from the atmosphere. The Nicolet Continuμm microscope has inifinity corrected Schwarzschild objectives and uses dual aperturing. Figure 3.2 shows the obtained intensities through the microscope's aperture for both the infrared synchrotron source and the thermal globar source. This source comparison clearly demonstrates that the intensities through square apertures below 20 x 20 $\mu\mathrm{m}^2$ are significantly higher for the brilliant synchrotron radiation. The instrumentation allows one to perform diffraction-limited infrared microspectroscopy using synchrotron radiation.

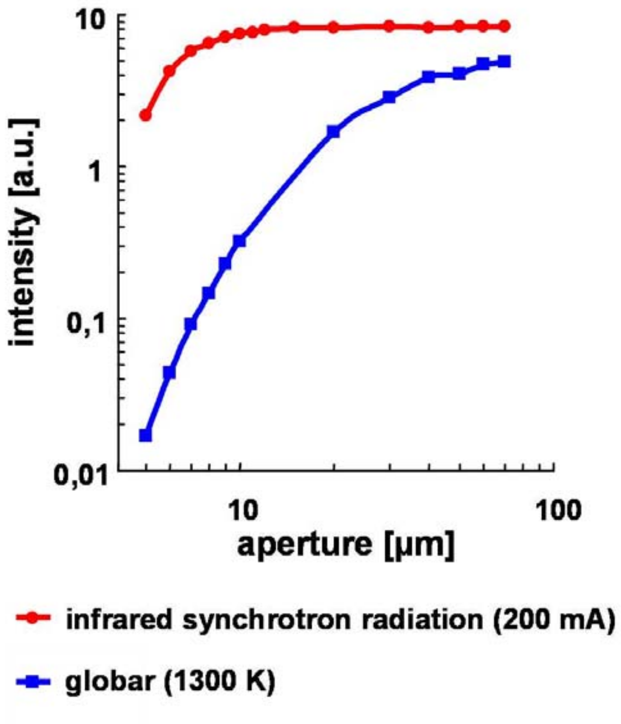

**Figure 3.2.** Source comparison performed at the infrared microscope on the IRIS beamline. Through small apertures (< 20 µm) the brilliant synchrotron source offers a significant intensity advantage over a thermal globar source.

## 3.2 Polarization Modulation Setup for Polarized IR Microspectroscopy

In the course of this dissertation a polarization modulation apparatus on the infrared microscope of the IRIS beamline at the electron storage ring BESSY II was implemented for sensitive measurements of vibrational linear dichroism.[141-143] The goal was to combine polarization modulation with Fourier-transform infrared synchrotron microspectroscopy as a novel microprobe and to benefit from the brilliant synchrotron source in terms of spatial and temporal resolution. The setup is comprised of a beam compressor in the Fourier-transform infrared spectrometer and a linear polarizer and a photoelastic modulator between the spectrometer and the microscope (see Figure 3.3 for a scheme of the experimental setup). In addition to these optical components, it includes also electronics which provide modulation control and demodulation.

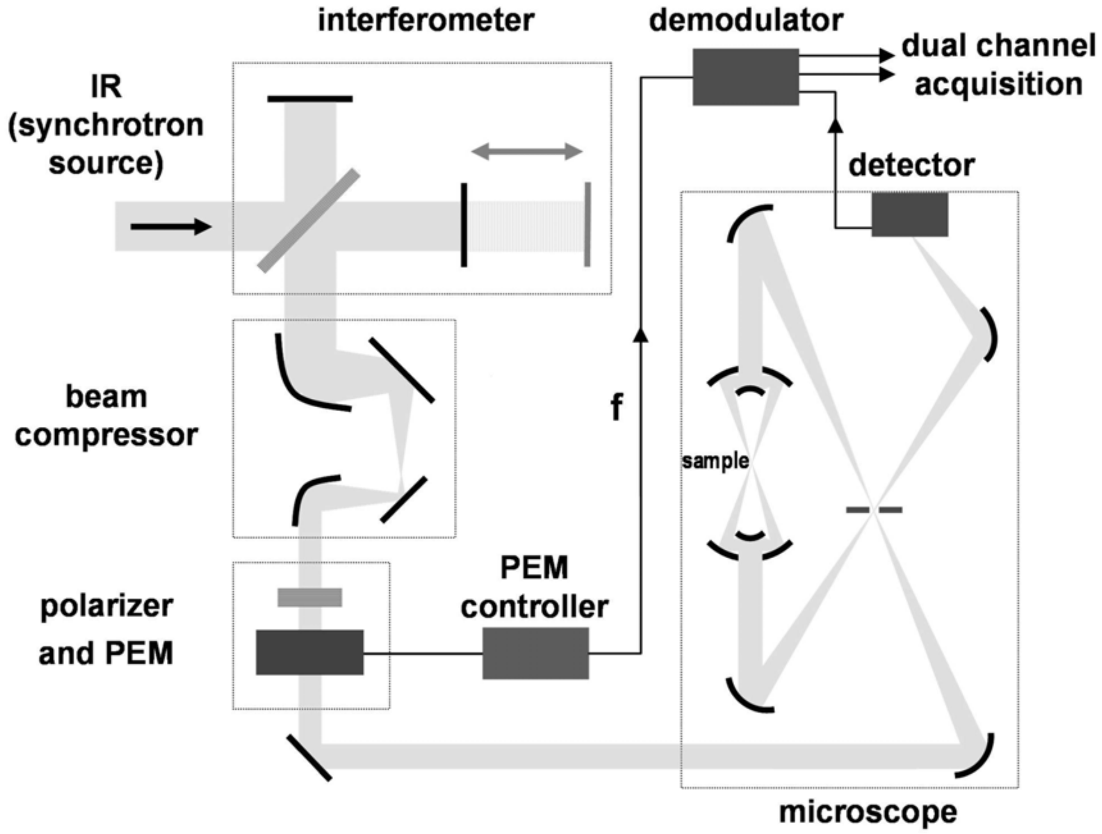

**Figure 3.3.** Scheme of the polarization modulation setup on the infrared microscope of the IRIS beamline.

The key component in the polarization modulation setup is the photoelastic modulator (Hinds Instruments, PEM-90 II, ZnSe, 50 kHz) which has a limiting useful aperture of 14 mm. Consequently, the optical design had to be adapted so that the collimated infrared beam passing from the interferometer into the microscope could be fully accommodated in the new setup. This was achieved by the insertion of a compact custom-built, adjustable beam compressor which was fitted into the restricted available space in the Fourier-transform infrared spectrometer (Nicolet Nexus 870). The beam compressor consists of two 90°-off-axis parabolic mirrors and two plane mirrors. It compressed the diameter of the collimated IR beam from 40 mm to 13 mm by choosing the appropriate ratio of focal lengths for the two parabolic mirrors. The performance of the beam compressor benefits from the superior collimation quality of the infrared synchrotron beam compared to light from the conventional globar source.

The polarization modulation unit is situated between the spectrometer and the infrared microscope (Nicolet Continuμm). It consists of a linear polarizer (Specac, holographic aluminium grid, KRS-5) and a photoelastic modulator which are both mounted on an adjustable bench and housed in a purged polycarbonate box. The polarizer generates linearly polarized infrared light with a desired orientation of the electric field vector. It should be noted that the inherent polarization of the infrared synchrotron radiation needs to be taken into account and may be advantageously exploited. The photoelastic modulator serves as the polarization modulation device and is placed in the beam path directly after the polarizer with the optical axis of the PEM crystal being tilted at 45° with respect to the plane of polarization of the incident infrared radiation. The operation of the PEM is based on the phenomenon of photoelasticity (cf. Chapter 2.6.2). By means of piezoelectric transducers the ZnSe crystal is stressed by compression and stretching generating an oscillating birefringence at a frequency of 50 kHz. When operated with a peak retardation of $\lambda/2$ and incident linearly polarized light the PEM modulates the light beam between two perpendicular, linearly polarized states at its second harmonic, i.e. 100 kHz. The PEM optical head is linked, via the electronic head, to its controller which governs the peak retardation and which also sends the required phase reference frequency to the demodulator unit. In the whole setup the infrared beam experiences a double modulation due to the interferometer and the polarization modulation device. The microscope detector electronics were modified so that the infrared signal from the MCT detector can be extracted after the preamplifier and fed into a demodulator unit. The synchronous sampling demodulator (GWC Technologies, SSD 100) demodulates the differential polarization signal for the two perpendicular, linearly polarized states from the modulated interferogram and generates the differential and sum interferograms.[100,101] To set up the sample for measurement either the demodulated output difference signal or sum signal can be returned to the microscope detector electronics and digitized by the analog-to-digital converter. Thus, using the microscope software, real-time difference and sum interferograms or spectra can be observed during positioning and adjustment of the sample in the confocal IR microscope. Importantly, in the measurements both the difference signal and the sum signal are acquired simultaneously exploiting the dual channel capabilities of the spectrometer's hardware and software. The difference and the sum outputs from the demodulator are amplified and then digitized. The largest data point in either interferogram is used to correlate both interferograms. Therefore, by choosing appropriate gain settings, the centerburst of the sum interferogram defines and thereby helps to correctly identify the zero path difference point in the difference interferogram. This is important because the difference interferogram does not necessarily have a centerburst, and a possible misidentification of the zero path difference point would lead to phase-correction-induced spectral anomalies.[144] The respective infrared vibrational spectra are calculated from the obtained interferograms via a fast Fourier transform. The sum interferogram is used for the calculation of all phase corrections so that the phase array calculated from this interferogram is employed for the phase correction of both the sum spectrum and the difference spectrum. Each measurement thus gives two spectra, the difference spectrum ($I_{\text{diff}} = I_{\|} - I_{\perp}$) and the sum spectrum ($I_{\text{sum}} = I_{\|} + I_{\perp}$), where $I_{\|}$ and $I_{\perp}$ denote the detected spectral intensities for light polarized in planes parallel and perpendicular with respect to a reference direction. The difference spectrum and the sum background spectrum are acquired simultaneously at the same sample position. There is thus a reference-free inherent background collection in real-time. The ratio $I_{\text{diff}}/I_{\text{sum}}$ yields the normalized experimental linear dichroic spectrum.

## 3.3 Infrared Microfluidic Cuvette

A dedicated microfluidic infrared transmission cuvette for measurements of biological macromolecules and complex biological systems in their native aqueous environment was implemented in cooperation with the Institut für Mikrostrukturtechnik of the Forschungszentrum Karlsruhe. Specifically, this cuvette with its peripheral elements was designed to study single living biological cells *in situ* by infrared microspectroscopy with concomitant visible observation. In addition to biocompatibility, two major constraints were given by the required path length of below 10 μm and the working distance of ± 7 mm of the Nicolet Continuμm microscope at BESSY. A demountable design to achieve ease of cell culturing as well as cleaning, and *p*H and temperature control for maintaining physiological conditions were further requirements. $CaF_2$ was chosen as the window material because of its suitable transmission characteristics and because it is scarcely soluble in water and amenable to microfabrication (cf. Chapter 2.7).

The design and the implementation of the microfluidic cuvette are pictured in Figure 3.4. The cuvette is based on two $CaF_2$ windows (Crystech Inc., polycrystalline, UV grade, ∅ = 1 inch, thickness = 2 mm). One of the $CaF_2$ windows carries polyimide (Durimide 7020, Arch Chemicals) structures produced by photolithography under cleanroom conditions. This negative photoresist was found to be suitable both in terms of processibility as well as applicability in the experiments. The photolithography involved spin coating of the polyimide onto the $CaF_2$ substrate, a two-stage soft-baking at 90° C and 110° C, exposure to ultraviolet light (200 $mJ/cm^2$) through a patterned photomask which was in contact with the photoresist, post-exposure baking at 110° C, development, and hard-baking at 400° C in vacuum. The polyimide structures serve as a spacer, define the sample volume and act as a sealant when compressing both windows. The design of the structures and their height could be tailored and optimized according to the experimental needs. Importantly, structural heights of 6 µm, 8 µm and 10 µm were realized thus meeting well the given path length requirement. Structural widths between 100 µm and 850 µm were found to be adequate.

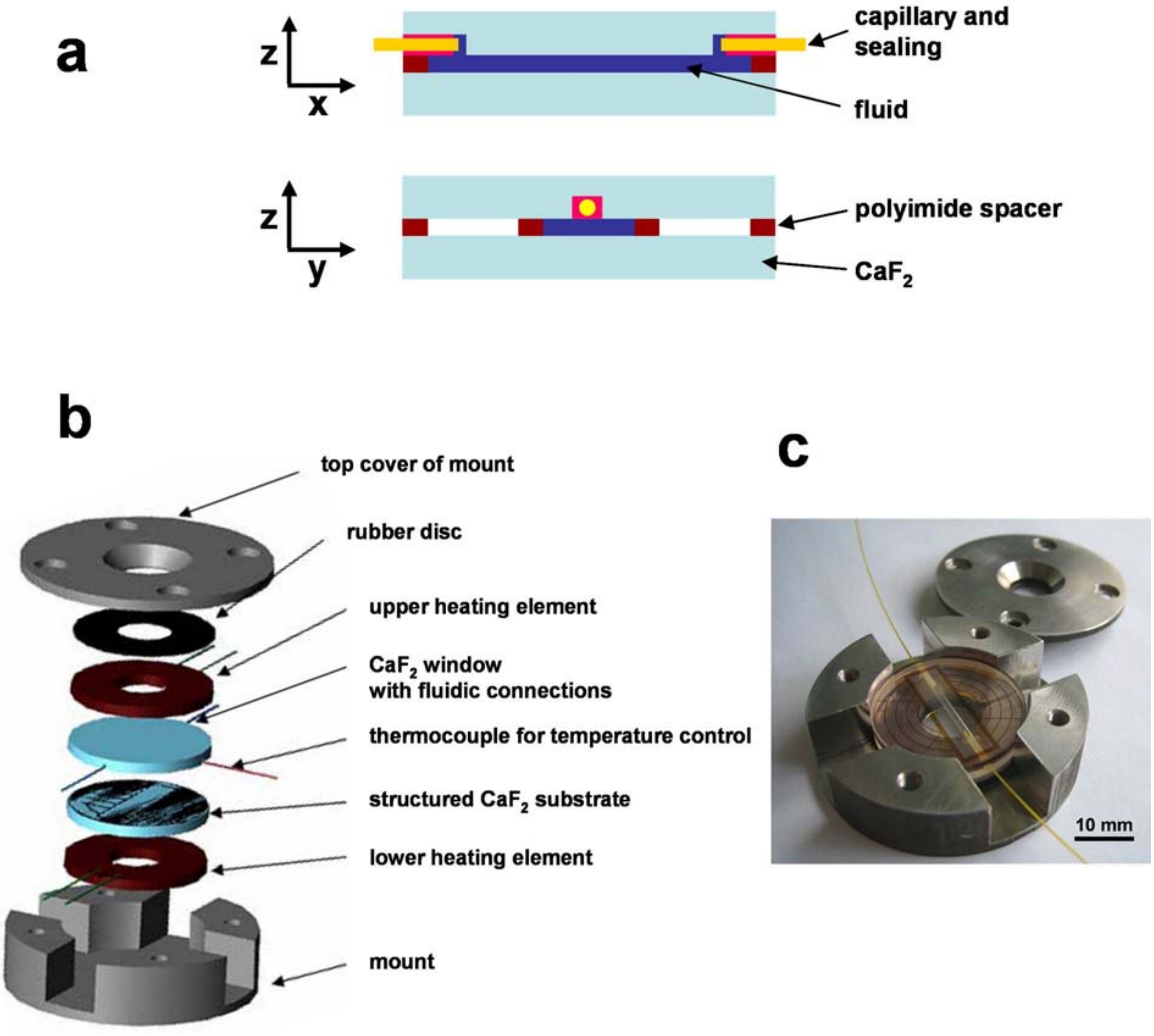

**Figure 3.4.** Sketch (a), design (b) (cf. Ref. 145), and implementation (c) of the microfluidic infrared (and ultraviolet-visible) transmission cuvette.

The second $CaF_2$ window contains lateral fluidic connections using either steel capillaries (outer ∅ = 600 µm, inner ∅ = 300 µm) or polyetheretherketone capillaries (outer ∅ = 360 µm, inner ∅ = 150 µm) to couple to the fluidic periphery. Lateral connections were chosen in order to narrow the vertical extension of the cuvette. Micromilling based on computer-aided design produced two grooves of 800 µm depth, 1 mm width and 7 mm length at the rim of the $CaF_2$ substrate. Plane adhesive sealing of the capillaries in these grooves was done with silicone (Elastosil M 4601, Wacker) or biocompatible cement (Dentsply). These connections provide the inflow and the outflow. When both $CaF_2$ windows are compressed, the confined cuvette volume defined by the polyimide structures becomes thus a flow-through chamber. The flow is produced by a high-precision, low-flow-rate syringe infusion pump (Harvard Apparatus, 11 Plus). Liquids and solutions, such as *p*H-buffered culture medium, are provided by a gas-tight syringe (2.5 mL, SGE) using high performance liquid chromatography tubing and fittings. The small volume in the cuvette (~ 1 μL) necessitates small flow rates (on the order of a few μL/h) in the presence of living cells in order to minimize shear stress. It was found that the chamber height of at most 10 μm indeed is an impediment for both the flow and the cell culturing. Fresh medium and drugs can be supplied and waste can be removed only slowly considering a dead volume of the fluidic periphery of approximately 20 μL. It seemed desirable to partly decouple flow and observation, and to thus have regions for observation with a small chamber height (small cross-sectional area) as well as regions of higher flow with a larger cross-sectional area. Also, an overall larger cuvette volume appears to be advantageous for cell culturing because a larger reservoir of medium would be provided. Therefore, in an alternative design, one end-to-end groove containing both connections instead of two grooves was implemented. This groove provides a vastly increased cross-sectional area compared to a chamber without an end-to-end groove while maintaining regions with a small chamber height. The chamber volume was thus increased to about 10 μL. Therefore, flow or exchange rates which are one order of magnitude larger become feasible. This design optimization proved crucial in improving culturing times and experimental capabilities. An additional groove was fabricated in the same window in order to place a thermocouple as close as possible to the cuvette chamber for accurate temperature sensing.

Temperature control is essential in order to maintain a cell culture environment of 37° C. Moreover, the experimental applicability of the cuvette is increased by being able to access and adjust a range of temperatures. Initially, a concept based on the circulation of a liquid as either a cooling agent or a heating agent was pursued because it gives a more general and versatile approach. Custom-built polymethylmethacrylate rings with fluidic grooves and connections were pressed onto both $CaF_2$ windows to heat or cool by the flow-through of a liquid. In principle, this approach was feasible and a temperature of 37° C in the cuvette chamber could be maintained. However, handling and minor leakage proved to be problematic. Therefore, an alternative concept based on resistively heated elements was implemented and the cooling capabilities were discarded.[145] The heating elements consist of thin metallic layers of gold and chromium on polyetheretherketone rings which are pressed onto the $CaF_2$ windows. This setup resulted in better handling and reliability. Temperature control is achieved by a thermocouple and a proportional-integral-derivative controller.

The $CaF_2$ windows together with the heating elements and a rubber ring are compressed by a steel mount. The vertical height of this modular setup is 12 mm and fits the space requirements of the Nicolet Continuμm microscope at BESSY well. Using different baseplates, this device can be placed also in other microscopes. Essentially, the microfluidic cuvette with its peripheral elements can be used as a miniincubator and *in situ* measurement chamber. Given the transmission characteristics of $CaF_2$ and the compact design, this device is also more generally applicable, e.g. to studies of molecules and materials in liquids and liquid flows in the infrared, visible and ultraviolet wavelength regions.

# 4 Results

## 4.1 Performance Evaluation of the Polarization Modulation Setup

### 4.1.1 Measurements on Thin Films of Polypropylene

The setting up of a polarization modulation apparatus on the infrared microscope of the IRIS beamline at BESSY II has entailed the implementation of a novel method for the structural characterization of anisotropic microscopic samples. Therefore, it was necessary to test the performance and to evaluate the capabilities of this technique during its development.[141] Initial tests were performed on thin sheets of isotactic polypropylene (iPP; Goodfellow, 8µm, and thin films provided by Dr. G. Ellis, CSIC, Madrid) measured in transmission. The infrared beam in a polarization modulation IRLD experiment experiences a double modulation (cf. Chapter 2.6.2). Figure 4.1a shows the detector signals obtained prior to demodulation when the photoelastic modulator in the setup was turned on or off respectively. When the PEM was turned off, a normal interferogram was found due to the Fourier modulation produced by the interferometer. An additional high-frequency contribution (100 kHz) from the polarization modulation was seen when the PEM was turned on. This double-modulated raw detector signal was demodulated giving the sum and difference interferograms (see Figure 4.1b). It can be seen that the difference interferogram does not have a distinct centerburst. Therefore, the data point corresponding to the well-defined centerburst of the sum interferogram is used for correlation to correctly identify the zero path difference point in the difference interferogram.

The respective infrared vibrational spectra are calculated from the obtained interferograms via a fast Fourier transform. Two spectra are recorded simultaneously in a measurement, the difference spectrum ($I_{\text{diff}} = I_{\parallel} - I_{\perp}$) and the sum spectrum ($I_{\text{sum}} = I_{\parallel} + I_{\perp}$), where $I_{\parallel}$ and $I_{\perp}$ denote the detected spectral intensities for light polarized in planes parallel and perpendicular with respect to a reference direction. The ratio $I_{\text{diff}}/I_{\text{sum}}$ yields the normalized experimental linear dichroic spectrum which is termed PM dichroic spectrum (or PM-LD spectrum) in the following.

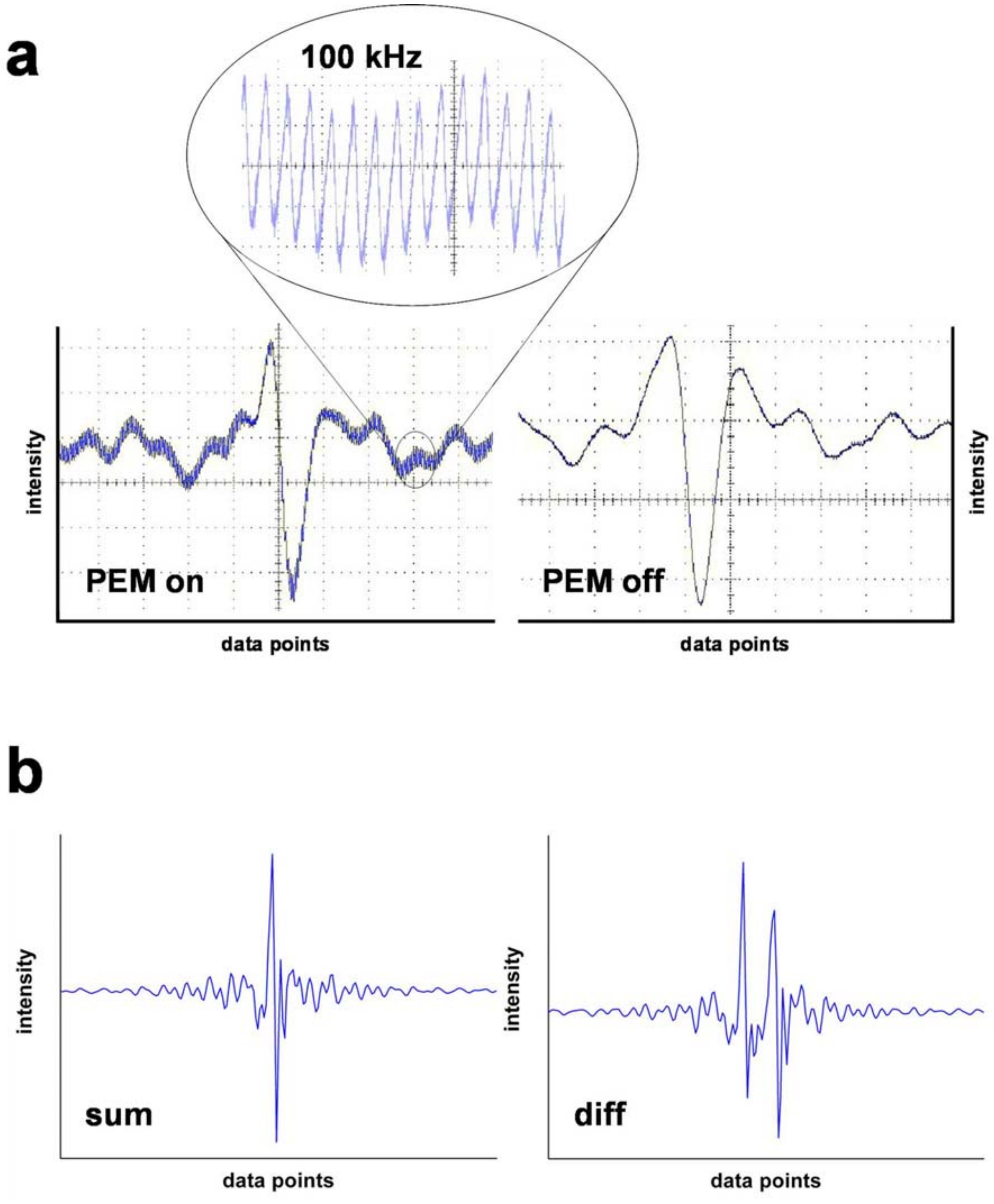

**Figure 4.1.** a) Interferograms obtained prior to demodulation when the photoelastic modulator was turned on or off respectively. A double modulation containing contributions from the interferometer and from the high-frequency polarization modulation (100 kHz) is seen when the PEM is turned on. b) Demodulation gives the sum and difference interferograms.

Figure 4.2 shows the PM dichroic spectra of a microscopic iPP sample and, for reference, of a thin film polarizer[146] which was oriented either parallel or perpendicular to the polarizer positioned in front of the PEM. The PEM peak retardation of $\lambda/2$ was set for 1150 cm$^{-1}$. For the two spectra of the polarizer it can be seen that the polarization modulation introduces an artifact in the spectral shape due to the wavenumber-dependent modulator efficiency, i.e. the wavenumber-dependent phase retardation amplitude. It is possible to further process the experimental linear dichroic spectrum in order to obtain the dichroic difference, $\Delta A$.[58] From the ratio $T_{\text{ratio}} = T_{\parallel} - T_{\perp} / T_{\parallel} + T_{\perp}$, where $T_{\parallel}$ and $T_{\perp}$ are the sample transmittances for light polarized in parallel and perpendicular planes, the dichroic difference $\Delta A$ can be calculated by the relation $\Delta A = \log(1 - T_{\text{ratio}} / 1 + T_{\text{ratio}})$. Due to instrumental artifacts such as wavelength-dependent PEM efficiency, but also residual birefringence of the photoelastic modulator and polarization artifacts of the optical setup and the detector, the raw PM dichroic spectrum is not a proper representation of $\mathrm{T}_{\text{ratio}}$. An experimental calibration procedure[58] is needed in order to account for these artifacts and to obtain $\Delta A$. The calibration measurements are performed by replacing the sample by a linear polarizer which is oriented parallel and perpendicular to the polarizer positioned in front of the PEM.

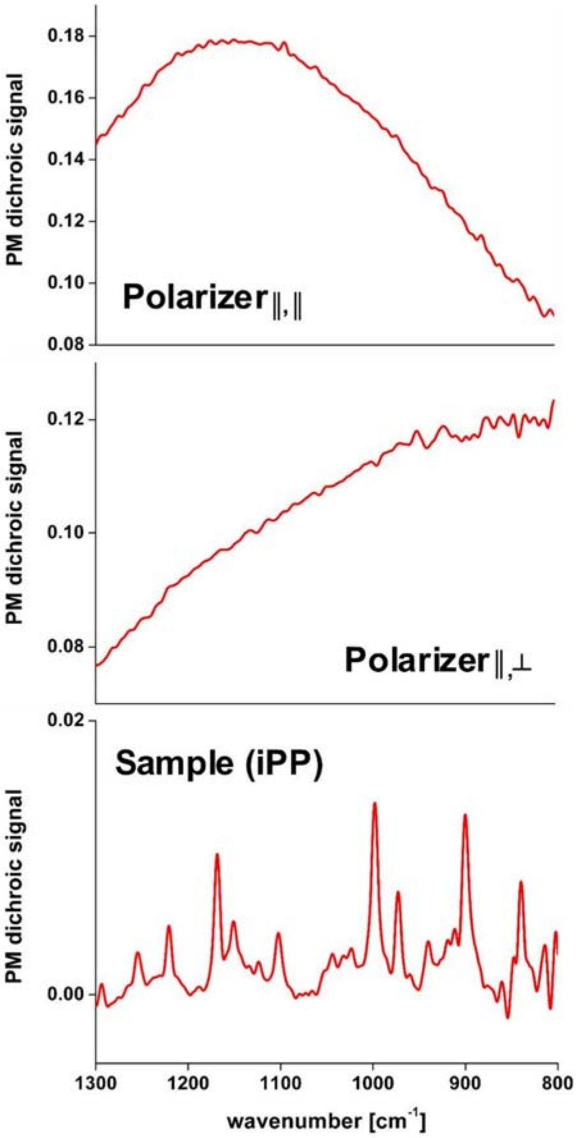

**Figure 4.2.** PM dichroic spectra of a thin film polarizer which was oriented parallel and perpendicular to the polarizer positioned in front of the PEM, and of a microscopic iPP sample.

Figure 4.3 shows the result of the calibration procedure for the PM dichroic spectrum of iPP given in Figure 4.2. The calibrated spectrum is in reasonably good agreement with a spectrum obtained by a conventional static polarization measurement. This means that PM dichroic spectra can be compared to conventional polarized spectra. Moreover, the S/N of the calibrated PM spectrum appears to compare favourably with respect to the static measurement. A more pronounced improvement is expected for even smaller values of $\Delta A$.[56,57,63]

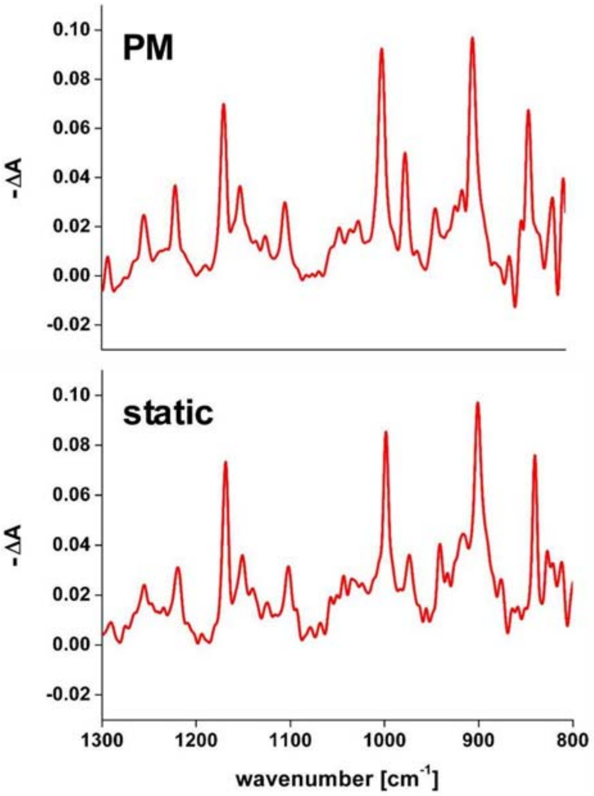

**Figure 4.3.** Comparison of a calibrated PM dichroic spectrum of iPP with an iPP spectrum obtained by a conventional static polarization measurement.

Further measurements, with a spectral resolution of 4 cm$^{-1}$ and with the PEM peak retardation of $\lambda/2$ set for 1350 cm$^{-1}$ using 32× Cassegrain objectives with a numerical aperture of 0.65, were performed to evaluate the capabilities of the setup. Figure 4.4 shows the absorbance spectrum (Figure 4.4a) and the PM dichroic spectra (Figure 4.4b) of an 8 μm thin iPP film acquired with a microscope aperture size of 15 x 15 μm$^2$ using infrared synchrotron radiation and coadding 128 scans. The intrinsic sample reference axis was taken to be along the long edge of the polypropylene extrusion sheet. By appropriately positioning the sample this reference axis could be aligned with the coordinate system given by the orientation of the polarizer in front of the PEM and the moveable xy microscope stage which define an extrinsic reference direction. The observed absorption bands of the respective dichroic signals for the sample oriented at an angle of 0° between both reference axes were found to be in good agreement with the literature (see Table 4.1 for band assignments).[147] It should be noted that if the average orientation of a distinct dipole-transition moment is parallel to the reference direction, the dichroic absorption becomes positive, whereas a negative dichroic signal is observed for a perpendicular orientation of the dipole-transition moment. PM dichroic spectra were also collected for samples rotated by approximately 45° and 90°. Exact sample rotation with concomitant retention of sample position was not possible due to a shortcoming of the sample holder. Nevertheless, it can be seen that for the sample rotated by 90° the dichroic absorption bands are inverted with respect to the sample at 0° and that for the sample rotated by approximately 45° the measured dichroic signals become close to zero as expected.

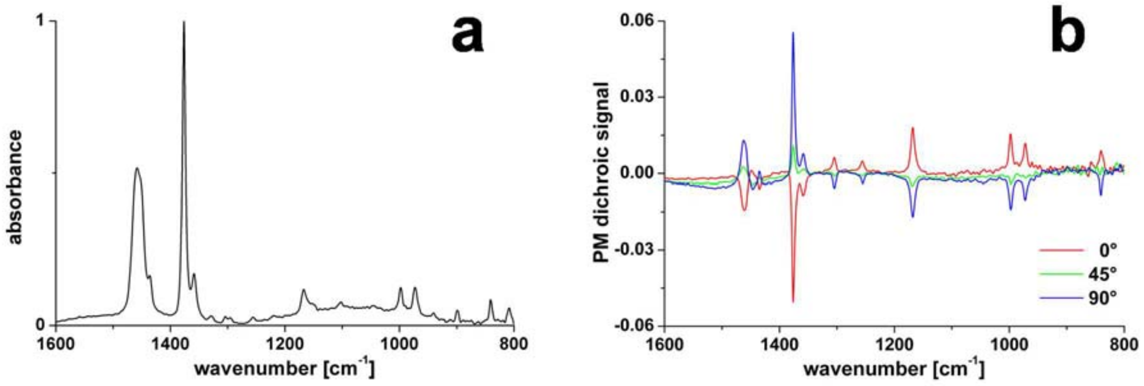

**Figure 4.4.** Absorbance spectrum (a) and polarization modulation (PM) dichroic spectra (b) of a thin film of isotactic polypropylene (8 µm). Spectra were acquired with a microscope aperture size of 15 x 15 µm$^2$ using infrared synchrotron radiation and coadding 128 scans.

**Table 4.1.** Band assignments of isotactic polypropylene according to the literature.[147]

| Band position [$cm^{-1}$] | Assignment |
|---|---|
| 1460, 1454 | antisymmetric deformation modes of $CH_3$ |
| 1435 | $CH_2$ bending vibration |
| 1377 | symmetric deformation mode of $CH_3$ |
| 1360 | CH bending with $CH_2$ twisting and wagging and symmetric $CH_3$ deformation |
| 1330 | $CH_2$ wagging with CH bending |
| 1304 | $CH_2$ wagging with $CH_2$ twisting and CH bending |
| 1254, 1220 | $CH_2$ twisting with CH bending |
| 1168 | axial C-C stretching with $CH_3$ rocking |
| 1103 | $CH_3$ rocking with axial C-C stretching |
| 1045 | C-methyl stretching with equatorial C-C stretching |
| 998 | $CH_3$ rocking with C-methyl stretching, CH bending and $CH_2$ twisting |
| 973 | $CH_3$ rocking with axial and equatorial C-C stretching modes |
| 941 | $CH_3$ rocking with axial C-C stretching |
| 899 | $CH_3$ rocking with $CH_2$ rocking and CH bending |
| 842 | $CH_2$ rocking with $CH_3$ rocking, equatorial C-C stretching and CH bending |
| 809 | $CH_2$ rocking with C-methyl stretching and equatorial C-C stretching |

Figure 4.5 illustrates the capabilities of the polarization modulation setup regarding spatial and temporal resolution. PM dichroic spectra of iPP acquired with an aperture of 30 x 30 $\mu m^2$ using infrared synchrotron radiation and collecting 4 or 128 scans respectively are presented in Figure 4.5a. As can be seen 4 scans seem sufficient to produce a spectrum with a reasonable S/N. Evidently, below 1000 $cm^{-1}$ S/N declines which is attributed to a deteriorating PEM efficiency in the long wavelength region of the spectrum. Increasing the number of scans to 128 clearly improves S/N so that weak dichroic signals become more distinguishable. Figure 4.5b shows spectra acquired from 24 and 128 scans collected with infrared synchrotron light and an aperture of 15 x 15 $\mu m^2$. Apparently, the decrease in aperture size compromises S/N. Still, the brilliance of the synchrotron source facilitates the collection of polarization modulation dichroic spectra of decent quality with an acceptable time resolution even at this aperture size.

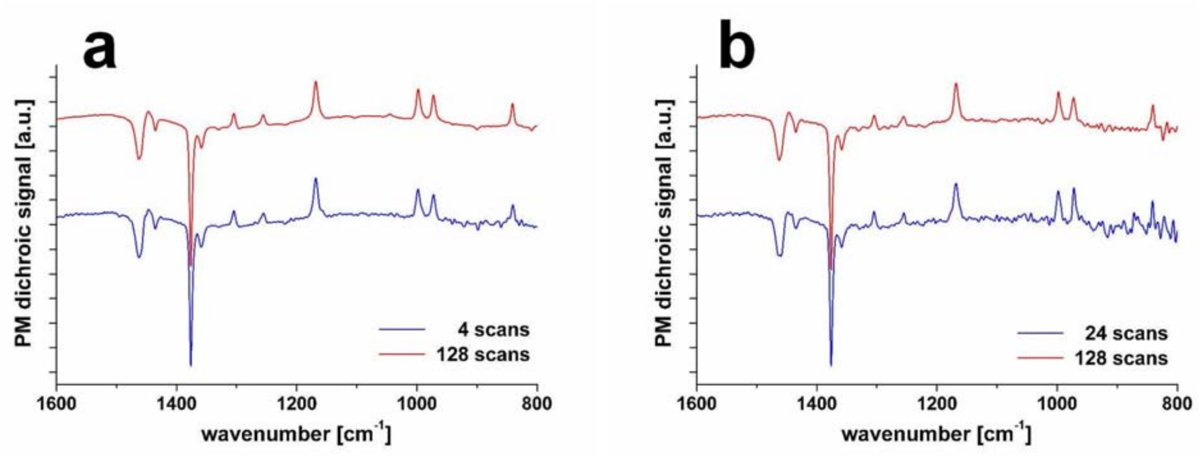

**Figure 4.5.** Polarization modulation (PM) dichroic spectra of isotactic polypropylene acquired with synchrotron radiation using apertures of 30 x 30 μm$^2$ (a) and 15 x 15 μm$^2$ (b).

The spectrum shown in Figure 4.6 was recorded with an aperture of 10 x 10 μm$^2$. The two parallel bands at 998 cm$^{-1}$ and 973 cm$^{-1}$ which are associated with methyl rocking modes[147] are still discernible. This means that for the given Cassegrain and dual aperture optics a spatial resolution which is diffraction-limited was achieved.[93] However, this diffraction-limited spatial resolution was attained at the expense of temporal resolution since for the spectrum shown 2048 scans were necessary. Thus, in principle diffraction-limited measurements with an aperture of 10 x 10 μm$^2$ are possible but from a practical point of view restricting the aperture size down to only 15 x 15 μm$^2$ seems reasonable.

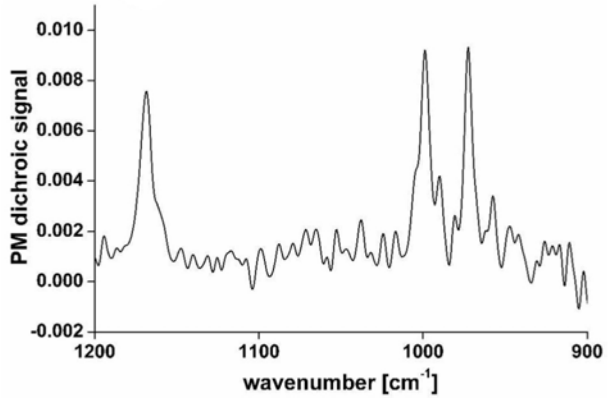

**Figure 4.6.** Polarization modulation (PM) dichroic spectrum of isotactic polypropylene acquired with synchrotron radiation using an aperture of 10 x 10 μm$^2$.

In Figure 4.7 a comparison between the infrared synchrotron and the conventional globar source (1300 K) is shown. For both cases polarization modulation dichroic spectra were recorded with an aperture size of 15 x 15 $\mu m^2$ collecting 512 scans. It is obvious that S/N is superior for the synchrotron source owing to its favourable brilliance, collimation and polarization characteristics. In order to achieve high spatial and temporal resolution as well as good sensitivity the use of infrared synchrotron radiation is essential.

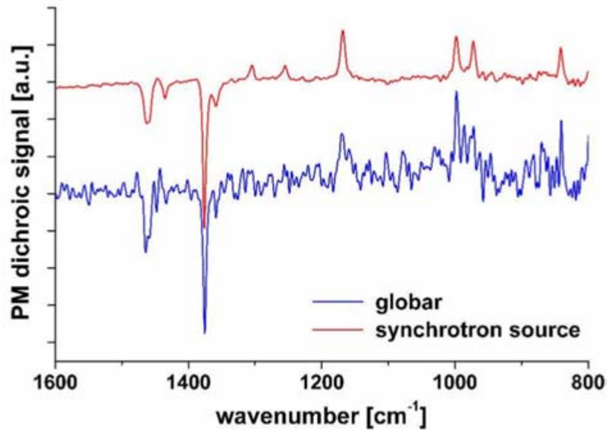

**Figure 4.7.** A source comparison between synchrotron and globar radiation for PM dichroic spectra of isotactic polypropylene recorded with an aperture size of 15 x 15 $\mu m^2$.

In the PM setup the difference spectrum and the sum background spectrum are acquired simultaneously at the same sample position. There is thus a reference-free inherent background collection in real-time. This means that for a PM dichroic spectrum instrumental fluctuations, such as beam instabilities and spectrometer drifts, as well as atmospheric changes over time become negligible in comparison to conventional polarized measurements without polarization modulation. For synchrotron radiation the simultaneous recording of a reference spectrum also provides an inherent normalization of the beam current and hence radiation intensity. Crucially, the need of a suitable reference for background collection vanishes. This alleviates sample measurement in aqueous solutions and other liquids because corrections for different liquid or solvent concentrations in the sample and reference beam paths become unnecessary. The observed dichroic signal is only sensitive to anisotropic contributions to absorption. Again, this makes the polarization modulation method attractive for sample measurement in for example aqueous solution because it is insensitive to the isotropic water background. The PM method is especially useful in cases where a suitable reference may not be available at all. The optical setup during measurement remains unchanged, and a sensitive time-resolved difference spectroscopy monitoring passive or actively induced changes of the sample becomes possible. The dichroic spectrum can be obtained directly without rotating either the polarizer or the sample. Rotation of microscopic samples with accurate repositioning is problematic and can thus be avoided. Non-repeatable viscoelastic phenomena may be studied by the PM method because the PM dichroic spectrum is recorded in a single measurement. Importantly, the combination of Fourier-transform infrared microspectroscopy with polarization modulation offers spatial resolution in addition to the spectral resolution of IRLD in anisotropic samples. Using infrared synchrotron radiation a diffraction-limited spatial resolution can be achieved. Good temporal resolution with good sensitivity is obtained down to very close to the diffraction limit. Therefore, using this method the reference-free and near-diffraction-limited mapping or imaging of IRLD seems to become a possibility. In the following, these capabilities are further explored and exploited.

### 4.1.2 Reflection Difference Measurements on Solid State Materials

A second set of test measurements was performed on solid state materials to further characterize the PM setup and to demonstrate the capability to carry out studies in reflection.[143] In particular, the transition metal oxides $Ca_{1.8}Sr_{0.2}RuO_4$, $Ca_{1.4}Sr_{0.6}RuO_4$ (both provided by Dr. J. S. Lee, BESSY, Berlin), and $Bi_{0.17}Ca_{0.83}MnO_{3+\delta}$ (provided by Prof. Dr. K. H. Kim, Seoul National University) were investigated. The anisotropic optical behaviour of these materials was interrogated using a 32× Cassegrain objective, an aperture size of 40 x 40 $\mu m^2$ and infrared synchrotron radiation.

$Ca_{2-x}Sr_xRuO_4$ ($x=0.2$ and 0.6) single crystals have a layered perovskite structure and are anisotropic due to a strong two-dimensionality. While they are metallic in the ab-plane, they are insulating along the c-axis. Figure 4.8a shows four PM dichroic (PM-LD) spectra of a $Ca_{1.4}Sr_{0.6}RuO_4$ sample with the anisotropic ac-plane oriented parallel to the reflecting surface in the mid-infrared spectral range between 7000 and 675 $cm^{-1}$. These four angle-dependent spectra represent the maximum, the minimum, and the two zero dichroic responses, respectively, obtained by rotating the sample by 0, 40, 80, and 130° around the axis normal to the surface. As a control, angle-dependent PM-LD spectra for rotation angles of 0, 45, 90, and 135° for an isotropic ab-plane of the $Ca_{1.8}Sr_{0.2}RuO_4$ sample are shown in Figure 4.8b. A dichroic signal very close to zero is found, independent of the azimuthal angle of the sample. A comparison of Figures 4.8a and b strongly suggests that the spectral behaviour observed in Figure 4.8a is based on the anisotropic optical reflection of the sample. All spectra in Figure 4.8 were recorded at a spectral resolution of 4 $cm^{-1}$ with the $\lambda/2$ peak retardation of the photoelastic modulator set for 2000 $cm^{-1}$, collecting 64 scans each.

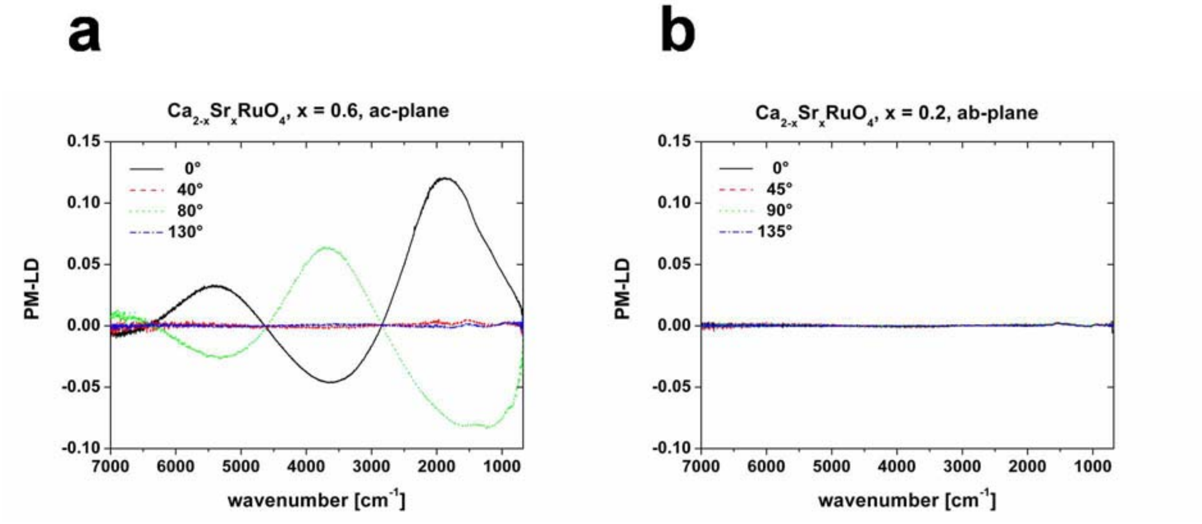

**Figure 4.8.** a) Angle-dependent PM dichroic (PM-LD) spectra of a $Ca_{1.4}Sr_{0.6}RuO_4$ sample with the anisotropic ac-plane oriented parallel to the reflecting surface. b) Angle-dependent PM-LD spectra for the isotropic ab-plane of a $Ca_{1.8}Sr_{0.2}RuO_4$ sample.

The spectral shapes of the two PM-LD spectra for 0 and 80° in Figure 4.8a resemble sinusoidal oscillations that decay towards higher wavenumbers, and they have multiple arches and nodes. This effect arises from the polarization modulation and, in particular, from the wavenumber-dependent modulator efficiency, i.e. the wavenumber-dependent phase retardation amplitude. It thus depends on the given $\lambda/2$ peak retardation setting of the photoelastic modulator. It was shown that the PM-LD spectra contain Bessel function factors that account for the wavenumber-dependent effectiveness of the modulator.[56] It is also known that there are discrepancies between experimental and theoretical values of the Bessel functions due to experimental artifacts.[99,102,110] As opposed to the alternative lock-in technique, the demodulation used in the present setup further complicates the theoretical and experimental comparison because contributions from higher harmonics of the second harmonic of the modulator frequency (i.e. 100 kHz) must be considered.[100,101] However, experimental calibration and normalization procedures for polarization modulation infrared reflection- absorption spectroscopy[99,102] and polarization modulation infrared linear dichroism measurements in transmission[58] have been established. Thus, in principle, the PM-LD spectra can be understood and compared to conventional polarized spectra obtained without polarization modulation. In the present setup, other detrimental effects, such as residual birefringence of the photoelastic modulator and polarization artifacts of the optical setup and the detector, are small compared to the optical response of the anisotropic sample (cf. Figures 4.8a and b).

In order to study the angular dependence of this dichroic response in more detail, a set of PM-LD spectra of the anisotropic ac-plane of the $Ca_{1.4}Sr_{0.6}RuO_4$ sample was recorded for rotation angles between 0 and 180°. Figure 4.9 shows the PM-LD response at 2000 $cm^{-1}$, i.e. the wavenumber for which the $\lambda/2$ peak retardation was set, as a function of the rotation angle. In a conventional polarized measurement the intensity shows a $\cos^2\theta$ dependence, where $\theta$ is the angle formed by the electric vector and the dipole-transition moment.[96] For measurements using polarization modulation, however, a $\cos(2\theta)$ dependence of the intensity is expected.[108] Here a simple mathematical expression is proposed as an approximation of the observed PM-LD response:

$$PM\text{-}LD_{\theta} = PM\text{-}LD_{0°}\,[a(\theta - 90°)^2 + b]\cos(2\theta).$$

This expression seems to describe the angular dependence of the PM-LD result reasonably well. The observed asymmetric behaviour in the experimental data may be due to a slight tilting of the sample surface with respect to the optical axis of the objective.

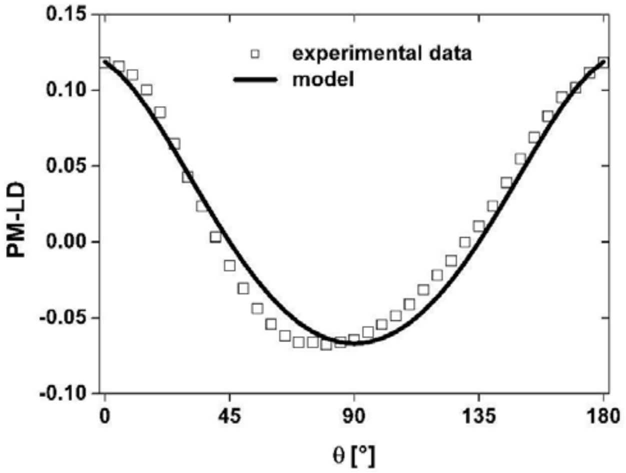

**Figure 4.9.** Angular dependence of the PM dichroic response of the anisotropic ac-plane of $Ca_{1.4}Sr_{0.6}RuO_4$.

Exploiting the mapping capability of the PM setup, the spatial distribution of the PM-LD signal in a $Bi_{0.17}Ca_{0.83}MnO_{3+\delta}$ sample was measured. Figure 4.10 shows the PM-LD spectra of the $Bi_{0.17}Ca_{0.83}MnO_{3+\delta}$ sample in the infrared spectral range between 5500 and 1500 $cm^{-1}$ which correspond to the horizontal line scan indicated in Figure 4.11a. For the measurements, the sample was mapped with a step size of 20 μm, collecting 128 scans at each measurement point. The maximum response of the PM-LD appears at about 4000 $cm^{-1}$, for which the $\lambda/2$ peak retardation of the PEM was set. The wavenumber-dependent PM-LD exhibits a notable variation, in magnitude but also in sign, as a function of position. While the magnitude of the PM-LD is a measure of the degree of anisotropy of the corresponding area, the sign indicates the direction along which the anisotropic axis is spatially oriented. Consequently, the results suggest that the line scan probed different anisotropic domains aligned along different directions.

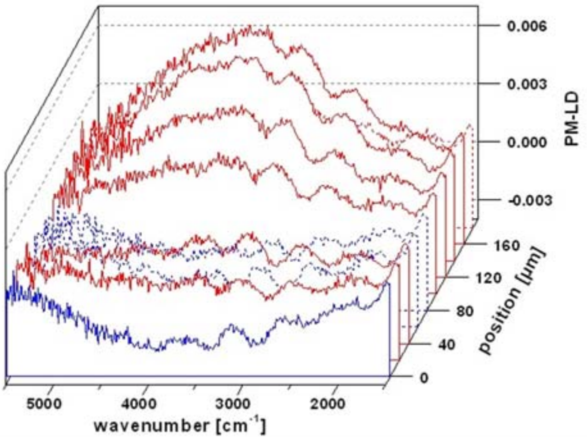

**Figure 4.10.** PM-LD spectra of a $Bi_{0.17}Ca_{0.83}MnO_{3+\delta}$ sample obtained by a line scan using an aperture size of 40 x 40 µm$^2$ and a step size of 20 µm.

This is seen more clearly in Figure 4.11a which shows the spatial distribution of the PM-LD signal at 4000 cm$^{-1}$ for the given area in the visible image in Figure 4.11d. The line profiles of the signal along the dotted lines indicated in Figure 4.11a are given in Figures 4.11b and c. While the PM-LD value for $Bi_{0.17}Ca_{0.83}MnO_{3+\delta}$ is much smaller than in the case of the totally anisotropic $Ca_{1.4}Sr_{0.6}RuO_4$ (cf. Figure 4.8a), the large contrast given by the change of the sign enables one to clearly distinguish between anisotropic domains with different anisotropic axes. At room temperature, $Bi_{0.17}Ca_{0.83}MnO_{3+\delta}$ has a pseudocubic, or more exactly orthorhombic, crystal symmetry. It is therefore suggested that the anisotropy observed in the measurement originates from the crystal symmetry. The mapping revealed the presence of different anisotropic domains in $Bi_{0.17}Ca_{0.83}MnO_{3+\delta}$, distributed inhomogeneously within tens of micrometers. It should be noted that all reflection measurements were performed without a reference sample. These results demonstrate that the experimental scheme is well suited to spatially and spectrally resolve anisotropy in solid state materials in the mid-infrared region.

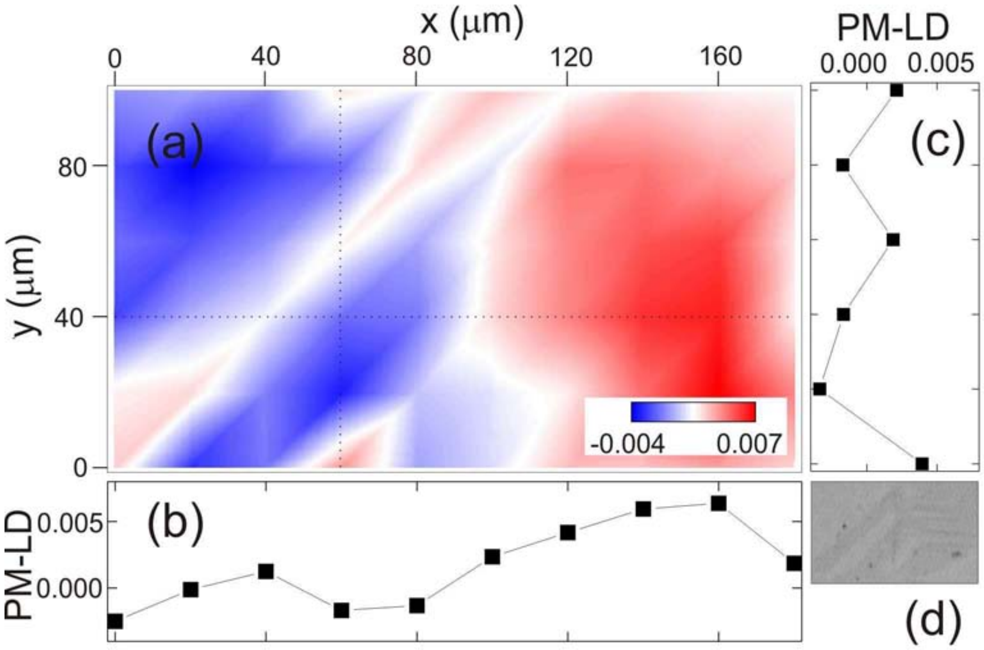

**Figure 4.11.** Spatial distribution (a) of the PM-LD signal at 4000 cm$^{-1}$ for a $Bi_{0.17}Ca_{0.83}MnO_{3+\delta}$ sample obtained by mapping with an aperture size of 40 x 40 μm$^2$ and a step size of 20 μm. Line profiles of the signal are given along the indicated horizontal line (b) and vertical line (c). The PM-LD image may be compared with the visible image (d) of the same sample area.

### 4.1.3 Polarized Measurements on Liquid Crystals

The capability of the PM method to obtain orientation information in reference-free measurements is of great potential. The method was applied in a preliminary study of liquid crystals. The measurements were performed using the liquid crystal E7 (Merck, cf. Figure 4.12a). The nematic-to-isotropic transition temperature of E7 is reported to be 60.5 °C.[148] Absorbance and PM dichroic spectra around the nitrile stretching mode at 2227 cm$^{-1}$ of E7 were measured in the anisotropic nematic phase at 50 °C and in the isotropic phase at 75 °C (see Figure 4.12b). For the unpolarized absorbance spectra, the nitrile band of E7 increases when the sample changes from nematic to isotropic, as was reported earlier in the literature.[148] By comparison, the PM dichroic spectra give a more pronounced discrimination of the two phases as the dichroic signal vanishes in the isotropic phase. PM measurements on liquid crystals can give additional information on orientation and, at the same time, may enhance the spectral contrast between different domains and phases. Given the spatial resolution, this method can be very useful to investigate the spatial distribution of liquid crystal domains and phases in response to, for example, chemical composition, temperature variations or electric fields.

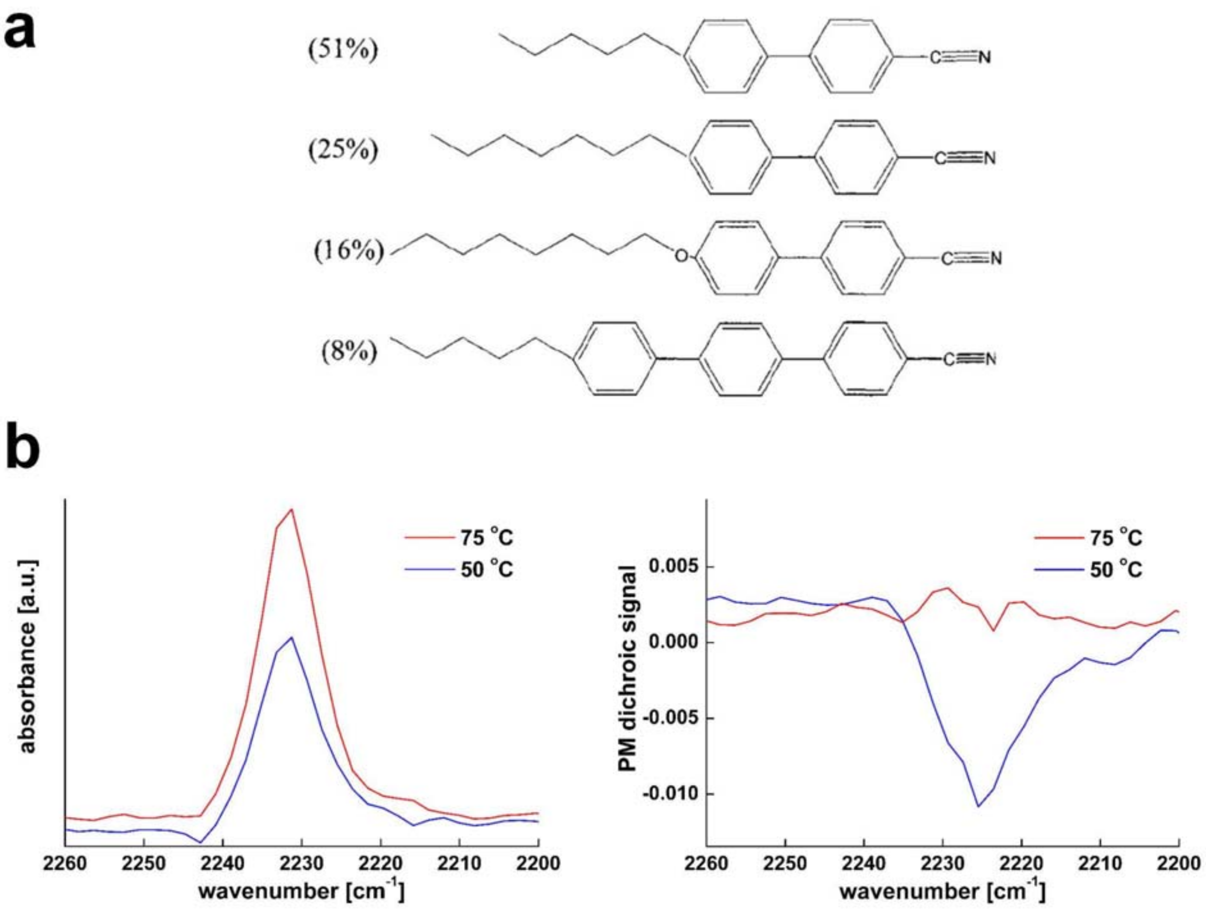

**Figure 4.12.** a) Composition of the liquid crystal E7. b) Absorbance spectra (left) and PM dichroic spectra (right) around the nitrile stretching mode at 2227 cm$^{-1}$ of E7 measured in the anisotropic nematic phase at 50 °C and in the isotropic phase at 75 °C.

## 4.2 PM Measurements on Synthetic and Biological Polymer Composites

### 4.2.1 Infrared Linear Dichroism in Polypropylene Model Composites

Polymeric materials are often heterogeneous and can contain both crystalline and amorphous regions and may have complex superstructures.[44] Such materials can also show anisotropic properties and sometimes polymorphism and they may be multicomponent systems such as polymer composites. It is therefore important to obtain spectroscopic information from heterogeneous polymeric materials at high spatial resolution in order to be able to characterize these complex systems with respect to composition, structure and orientation. Infrared microspectroscopy is a very useful tool for the characterization of such polymeric materials.[44,45,149] Fiber-reinforced thermoplastics are an important class of structural polymeric materials. They are of fundamental importance in the development of composite materials with attractive thermal and mechanical properties.[45] Systems based on isotactic polypropylene as the thermoplastic matrix and liquid crystal polymer (LCP) fibers as reinforcements are among fiber-reinforced model composites. The presence of fibers can modify the crystallization behaviour of polypropylene melts because the fiber surfaces provide heterogeneous nucleating sites. This can lead to preferentially oriented crystal growth perpendicular to the fiber axis yielding the so-called transcrystalline (TC) morphology with almost parallel superstructures within the iPP matrix.[44,45,149] Isotactic polypropylene exhibits three crystalline polymorphs where the monoclinic α modification predominates and the trigonal β modification rarely occurs.

In this work, the iPP matrices close to the LCP fibers of several thin film samples of iPP-LCP model composites (provided by Dr. G. Ellis, CSIC, Madrid) were investigated by polarized infrared transmission microspectroscopy using the PM setup.[150] Dichroic line and area maps for the microscopic discrimination of the morphology and for the characterization of the local microstructure in the samples were acquired. The samples were scanned with an aperture size of 15 x 15 $\mu m^2$ and a step size of 5 µm using 32× Cassegrain objectives and synchrotron radiation. All spectra were recorded at a spectral resolution of 4 $cm^{-1}$ with the $\lambda/2$ peak retardation of the photoelastic modulator set for 1150 $cm^{-1}$, collecting 256 scans each. Figure 4.13 shows the results of two line scans in α and β transcrystalline iPP matrices of iPP-LCP samples crystallized isothermally at 130 °C. In both cases distinct parallel and perpendicular dichroic bands (cf. Table 4.1 for band assignments) are observed. However, it is seen that in the case of β-TC iPP the magnitudes of the dichroic bands are larger and that the sign of the dichroic signals is inverted with respect to α-TC. In α iPP lateral growth or cross-hatching takes place[44] producing daughter lamellae that grow out tangentially at an angle of about 80°. This means that the average chain orientation in the α modification is averaged out to a considerable extent. By contrast, the average chain orientation is much higher in the β-TC phase because it does not contain daughter lamellae. Owing to the high spatial resolution which was near the diffraction limit and to the very good S/N, a pronounced periodic intensity variation of the dichroic bands as a function of distance from the fiber was detected in the β-TC phase. The origin of this observation seems to be based on the crystalline superstructure and may be due to a phenomenon called lamellar twisting.[151]

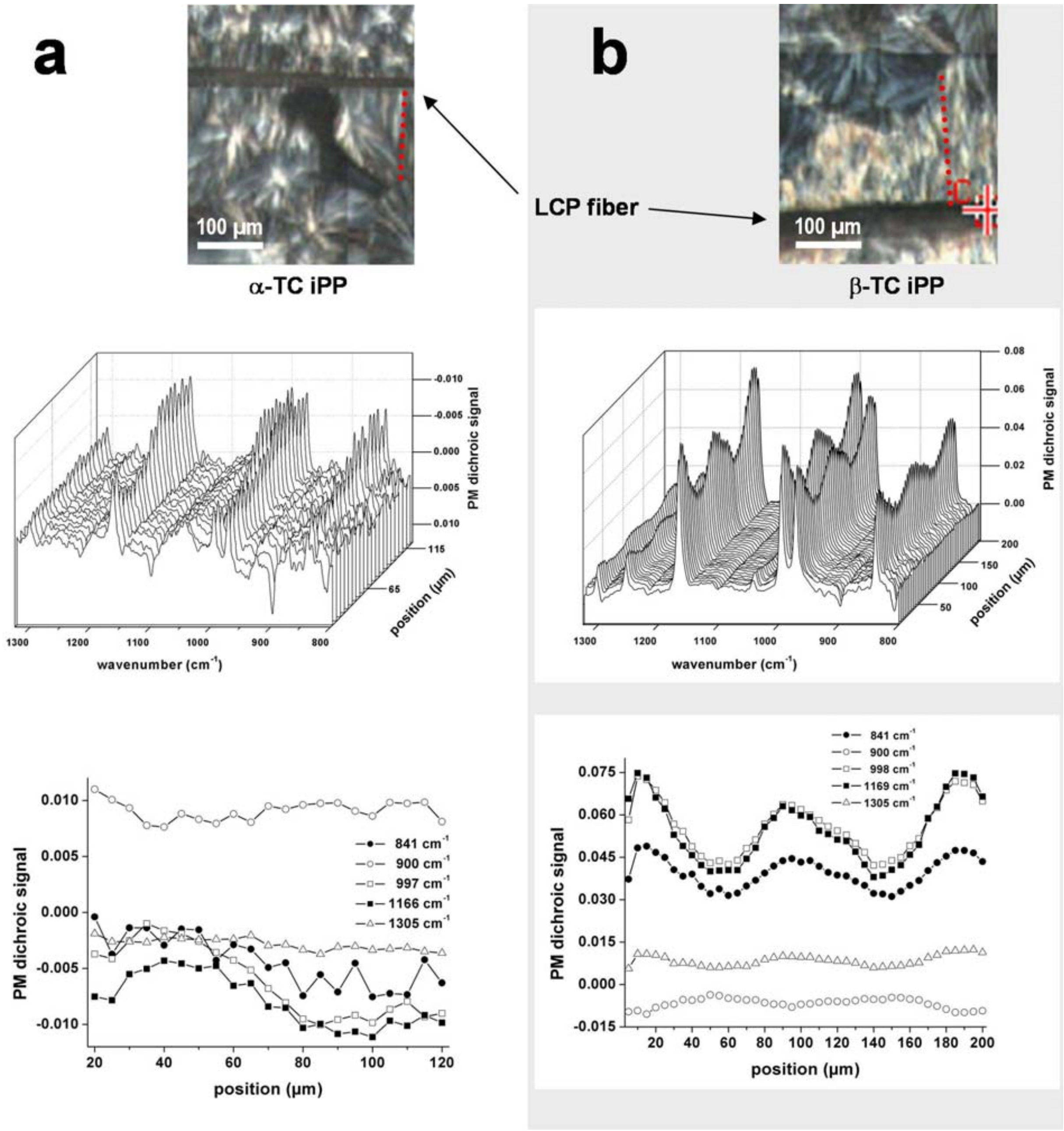

**Figure 4.13.** PM dichroic spectra (centre) of α transcrystalline (α-TC) (a) and β transcrystalline (β-TC) (b) isotactic polypropylene obtained from the line scans close to the liquid crystal polymer (LCP) fibers as indicated in the optical micrographs (top) by the red dotted lines. The aperture size was 15 x 15 µm$^2$ and the step size was 5 µm. Note that the ordinate in the PM dichroic spectra of α-TC (centre left) is inverted for a clearer representation. The line profiles for selected dichroic bands are also shown (bottom). A pronounced periodic intensity variation of the dichroic bands as a function of distance from the fiber is observed in the β-TC phase.

Figure 4.14 shows the result of a line scan, starting from the LCP fiber, in a TC iPP matrix of an iPP-LCP sample that underwent a step change in the crystallization temperature from 140 to 130 °C. This change in the crystallization temperature has been imprinted in the behaviour of several dichroic bands which change in magnitude and also in sign as the sample is scanned over the crystallization temperature edge. The crystallization temperature affects the average chain orientation and the degree of ordering and of lamellar branching. Interestingly, some dichroic bands appear to be unaffected by the change in crystallization temperature. The structural origin of these different behaviours still needs to be identified.

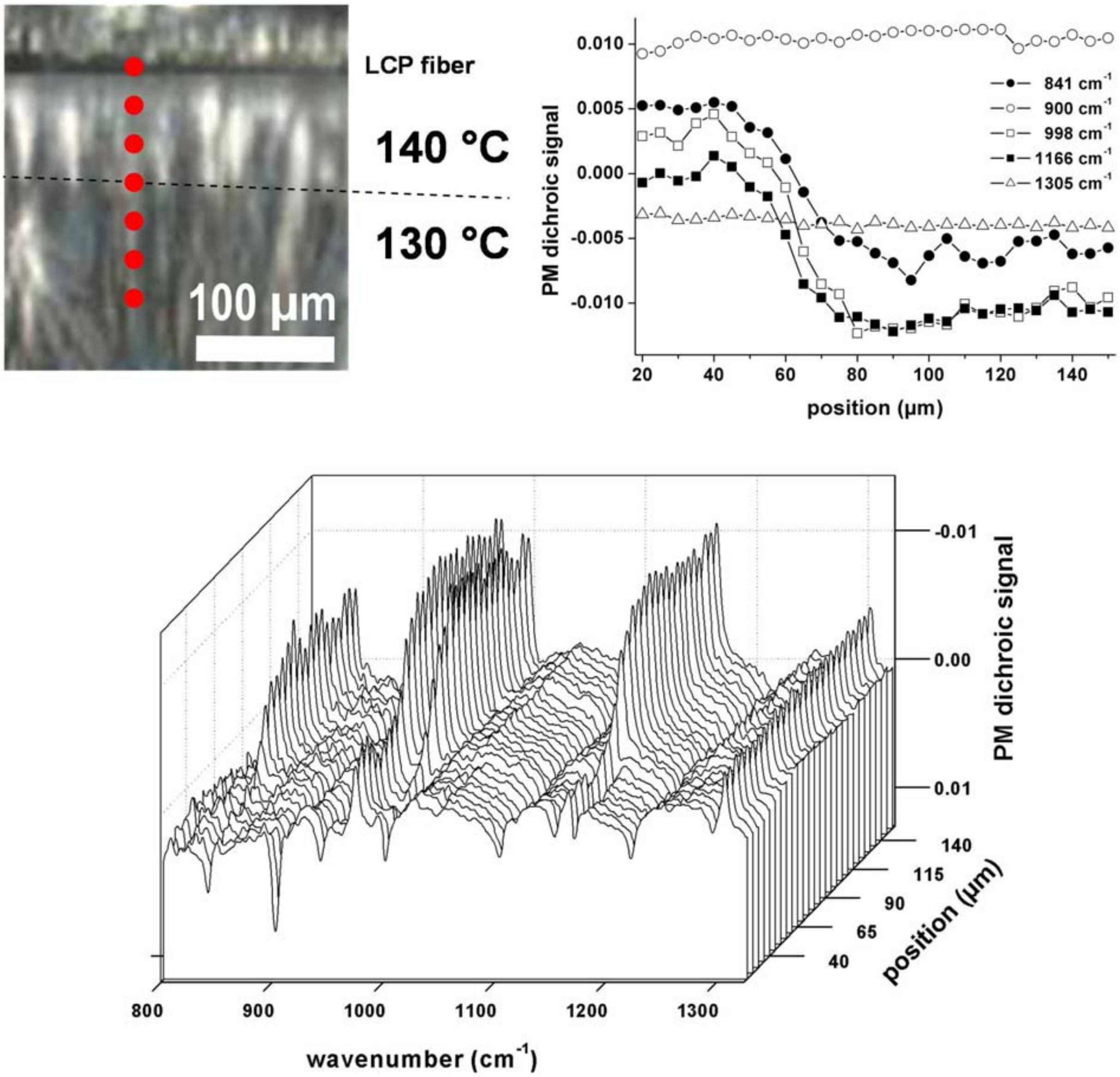

**Figure 4.14.** PM dichroic spectra (bottom) of a transcrystalline isotactic polypropylene matrix in an iPP-liquid crystal polymer (LCP) sample that underwent a step change in the crystallization temperature from 140 to 130 °C, obtained from the line scan starting close to the LCP fiber as indicated in the optical micrograph (top left) by the red dotted line. The aperture size was 15 x 15 µm$^2$ and the step size was 5 µm. Note that the ordinate in the spectra is inverted for a clearer representation. The line profiles for selected dichroic bands are also shown (top right).

The area of a polymorphic iPP matrix in an iPP-LCP sample was mapped, containing three regions with different crystalline morphologies, namely α-TC, spontaneous β phase and spherulitic iPP. The image shown in Figure 4.15b was obtained by integrating the PM dichroic signal between 1020 and 960 cm$^{-1}$, i.e. in the spectral region containing the two bands at 998 cm$^{-1}$ and 973 cm$^{-1}$ which are associated with methyl rocking modes.[147] This means that the reference-free and near-diffraction-limited mapping or imaging of IRLD in a polymeric material using the PM method was accomplished. The image reveals a heterogeneous spatial distribution of the dichroic signal and it agrees reasonably well with the optical micrograph (see Figure 4.15a) of the same area. The contrast in the infrared image is due to the different signs and magnitudes of the dichroic signal. Overall, the results on iPP-LCP composites demonstrate the capability of the PM method to study the spatial distribution of IRLD in heterogeneous polymeric samples. The mapping capabilities of the setup along with the good sensitivity allow one to obtain information on molecular chain orientation and crystalline superstructures and to distinguish spectrally and spatially between crystalline morphologies.

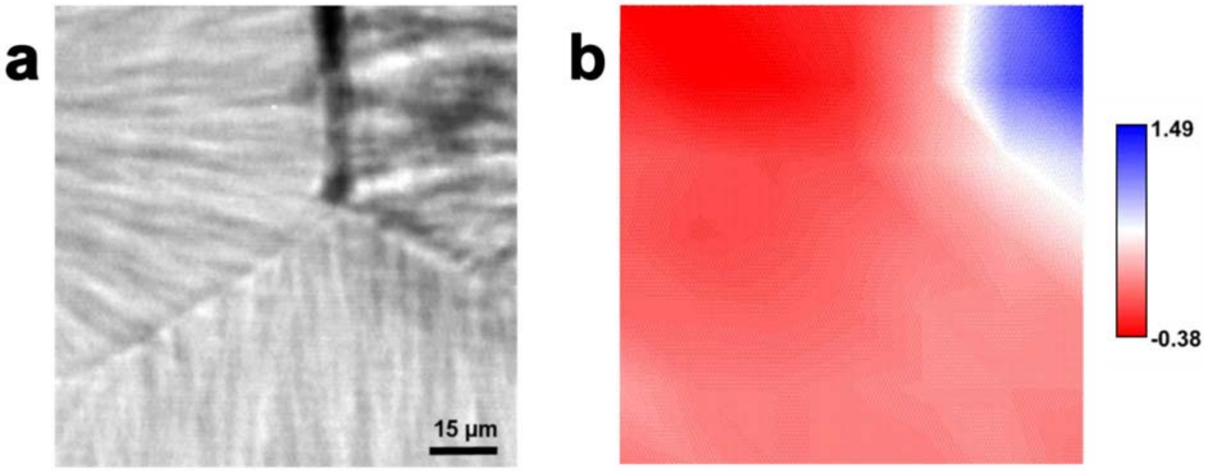

**Figure 4.15.** a) Optical micrograph of an isotactic polypropylene matrix in an iPP-LCP sample containing α transcrystalline (bottom), spontaneous β (top right) and spherulitic (top left) morphologies. b) IRLD image obtained by mapping the area with an aperture size of 15 x 15 µm$^2$ and a step size of 5 µm and integrating the PM dichroic signal between 1020 and 960 cm$^{-1}$.

### 4.2.2 Polarized Infrared Measurements on Single Wood Fibers

Cell walls are crucial components of plants. In addition to their role in maintaining cell structure, these extracytoplasmic matrices have many other functional properties.[152] In the case of wood cells, the cell walls are composed of cellulose, hemicelluloses, lignin and a relatively small amount of molecules with low molecular weights (extractives). The cellulose molecules form stretch-resistant microfibril aggregates. These aggregates are embedded in a compression-resistant matrix of other polysaccharides (hemicelluloses) as well as polyphenol macromolecules (lignin). The unique physical and mechanical properties of wood fibers are chiefly determined by the complex arrangement of and the interplay between the different wood polymers within the cell wall.[153] However, the exact arrangement and interactions of the different constituents, especially at the ultrastructural level, are not yet fully understood.

Cellulose constitutes the major polymer of the wood cell wall. The basic macromolecular units of this polysaccharide are unbranched poly-β-(1,4)-D-glucopyranose (glucan) chains (see Figure 4.16). In the cell walls these glucan chains are aggregated to form more complex supramolecular structures. This aggregation of individual chains into higher order structures is controlled by the intricate processes involved in cellulose biosynthesis.[152,154,155] Crystalline regions form microfibrils but less ordered or amorphous domains are also present. Importantly, in the crystalline domains the hydroxyl groups of the glucose residues engage in ordered hydrogen bond systems, both within and between the cellulose chains.[156] Intramolecular hydrogen bonding is important for the conformation of individual chains, whereas intermolecular hydrogen bonding is significant in forming the supramolecular aggregates. Crystalline cellulose can exist in different allomorphs, the metastable cellulose I being the most prevalent native crystalline form.[152,154] Cellulose I is made of parallel glucan chains in a flat-ribbon conformation and has strong intramolecular hydrogen bonds. In fact, there are two sub-allomorphs, $I_\alpha$ and $I_\beta$.[157] Both can co-exist in a cell wall but cellulose $I_\beta$ is known to be the dominant form in cell walls of higher plants.[157,158]

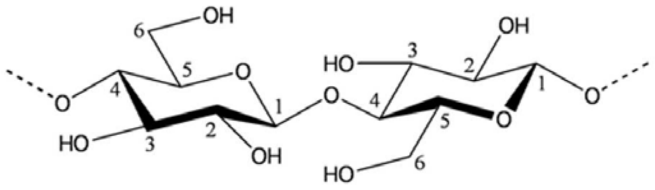

**Figure 4.16.** Schematic drawing of the repeating unit of the β-(1,4)-glucan polymer chain (cellulose).

In wood the cellulose microfibrils are embedded in the hemicelluloses-lignin matrix and a close interaction or cooperative mixing between the various wood polymers is implied.[153] The different constituents are interrelated and each fulfills essential functional and structural roles in the biocomposite. Compared to xylan polysaccharides, glucomannan polysaccharides are thought to have a closer association with the cellulose microfibrils in spruce fibers. Both these hemicelluloses show signs of an ordered structure.[153] Some degree of ordering in lignin is also evident and it may be inferred that lignin arrangement in the cell wall is related to or dependent on the oriented and templating structure of the polysaccharides.[159,160] The various linkages between the phenyl-propane units within the lignin macromolecules create a three-dimensional polymer network well suited as an adaptable matrix material.

Infrared spectroscopy seems to be a well suited tool to gain a further understanding of the complex architecture of wood cell walls. Firstly, it can give information on both crystalline and non-crystalline phases. Secondly, the morphology of the cell walls is based on hierarchically built structures and it is governed by various factors on different length scales (see Figure 4.17 for a schematic illustration of the wood cell wall). These include the configuration and orientation of submolecular units, macromolecular conformations, intermolecular interactions and supramolecular arrangements, and degrees of ordering of the wood polymers. Infrared spectroscopy may give access to compositional and structural information from the different levels.

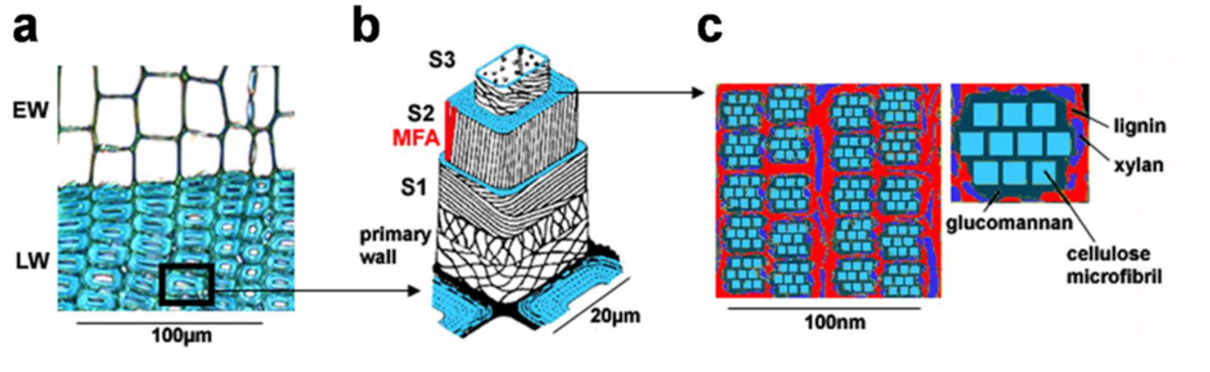

**Figure 4.17.** Hierarchical structure of wood: a) earlywood (EW) for water transport and latewood (LW) for mechanical support; b) layered structure of the cell wall with changing microfibril angle (MFA) (modified after Ref. 161); c) composite structure within the S2 layer of the secondary wall: microfibrils embedded in a matrix of hemicelluloses (xylan and glucomannan) and lignin (modified after Ref. 162).

In this work, in collaboration with the Abteilung Biomaterialien of the Max-Planck-Institut für Kolloid- und Grenzflächenforschung, wood polymers in their native composite structure using single spruce fibers were investigated in order to probe the wood polymers *in situ* in their native cell wall environment.[142] Dichroic infrared spectra of fibers placed in the custom-built microfluidic cuvette were acquired in air, in liquid (heavy) water and in liquid dimethylacetamide. A tangential section (200µm) of spruce (*Picea abies* [L.] Karst.) wood was cut on a rotary microtome (LEICA RM2255, Germany) and single wood fibers (tracheids) were mechanically isolated by a peeling out with fine tweezers.[163] This mechanical isolation procedure makes possible to work on the unmodified cell wall in its native state.[164] All PM dichroic spectra were recorded using a square aperture of 40 µm side length which was smaller than the lateral dimension of the fibers. The spatial resolution of the measurement was thus sufficient to investigate single fibers, rather than fiber bundles which may contain both optically dense and transparent regions which would give rise to stray light problems.[97] Spectra were recorded with the $\lambda/2$ peak retardation of the photoelastic modulator set for 3350 cm$^{-1}$. 32× Cassegrain objectives and an MCT detector were used for the microscopic measurements in transmission. The spectral resolution applied was 4 cm$^{-1}$ and 2048 scans were collected for each PM dichroic spectrum. For all spectra a base line offset with respect to 3800 cm$^{-1}$ was applied.

Figure 4.18a shows a representative infrared absorbance spectrum between 4000 cm$^{-1}$ and 1000 cm$^{-1}$ of single spruce fibers in air. There are abundant spectral signatures, especially below 1800 cm$^{-1}$, where bands from the various molecular constituents are superimposed to yield a complex spectral pattern.[153] There is also a broad band between 3700 cm$^{-1}$ and 3000 cm$^{-1}$ due to O–H stretching vibrations. This spectral region is very useful for sensitive measurements of hydrogen bonding.[165] However, due to the overlap of distinct bands, detailed information on hydrogen bonding is hidden in the broad and mostly unstructured absorption band.[158,166] Several strategies have been used to resolve and to interpret these overlapping bands. Polarized infrared spectroscopy has been employed in studies on cellulose to distinguish between the different hydroxyl groups and their respective orientation, and to explore possible hydrogen bonding patterns.[167-170] Deuteration techniques,[171-173] also in conjunction with polarized light,[165,174] have been utilized to assess the accessibility of hydroxyl groups and to distinguish amorphous and crystalline domains in cellulose. Second derivative[175,176] and deconvolution[166,177] processing of cellulose spectra have also resulted in a better resolution of O–H stretching bands.

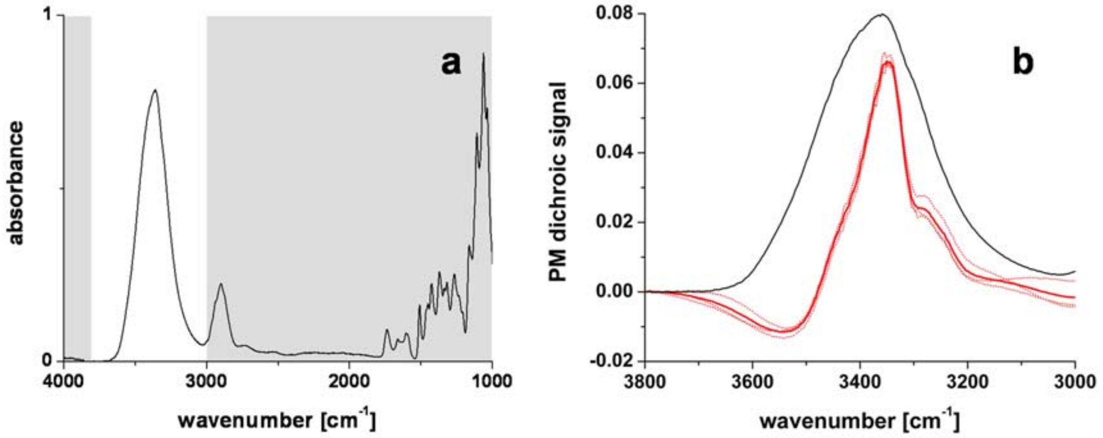

**Figure 4.18.** a) A representative infrared absorbance spectrum between 4000 cm$^{-1}$ and 1000 cm$^{-1}$ of single spruce fibers (average of measurements of three fibers) in air. Emphasis is put on the O–H stretching frequency region where a broad and mostly unstructured band is observed (the rest of the spectrum is shaded in gray).
b) Polarization modulation dichroic spectra between 3800 cm$^{-1}$ and 3000 cm$^{-1}$ of three single spruce fibers in air (dotted red lines), and the average of the three measurements (solid red line) are presented. The unpolarized absorbance spectrum from Figure 4.18a (in arbitrary units) is superimposed (black line).

In Figure 4.18b the PM dichroic spectra between 3800 cm$^{-1}$ and 3000 cm$^{-1}$ of three single spruce fibers measured in air within the microfluidic cuvette are presented. The PM dichroic spectra comprise only anisotropic contributions of absorption from O–H groups and exhibit more spectral details compared to the unpolarized spectrum (see black line in Figure 4.18b). To improve the signal-to-noise ratio and to account for diversity between fibers the average of three single fiber measurements was calculated (Figure 4.18b) and used for further evaluation. One negative band and several positive bands are discernible as either peaks or shoulders. Note that the dichroic signal is positive if the average orientation of a given dipole-transition moment is parallel to the fiber direction. Conversely, for a perpendicular orientation of the dipole-transition moment a negative signal is observed. The position of a band reflects the strength of hydrogen bonding. Bands originating from hydrogen bonded O–H groups are red shifted and increase in intensity with increasing hydrogen bond strength relative to free O–H groups.[165] Thus, orientation, position and intensity of the dichroic bands indicate the hydrogen bonding patterns and the structural arrangements in the fiber cell wall.

In order to identify the bands and their exact peak positions more clearly the second derivative (Norris derivative, 23-point segment length, 8-point gap) spectrum was calculated from the averaged PM dichroic spectrum (see Figure 4.19). Minima, deriving from positive bands in the dichroic spectrum, appear at 3241 cm$^{-1}$, 3275 cm$^{-1}$, 3340 cm$^{-1}$ and 3451 cm$^{-1}$. Shoulders in the second derivative spectrum at 3375 cm$^{-1}$ and 3432 cm$^{-1}$ are also identified.

The broad negative signal in the dichroic spectrum at 3548 cm$^{-1}$ is not resolved in the second derivative spectrum.

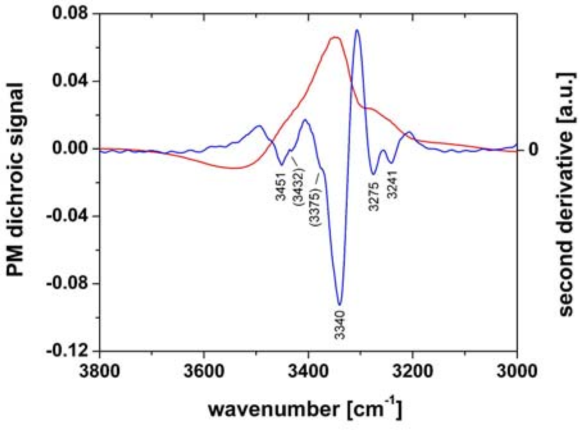

**Figure 4.19.** Average PM dichroic spectrum between 3800 cm$^{-1}$ and 3000 cm$^{-1}$ of three single spruce fiber measurements in air (red line) and its calculated second derivative spectrum (blue line, in arbitrary units). Bands seen as shoulders in the second derivative spectrum are shown in brackets.

Given the complex composite nature of the cell wall assembly and structure it is of interest to discriminate between the hydroxyl groups of the different wood polymer components and also residual weakly bound water. Due to different accessibility of water molecules to the structural units of the hydrophilic wood polysaccharides the spectral changes in aqueous environment were investigated to reveal further insights. The introduction of water to the dry fibers leads to filling of the lumen and hydration of the partially hydrated and accessible structures. Existing inter- and intramolecular hydrogen bonds may be weakened, ruptured or reoriented due to the presence of water thus causing structural perturbations and rearrangements. Despite the low path length of the microfluidic cuvette, spectra in the region between 3700 cm$^{-1}$ and 3000 cm$^{-1}$ of fibers in $H_2O$ could not be recorded due to total absorption. Therefore, heavy water ($D_2O$) was used for the measurements. It is important to note that $D_2O$ converts accessible O–H groups to O–D groups due to the H-D exchange reaction. Intracrystalline domains of cellulose are known to be devoid of water.[165] By contrast, water molecules can be inserted in non-crystalline regions of cellulose and at accessible crystal surfaces and interfaces where the crystalline cellulose network is disrupted.[165,172,173] Thus, it is possible to distinguish the hydroxyl groups of inaccessible cellulose fibrils from those of accessible cellulose surface chains and amorphous cellulose[171] and presumably from hydroxyl groups of the less ordered or amorphous hemicelluloses-lignin matrix.[178]

The average PM dichroic spectrum of three single fiber measurements in liquid $D_2O$ is shown in Figure 4.20. The spectrum is derived from the same single fibers previously measured in air (cf. Figures 4.18b and 4.20) thus reflecting the *in situ* spectral differences due to the change in ambient conditions. Differences are found in band intensities rather than band positions or orientations. The three parallel bands at 3241 $cm^{-1}$, 3275 $cm^{-1}$ and 3340 $cm^{-1}$ are more intense, whereas all other bands show decreased intensities.

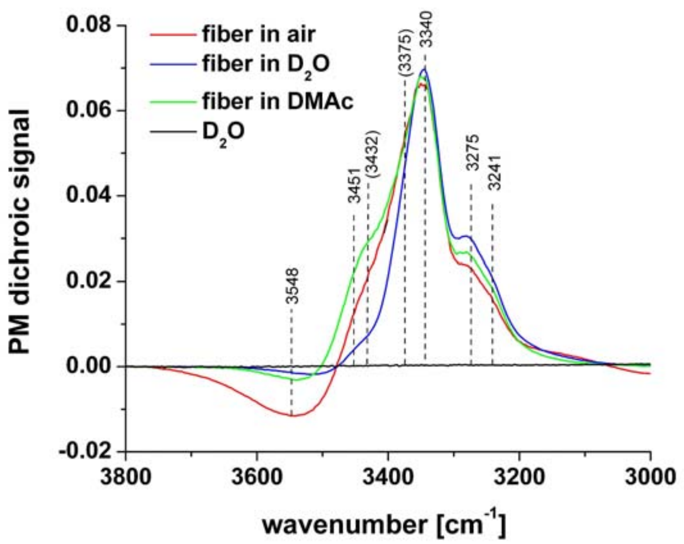

**Figure 4.20.** PM dichroic spruce fiber spectra (each an average of three single fiber measurements) recorded in air, liquid $D_2O$ and liquid DMAc, and a background ($D_2O$ in the microfluidic cuvette) spectrum as control.

In order to obtain further access to structural information liquid dimethylacetamide (DMAc) instead of $D_2O$ was used in a separate experiment. It is known from the work of Björkman[179] that DMAc influences the spruce wood structure due to solvation and swelling effects. DMAc molecules are also polar but they are larger in size compared to $D_2O$ molecules and serve as hydrogen bond acceptors only. Moreover, they lack N–H and O–H functionalities so they do not contribute to the absorption in the spectral region of interest or engage in H-D exchange reactions. The PM dichroic fiber spectrum in DMAc exhibits spectral differences with respect to the fiber spectra recorded both in air and $D_2O$ (see Figure 4.20). The perpendicular band around 3548 $cm^{-1}$ is noticeably weaker than for fibers in air, but somewhat more intense compared to $D_2O$. For the parallel bands at 3241 $cm^{-1}$, 3275 $cm^{-1}$

and 3340 cm$^{-1}$ the intensities are similar to the cases of air and $D_2O$. The parallel band around 3451 cm$^{-1}$ is more intense in DMAc than in air. Figure 4.20 also shows the PM dichroic spectrum of liquid $D_2O$ recorded in the cuvette as a control.

Taking advantage of the microfluidic cuvette, supplementary experiments were performed on the drying of fibers from $D_2O$ and the reintroduction of $D_2O$ into fibers (see Figure 4.21a). The obtained spectra indicate a relatively high degree of reversibility. The O–D stretching frequency region of the spruce spectra becomes accessible when fibers are drying from $D_2O$. Therefore, bands originating from various species (DO–D, HO–D, CO–D) in the accessible regions of the fiber walls previously penetrated by $D_2O$ could be observed. Figure 4.21b shows two PM dichroic fiber spectra between 3800 cm$^{-1}$ and 2200 cm$^{-1}$ for fibers drying from $D_2O$. Five bands in the O–D stretching frequency region are identified, namely four parallel bands at 2418 cm$^{-1}$, 2443 cm$^{-1}$, 2492 cm$^{-1}$ and 2544 cm$^{-1}$, and a perpendicular band around 2600 cm$^{-1}$.

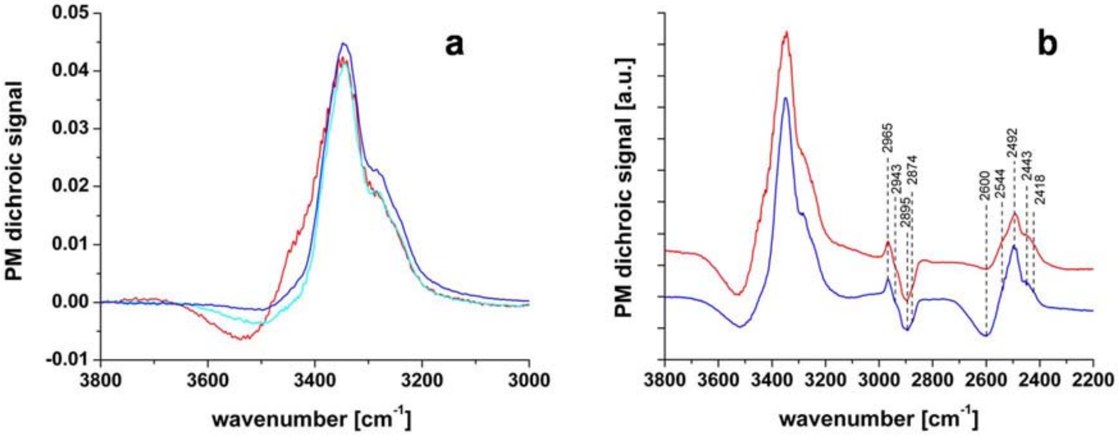

**Figure 4.21.** a) PM dichroic spectra of single measurements of a fiber in $D_2O$ (cyan line), drying from $D_2O$ (red line) and exposed to $D_2O$ again (blue line). b) PM dichroic spectra between 3800 cm$^{-1}$ and 2200 cm$^{-1}$ for fibers drying from $D_2O$ (each an average of three single fiber measurements, shifted in the ordinate for clarity and in arbitrary units). Both spectra represent two intermediary stages during the drying process.

According to the literature (see Table 4.2) a vibrational band at approximately 3630 cm$^{-1}$ characterizes free, i.e. non-hydrogen-bonded O–H groups of water[177] or alcohols.[180] This means that all dichroic bands that were identified (see Table 4.3 for band assignments for spruce fibers) in the O–H stretching region originate from O–H groups involved in hydrogen bonding. The two parallel bands at 3241 cm$^{-1}$ and 3275 cm$^{-1}$ are shifted most and therefore indicate groups with the strongest hydrogen bonds in the samples. Their persistence in the presence of $D_2O$ and DMAc suggests that these bands originate from O–H groups of inaccessible cellulose fibrils. The assignments of the band at 3241 $cm^{-1}$ to $I_\alpha$ cellulose and of the band at 3275 $cm^{-1}$ to $I_\beta$ cellulose are in good agreement with the work of Sugiyama *et al.*.[169] The appearance of both bands is a sign of the co-existence of the two cellulose sub-allomorphs in the spruce cell walls. Maréchal and Chanzy[165] found a parallel band at 3270 $cm^{-1}$ in $I_\beta$ cellulose and assigned it to the secondary alcohols C2O2–H (cf. Figure 4.16 for nomenclature) establishing relatively strong hydrogen bonds on O6 atoms of primary alcohols of the same chain. They also noted that this type of intramolecular hydrogen bonding is accomplished by only a minor conformation which accounts for less than one third of C2O2–H alcohols. This assignment may be corroborated by looking at the most intense and parallel band at 3340 $cm^{-1}$. It also stems from crystalline cellulose and was attributed to the secondary alcohols C3O3–H, each of which have an intramolecular hydrogen bond with the ring oxygen O5 of an adjacent glucose unit.[165,167] The observed relative intensities of the bands at 3275 $cm^{-1}$ and at 3340 $cm^{-1}$ support the earlier assignment of Maréchal and Chanzy.

**Table 4.2.** Band assignments of O–H vibrations according to the literature.

| Band position [$cm^{-1}$] | Assignment | Band orientation |
|---|---|---|
| ~ 3630 | non-hydrogen-bonded OH groups of water[a] or alcohols[b] | |
| 3540 | weakly hydrogen bonded OH groups of alcohols[b] | |
| 3447 | 2,3-di-O-methylcellulose (model compound for amorphous cellulose)[c] | |
| 3420 | amorphous cellulose[c] | |
| 3340 | cellulose I; O3–H…O5 intramolecular[d, e] | $\parallel$ |
| 3270 | cellulose $I_\beta$[f] | |
| 3270 | cellulose $I_\beta$; O2–H…O6 intramolecular[e] | $\parallel$ |
| 3240 | cellulose $I_\alpha$[f] | $\parallel$ |
| 2615 | free OD groups of $D_2O$ in cellulose[e] | |

[a] Ref. 177; [b] Ref. 180; [c] Ref. 181; [d] Ref. 167; [e] Ref. 165; [f] Ref. 169

The band around 3548 $cm^{-1}$ is indicative of O–H groups with a perpendicular orientation to the fiber axis and very weak hydrogen bonding. It originates, at least predominantly, from molecules in the amorphous or less ordered regions of the fiber cell walls since it strongly decreases in the presence of $D_2O$ or DMAc. The hemicellulose glucomannan was shown to sorb water more strongly than cellulose[178] and it is plausible that the less ordered or amorphous hemicelluloses matrix in wooden cell walls can be penetrated by water molecules relatively easily. Thus, an assignment of the band at 3548 $cm^{-1}$ to weakly hydrogen bonded water in the amorphous or less ordered regions of cellulose and hemicelluloses is reasonable. This assignment implies a preferred orientation or structuring of the water molecules involved. A distinction of weakly bound water from liquid water seems inappropriate here and deserves a more specific investigation and detailed proof. Weakly hydrogen bonded O–H groups of alcohols are an alternative or additional source of the band.[166,180] The effect of $D_2O$ and DMAc on the band intensity is similar. The decrease in intensity may be attributed to the disruption of the original hydrogen bonds by solvation and, since no band at higher wavenumbers appears in the fiber spectra recorded in either $D_2O$ or DMAc, to a randomization of orientation. Furthermore, in $D_2O$ the H-D exchange reaction depletes the accessible O–H groups. Thus, the O–H groups involved must be sterically easily accessible and conformationally flexible. Still, a more precise band assignment to water or alcohols seems not feasible. Also, a small residual negative dichroic signal is observed in the presence of both $D_2O$ and DMAc. This suggests that there is either imperfect penetration of the liquid molecules in the less ordered cellulose domains and in the heterogeneous matrix, an incomplete loss of preferred molecular orientation of the O–H groups in the less ordered regions, or dichroic absorption contributions from crystalline cellulose. Evidence from nuclear magnetic resonance studies indicates that cellulose chains at fibril or crystallite surfaces are in part inaccessible to solvent.[182,183]

**Table 4.3.** Assignments of bands[a] for spruce (*Picea abies* [L.] Karst.) fibers.

| Band position [$cm^{-1}$] | Assignment | Band orientation |
|---|---|---|
| 3548 | weakly hydrogen bonded OH groups of water and/or alcohols in the amorphous or less ordered regions of the fiber cell walls | ⊥ |
| 3451 | OH groups of alcohols in the amorphous or less ordered regions of the fiber cell walls | ‖ |
| 3432 | possibly OH groups of alcohols | ‖ |
| 3375 | possibly OH groups of alcohols | ‖ |
| 3340 | cellulose I | ‖ |
| 3275 | cellulose $I_\beta$ | ‖ |
| 3241 | cellulose $I_\alpha$ | ‖ |
| 2965 | CH groups | ‖ |
| 2943 | | ⊥ |
| 2895 | | ⊥ |
| 2874 | | ⊥ |
| 2600 | hydrogen bonded OD groups | ⊥ |
| 2544 | | ‖ |
| 2492 | | ‖ |
| 2443 | | ‖ |
| 2418 | | ‖ |

[a] corresponding to Figures 4.19, 4.20 and 4.21b

The parallel band at 3451 $cm^{-1}$ originates mainly from O–H groups in the less ordered or amorphous regions of the cell walls because it is strongly influenced by the presence of $D_2O$ or DMAc. In contrast to the band around 3548 $cm^{-1}$, the band at 3451 $cm^{-1}$ is affected by $D_2O$ and DMAc in clearly different fashions. In $D_2O$ the band intensity is greatly decreased compared to the fiber spectrum in air, whereas in DMAc it is increased. The decrease of intensity of the band at 3451 $cm^{-1}$ in the presence of $D_2O$ may be attributable to the H-D exchange reaction. The augmentation of the band in the presence of DMAc may suggest a higher degree of ordering. However, it is necessary to also consider that this parallel band may become more prominent due to the strong decrease of the broad opposing negative band around 3548 $cm^{-1}$. Apparently there is no loss of orientational preference so the groups at the origin of the band are conformationally less flexible. A band assignment to O–H groups of alcohols is indicated. The band position is in approximate agreement with literature values for amorphous cellulose.[181] However, O–H groups of the other wood polymers may also contribute to the absorption. Both the bands at 3451 cm$^{-1}$ and 3548 cm$^{-1}$ originate from the so-called amorphous regions of the fiber walls. The presence of these two dichroic signals immediately implies some degree of ordering and structural anisotropy. This is further evidence that the structural organization in these regions is to some degree ordered.

The two bands at 3375 cm$^{-1}$ and 3432 cm$^{-1}$ that were observed as shoulders in the second derivative spectrum in Figure 4.19 may be due to O–H groups of alcohols. It is likely that other oriented weaker bands cannot be identified because they are masked by the stronger bands. This could explain the observed differences for the bands at 3241 cm$^{-1}$, 3275 cm$^{-1}$ and 3340 cm$^{-1}$ in air, in $D_2O$ and DMAc.

When fibers are drying from $D_2O$ it becomes possible to observe bands in the O–D stretching frequency region of the spruce spectra (see Figure 4.21b). Overall, these bands appear less intense than the O–H bands. This suggests that there is a comparatively smaller number of oriented O–D groups available to contribute to the absorptions, or that the involved O–D groups have less preferential orientation longitudinally or perpendicular to the fiber axis. The pattern of the bands bears some resemblance to the O–H stretching frequency region. However, unlike in the O–H stretching region, the O–D bands originate only from groups in the less ordered regions of the fiber walls and have no contributions from crystalline cellulose where H-D exchange cannot take place. The appearance of these dichroic bands is another manifestation of structural anisotropy and some degree of ordering in the non-crystalline domains of the fiber cell walls. Free O–D groups of $D_2O$ in cellulose are reported to have a band at 2615 cm$^{-1}$.[165] This suggests that all the observed O–D bands are attributable to hydrogen bonded groups which may include adsorbed $D_2O$ and HDO molecules, and deuterated CO–D groups.

Both spectra in Figure 4.21b represent two intermediary stages during the drying process. Looking at the O–H stretching region it can be seen that one spectrum (blue line) is more similar to the spectrum recorded in $D_2O$ while the other (red line) resembles more the spectrum recorded in air (cf. Figure 4.20). Differences between the two spectra are most clearly observed for the bands around 2600 cm$^{-1}$, 3451 cm$^{-1}$ and 3548 cm$^{-1}$. In order to extract kinetic information on the dynamic processes during the penetration of liquids into the spruce fibers and the drying of the fibers more studies are required.

The observed bands in the C–H stretching region of the spruce spectra (see Figure 4.21b) are also listed in Table 4.3. A parallel band at 2965 cm$^{-1}$ and three perpendicular bands at 2874 $cm^{-1}$, 2895 $cm^{-1}$ and 2943 $cm^{-1}$ are identified. In all experiments these bands appear to be unaffected by the various ambient conditions. This indicates that they stem mainly from groups of crystalline origin. These bands are further evidence of the structural anisotropy and directional arrangement in the spruce fiber walls.

The results on single spruce fibers demonstrate the applicability of the PM method to investigate fiber materials and (bio)polymeric multicomponent and multiphase systems in liquids. The cuvette made possible the use of liquids as a source of perturbation and as a structural probe. This enabled one to follow *in situ* molecular changes due to wetting and swelling in $D_2O$ and dimethylacetamide. The measurements provided information on hydrogen bonding, orientation and accessibility of structural units of the wood polymers in their native setting in the spruce cell walls. Insights into structural details on different levels could be obtained including orientation of submolecular groups, observation of different crystalline allomorphs, and distinction between highly ordered cellulose domains and less ordered domains.

## 4.3 Towards Polarized Measurements on Single Living Cells

### 4.3.1 Live Cell Adhesion Study with Attenuated Total Reflection Infrared Spectroscopy

The ability of cells to sense, integrate, and respond to environmental cues implies the dynamic interactions among their complex macromolecular components.[184] The explicit study of cell structure and function therefore ultimately requires living cells. *In vitro* experiments are most commonly based on biochemical assays and optical light microscopic methods. However, spectroscopic techniques can provide complementary or additional information. Infrared spectroscopy is a non-invasive, non-destructive, non-cytotoxic as well as a label- and stain-free method and it is very well suited for the study of living cells.[31,32,55] It offers the possibility of time-resolved *in situ* monitoring of biochemical or physical cellular changes which may be triggered by internal or external events.

In this work, the application of infrared spectroscopy was aimed at gaining insights into the complex arrangement and dynamics of the cytoskeleton. Specifically, it was proposed to use polarized infrared spectroscopy to characterize the degree of cytoskeletal order or alignment in a time-resolved fashion. For this purpose, it is desirable to be able to locate macromolecules in single cells and to spectroscopically monitor them at the molecular level. However, this microspectroscopic approach is technologically challenging as it requires instrumental and also methodical developments.

To this end, preliminary studies were performed using attenuated total reflection (ATR) infrared spectroscopy on cell ensembles.[185] These experiments were carried out in order to establish a suitable model system for the *in situ* monitoring by infrared spectroscopy of the cytoskeletal response triggered by an external stimulus. Application of the ATR geometry gives enhanced surface sensitivity and decouples the path length, i.e. the thickness of the sample penetrated by the evanescent field, from the actual extent of aqueous medium during observation. The latter provides ease of sampling in view of the high infrared absorptivity of water. In contrast to relevant optical microscopy techniques (e.g. phase contrast, interference reflection, and total internal reflection fluorescence) ATR infrared spectroscopy thus has the combined virtues of being surface-sensitive and label-free, and of providing molecular-level spectral information. It was previously applied to investigations of bacteria,[186] and to living mammalian cells in studies with regard to cell growth and inhibition[33] as well as infection and activation.[187] As was alluded to in the literature,[33] ATR infrared spectroscopy seems to be suitable also for studies of cell adhesion due to its distinctive nature as a surface probe. In the present work, this potential was addressed and the applicability of ATR infrared spectroscopy for live cell adhesion assays was explored.

Fish fibroblast cells RTG-P1 from rainbow trout were obtained from ATCC (Manassas, VA, USA) and cultured according to the following protocol. The cells were grown in 10 cm petri dishes with Leibovitz L-15 medium (Gibco, Carlsbad, CA, USA), supplemented with 10% fetal bovine serum (Cambrex, Walkersville, MD, USA) and 1% Pen/Strep (Gibco). Cells were incubated in the dark at 23°C in 100% air atmosphere. Cells were used for experiments from P4 to P8. For the ATR infrared experiments, a Bruker VERTEX 70 Fourier-transform infrared spectrometer equipped with a PIKE MIRacle ATR sampling accessory with a 45° single reflection diamond/ZnSe horizontal crystal plate was used. A 100 µL aliquot of a cell suspension of $10^6$ cells/mL in complete medium was pipetted on the uncoated diamond internal reflection element (diameter = 1.8 mm) and covered to prevent evaporation. Mid-infrared spectra with a spectral resolution of 4 $cm^{-1}$ were recorded at room temperature using the globar source, a KBr beamsplitter, a $LN_2$-cooled MCT detector and coadding 256 scans each. As a reference, a single beam spectrum of the bare diamond in air was collected before each experiment. Atmospheric and ATR penetration depth compensations as well as a base line offset with respect to 1800 $cm^{-1}$ were applied. For each experiment, collection of spectra was repeated with duplicate samples to ensure reproducible results.

Figure 4.22a shows the spectra in the range between 1800 cm$^{-1}$ and 900 cm$^{-1}$ for a cell suspension placed on the diamond ATR crystal recorded at time intervals between 0 and 240 min. The ATR absorbance spectrum corresponding to 0 min is characterized by a strong absorption band around 1640 cm$^{-1}$ which is assigned to the bending mode of liquid water.[134] In addition to this band, the successive spectra display several other spectral features that increase in intensity with time until a steady plateau is reached after about 240 min. These absorption bands can be seen more clearly in the difference spectra (see Figure 4.22b) calculated with respect to the spectrum at 0 min. The bands are attributable to the biochemical and structural profile of the cells and can be assigned according to the literature (see Table 4.4).[188,189] It should be noted that due to the limited penetration depth, the infrared radiation interrogates only those cellular fractions which are in close proximity (within an average infrared penetration depth of about 1.2 µm) to the surface. The spectra thus reflect the settling and the spreading of the cells on the diamond surface. Maximum coverage or confluence after 240 min is inferred considering the plateau reached. This conclusion was corroborated by visual inspection of the cells on diamond using a low-resolution microscopic external reflection geometry. The persistence of the infrared bands of cellular origin after exchange of culture medium and after rinsing with a phosphate buffered saline (PBS, Cambrex, Walkersville, MD, USA) solution (100% and 98% retention of integrated cell signal intensity respectively, spectra not shown) indicated good cellular adhesion on diamond which is known to be a biocompatible material for living cells.[190] As a control, cell spreading and adhesion were found to be compromised when the diamond was coated with heat-denatured bovine serum albumin (Sigma, St. Louis, MO, USA) (67% of integrated cell signal intensity with respect to cells on uncoated diamond, dropping to 51% after rinsing with PBS, spectra not shown).

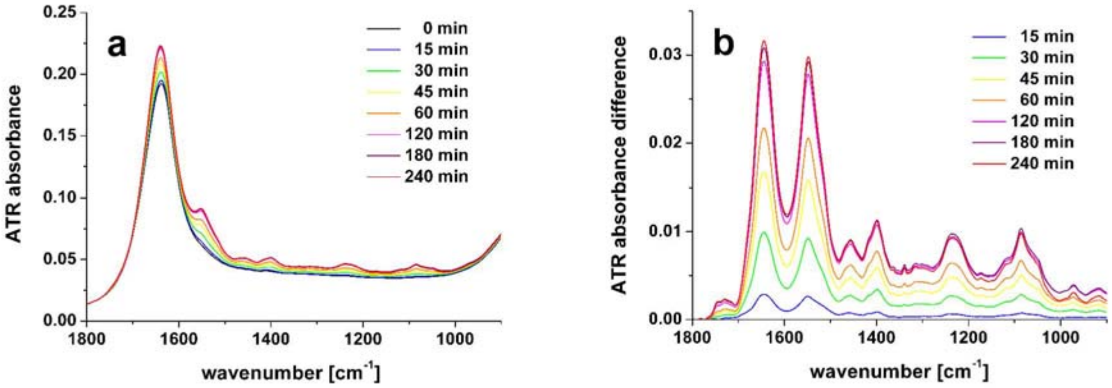

**Figure 4.22.** a) ATR absorbance spectra of a cell suspension placed on diamond in the time course between 0 min and 240 min. b) Difference spectra calculated with respect to the ATR absorbance spectrum at 0 min.

**Table 4.4.** Assignments of bands according to the literature.[188,189]

| Band position [cm$^{-1}$] | Assignment[a] |
|---|---|
| 1745 | C=O str of esters |
| 1729 | (COOH) str |
| 1644 | Amide I of proteins |
| 1547 | Amide II of proteins |
| 1515 | “tyrosine” band |
| 1469 and 1456 | C–H def of CH$_2$ and CH$_3$ |
| 1398 | C=O str (sym) of COO$^-$ |
| 1310-1240 | Amide III of proteins |
| 1235 | P=O str (asym) of PO$_2^-$ phosphodiesters |
| 1200-900 | C–O, C–C str, C–O–H, C–O–C def of carbohydrates |
| 1173 | C–O str |
| 1086 | P=O str (sym) of PO$_2^-$ |
| 972 | P–OH str |

[a] str = stretching; def = deformation; sym = symmetric; asym = antisymmetric

For the cell assays the cells were cultured on diamond for 20 h prior to experiments with an exchange of medium after 10 h. Figure 4.23a shows the ATR absorbance spectra of cells in PBS to which a trypsin/EDTA solution (2.5 g/L of trypsin and 0.38 g/L of EDTA) (Gibco, Carlsbad, CA, USA) was added at the time point denoted as 0 min. Trypsins belong to the serine endopeptidases and are enzymes that cleave peptide bonds in proteins. They can therefore be used to resuspend adherent cells by breaking extracellular attachments to the surface. As can be seen the infrared bands of cellular origin decrease over time and vanish within 45 min. For clarity, the difference spectra with respect to the spectrum recorded after 45 min are shown in Figure 4.23b. This experiment demonstrates that ATR infrared spectroscopy can be used for *in situ* monitoring of the effect of a stimulus or agent on adherent cells. Also, the observed response to trypsin serves as a further proof for the presence of living adherent cells in the experiments.

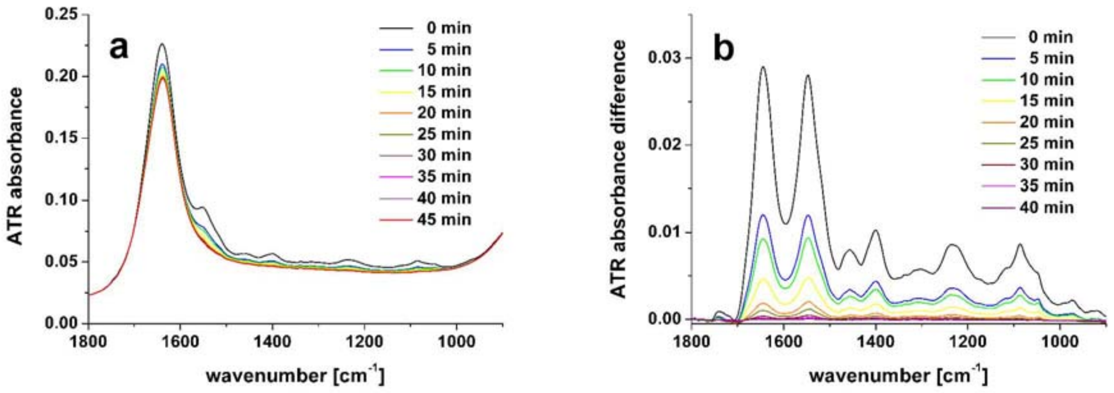

**Figure 4.23.** a) ATR absorbance spectra of cells initially adherent on diamond in the time course between 0 min and 45 min after adding a solution of trypsin/EDTA. b) Difference spectra calculated with respect to the ATR absorbance spectrum at 45 min.

Cytochalasin D is a cell permeable fungal metabolite that causes the inhibition of actin polymerization and the disruption of actin filaments. This disruption of the supramolecular organization of the cytoskeletal actin filaments causes cells to round up.[191] Figure 4.24a shows the ATR absorbance spectra of cells exposed to a 2 μM solution of cytochalasin D (Sigma) from the time point denoted as 0 min. The infrared bands of cellular origin decrease over time. After about 300 min, no significant change in the spectra is detected. The residual integrated signal intensity of the infrared bands of cellular origin after 300 min corresponds to approximately 27% of the initial intensity at 0 min (for reference, see the dotted line in Figure 4.24a which corresponds to the initial spectrum (0 min) shown in Figure 4.22a). This means that the cells do not completely detach from the diamond surface. Looking in a conventional culture dish by light microscopy at cells that were treated with cytochalasin D it was found that the confluent cells changed from a spread or flattened morphology into a spherical shape covering only a fraction of the surface (see Figure 4.25). The difference spectra with respect to the spectrum recorded after 300 min are presented in Figure 4.24b.

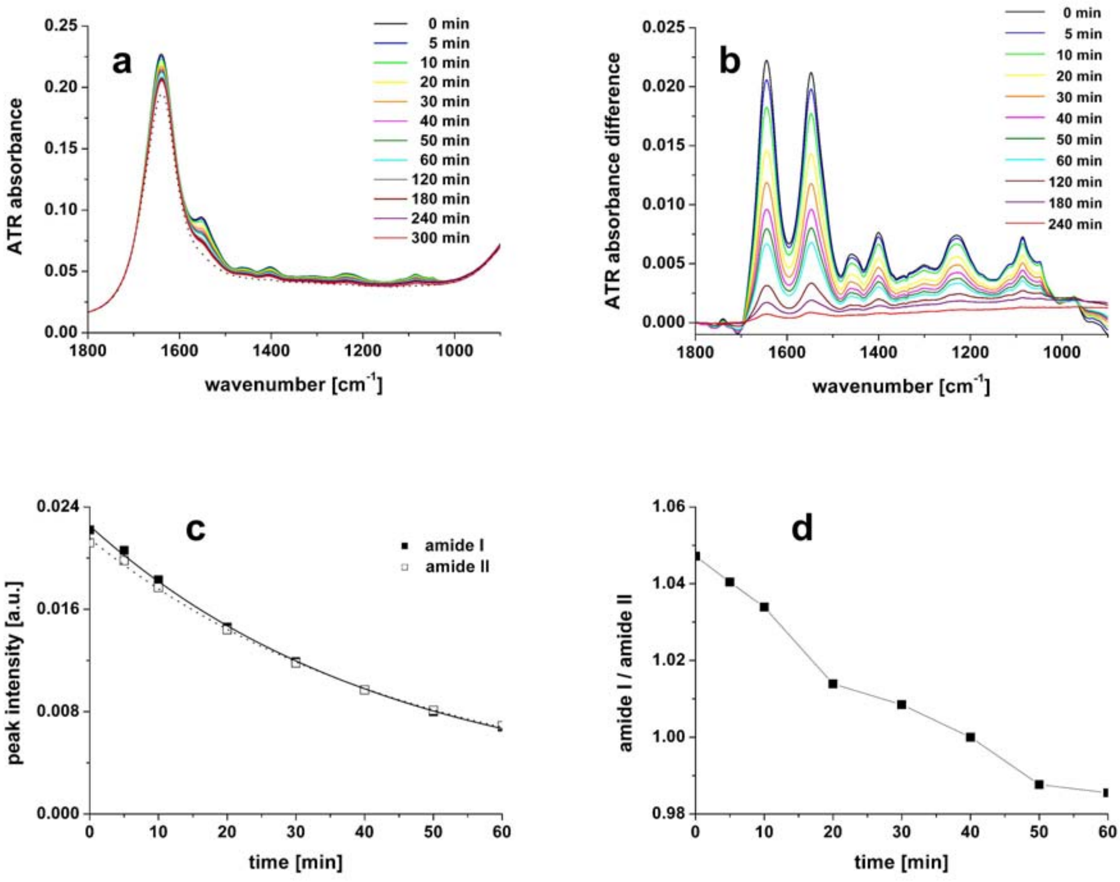

**Figure 4.24.** a) ATR absorbance spectra of cells on diamond after adding a solution of cytochalasin D. For reference, the initial spectrum (0 min) shown in Figure 4.22a is added (see dotted line). b) Difference spectra calculated with respect to the ATR absorbance spectrum at 300 min. The peak maxima (c) and the ratio (d) of the peak maxima of the amide I and amide II bands during the treatment of cells with cytochalasin D.

The projected area seen in the microscope to be covered by cells after 300 min is about 50% (see Figure 4.25). From this it is estimated that only approximately 11% of the actual volume that would be probed in the ATR infrared experiment is filled by cells (assuming perfectly spherical cells with a diameter of 10 µm, and an infrared penetration depth of 1.2 µm). There is a discrepancy between this estimate and the larger (~27%) measured residual infrared cell signal intensity. The most plausible explanation for this is that on diamond the cells after 300 min have a spherical-*like* geometry and actually a larger contact area with the surface than that expected for cells with a perfectly spherical shape.

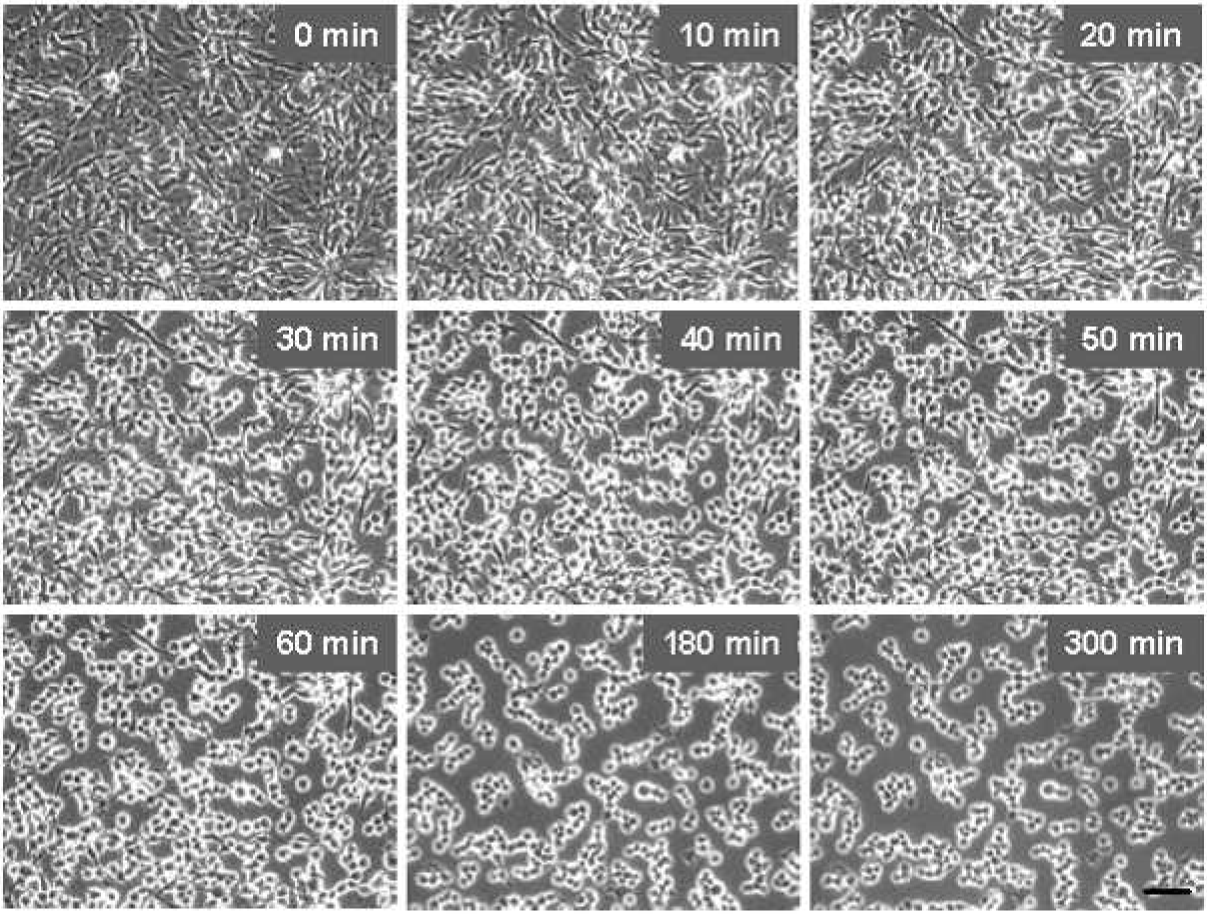

**Figure 4.25.** Light microscopy images of cells in a culture dish that were treated with a 2 µM solution of cytochalasin D. The scale bar in the bottom right-hand corner marks 50 µm.

These experiments with trypsin and cytochalasin D show the capabilities of ATR infrared spectroscopy for live cell assays. The spectra give access to qualitative and quantitative information. For both trypsin and cytochalasin D, the infrared bands of cellular origin were found to decrease with time. This is consistent with a decrease of mass or concentration of the cells and their constituent biochemical molecules in the sample volume probed by the infrared radiation. This is due to the changes of cellular shape and geometry from a spread and more flat morphology when adherent to a more spherical shape towards cellular detachment. Kinetic data can be derived from the time-resolved spectral changes which are associated with the cellular responses. For the fungal toxin cytochalasin D the cell retraction from the surface occurs slower. Cytochalasin D and trypsin act at different sites and in different ways to interrupt cell adhesion and spreading. The difference in the temporal responses is directly related to the mechanistic differences.

Figure 4.26 shows a plot of the integrated intensity for the ATR absorbance spectra acquired during the treatment with cytochalasin D (cf. Figure 4.24a) as a function of time. Assuming a second order exponential decay a good fit ($R^2$ = 0.994) to the experimental data was obtained. A simple lift-off of cells during detachment from the surface would be adequately described by a single exponential term. Cytochalasin D, which was found to induce the retraction of cellular protrusions and the rounding up of cells (cf. Figure 4.25), however causes the more complicated kinetic behaviour observed in Figure 4.26.

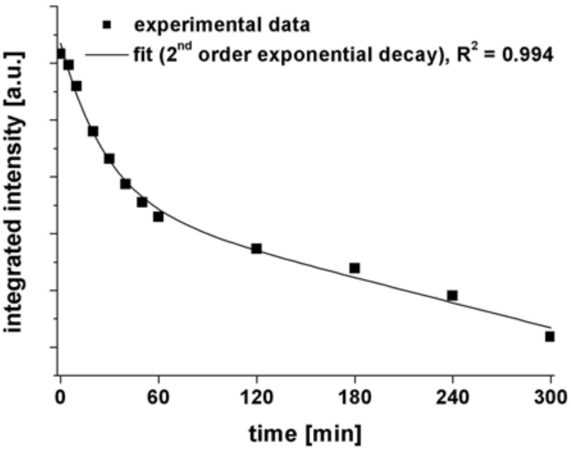

**Figure 4.26.** Integrated intensity for the ATR absorbance spectra acquired during the treatment with cytochalasin D (cf. Figure 4.24a) as a function of time.

The spectra contain specific chemical information on the molecular level. The two most prominent bands in the difference spectra around 1644 $cm^{-1}$ and 1547 $cm^{-1}$ can be assigned to the amide I and amide II absorption modes of proteins. Figure 4.24c shows how the peak maxima for these two bands change during the treatment of cells with cytochalasin D. It is noted that the responses are slightly different. Indeed, the ratio of the peak maxima of the amide I and amide II bands decreases with time (see Figure 4.24d). The interpretation of this observation seems complicated for two reasons. First, the amide I band is superimposed on the bending mode of liquid water, and during the experiments there is a varying exposure of the ATR crystal to aqueous medium. Second, there is a complex and heterogeneous distribution of proteins in the cells. It was however reported that the amide I/II intensity ratios of adsorbed protein films on a Ge ATR crystal were significantly different from those of proteins in solution, suggesting that the difference was associated with changes in the secondary structure.[192] Hence, the amide I/II intensity ratio may be useful to detect changes in the secondary structure of proteins that occur upon adsorption to or desorption from a solid surface. Most recently, a change of the amide I/II intensity ratio was observed upon adhesion of bacteria to an $\alpha$-$Fe_2O_3$-coated ZnSe ATR crystal.[189] Therefore, the change of the amide I/II intensity ratio during the treatment of cells with cytochalasin D may implicate changes in protein conformation. Further experiments are required to get detailed insights into the possible origins (e.g. cell surface proteins) of the variation in the ratio of the amide I and amide II peaks. Further spectral changes, most notably those indicative of cell death,[51,52] were not detected in the measurements.

These results demonstrate that infrared spectroscopy is suitable to monitor *in situ* the biochemically induced structural responses of adherent cells which were exposed to the fungal toxin cytochalasin D. It seems desirable to extend these cell adhesion studies to mammalian cells. Indeed, it is possible to investigate such cells by ATR infrared spectroscopy under the required physiological conditions by controlling *p*H and temperature.[33] It should be noted that concomitant visible images of the cells could not be recorded during these infrared measurements. Another drawback is the lack of spatial resolution in the measurements. Indeed, average spectra from cell ensembles do not provide the same level of information which is available from the analysis of spectra of a large number of single cells.[193]

### 4.3.2 Towards Measurements of Single Living Cells by Infrared Spectroscopy

In collaboration with the Abteilung Biomaterialien of the Max-Planck-Institut für Kolloid- und Grenzflächenforschung, living adherent cells of the murine osteoblastic MC3T3-E1 cell line were studied using infrared microspectroscopy with a thermal globar source and the custom-built microfluidic cuvette. This microspectroscopic approach provides spatial resolution in the infrared measurements with concomitant observation of the cells with visible light. However, the spatial resolution is limited by the thermal source. In this work, the aperture size was 50 x 50 $\mu m^2$ thus approaching the single cell level (cf. Figure 4.27). Cells were seeded on a $CaF_2$ substrate and were cultured in $\alpha$-modified Eagle's minimal essential medium containing 10% fetal calf serum and were maintained in 5% $CO_2$ at 37°C for

48 hours prior to the transfer into the microfluidic device. In the cuvette, the cells were provided with the bicarbonate-$CO_2$-buffered medium by a syringe infusion pump delivered through gas-tight tubing at a flow rate of 25 µL/h. The temperature was maintained at 37°C using the integrated heating elements and temperature control. Cell viability with normal cell behaviour in the microfluidic environment was observed for culturing times in excess of 48 hours. This means that the microfluidic cuvette with its peripheral elements is a reasonably stable device for cell culturing and can be used as a miniincubator.

The microspectroscopic measurements were performed in transmission at a spectral resolution of 4 $cm^{-1}$ with a Bruker Hyperion infrared microscope coupled to a VERTEX 70 Fourier-transform infrared spectrometer using an MCT detector and a globar source and coadding 256 scans per measurement. Figure 4.27a shows an optical micrograph of cells in the cuvette as well as mid-infrared spectra of cells taken at different measurement spots. In the visible image the adherent cells exhibit spread morphologies. Occasionally, cells undergoing mitosis could be observed. These are clear indications of cell viability and normal cell behaviour. The bands in the infrared spectra can be attributed to the biochemical and structural profile of the cells and they are in good agreement with the literature (see Table 4.4).[188,189] These results demonstrate that the cuvette is well suited to measure infrared spectra of living cells in transmission with concomitant observation of the cells.

Subsequent to the studies with ATR infrared spectroscopy on the effect of cytochalasin D on cell ensembles (cf. Chapter 4.3.1), microspectroscopic measurements were performed after the addition of a 2 µM solution of cytochalasin D to the adherent cells in the cuvette. The optical micrograph in Figure 4.27b shows different cell morphologies with respect to untreated cells (cf. Figure 4.27a). The cells appear more rounded up and cellular protrusions are retracted. This change in morphology results from the disruption of actin filaments by cytochalasin D. Infrared spectra of cells treated with cytochalasin D were recorded at different measurement spots (see Figure 4.27b). These results show the potential of infrared microspectroscopy and of the custom-built microfluidic cuvette for monitoring *in situ* the cytoskeletal response triggered by an external stimulus.

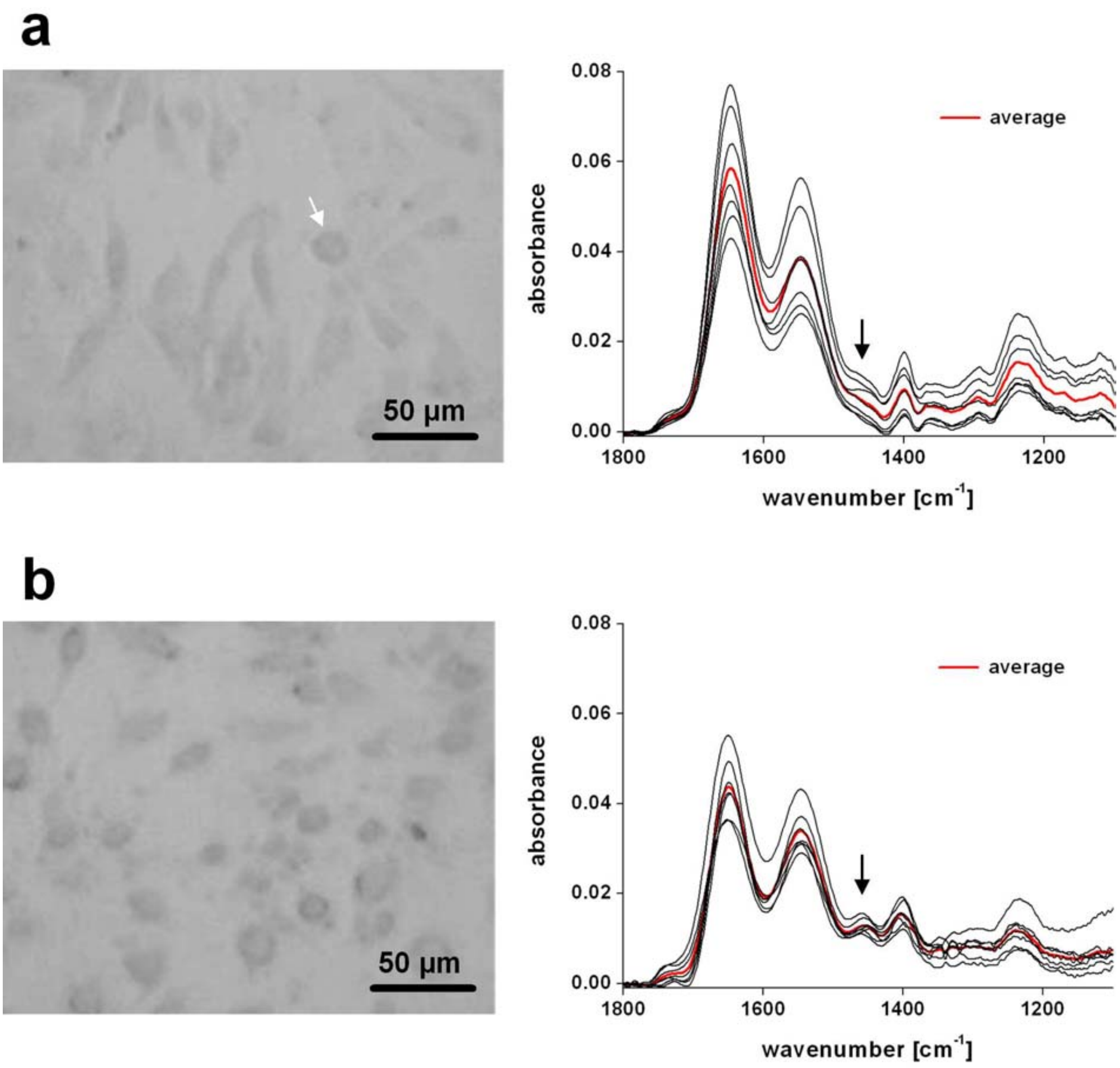

**Figure 4.27.** a) Optical micrograph of murine osteoblastic cells in the custom-built microfluidic cuvette (left). The white arrow indicates a cell undergoing mitosis. Mid-infrared spectra of cells taken at different measurement spots (single measurements are shown as black lines and the average spectrum as a red line) with an aperture size of 50 x 50 $\mu m^2$ (right). b) Optical micrograph of cells treated with cytochalasin D (left) and infrared spectra of treated cells at different measurement spots (right). The black arrows in the spectra highlight the band around 1455 $cm^{-1}$.

However, there are some limitations in the measurements that are reflected in the infrared spectra and that need to be addressed. Both the spectra of untreated cells and cells treated with cytochalasin D show a large variability. It is known that the spectra of cells exhibit a large heterogeneity, even for cultured, i.e. clonal, cells at a similar stage of development.[193] The aperture size of 50 x 50 $\mu m^2$ is insufficient to spatially select a single cell, but rather the spectrum of two or three cells is measured. Also, every measurement spot includes cell nuclei. In fact, the spectra of cells are dominated by the contributions of nuclei.

Therefore, a higher spatial resolution is necessary to be able to clearly discriminate single cells and to focus on cytoplasmic regions of interest and to exclude cell nuclei. Moreover, the spectral shapes for untreated and treated cells (cf. average spectra in Figures 4.27a and b) result from the superposition of the contributions from all cellular components and are thus very similar. The average spectrum of cells treated with cytochalasin D overall has a smaller absorbance. Possibly, there is a spectral difference for the band around 1455 cm$^{-1}$ which is due to the antisymmetric deformation of $CH_3$ and $CH_2$ groups. The significance and interpretation of these differences is not at all clear. In the context of the cytoskeletal arrangement and dynamics, the use of polarized radiation may considerably improve the spectral analysis. Infrared linear dichroism measurements are sensitive to the anisotropic contributions of absorption and, essentially, discard the isotropic background information. Difference spectra calculated from polarized spectra recorded at different time points may thus give more distinct insights into the evolution or change of orientation, order, and anisotropy.

### 4.3.3 Polarized Measurements on Single Cells with Infrared Synchrotron Radiation

Therefore, the application of synchrotron radiation and of the PM setup for measurements on single cells was pursued. Unpolarized mid-infrared spectra of living osteoblastic MC3T3-E1 cells in the microfluidic cuvette were acquired in transmission using 32× Cassegrain objectives and collecting 256 scans per measurement. Figure 4.28 shows the spectrum of a single living cell measured with an aperture size of 15 x 15 µm$^2$ using infrared synchrotron radiation. This spectrum exhibits a reasonably good S/N above 1200 cm$^{-1}$, especially in the protein amide I region around 1644 cm$^{-1}$. It thus becomes possible to clearly discriminate single cells and to focus on regions of interest within a cell.

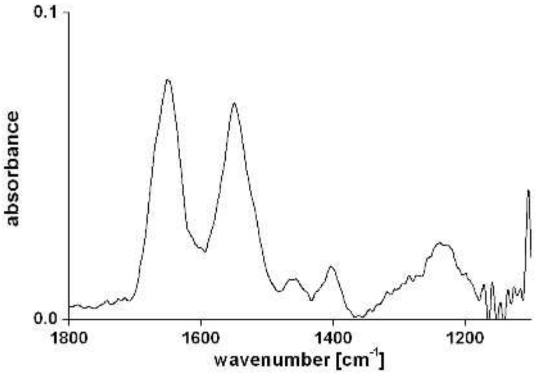

**Figure 4.28.** Spectrum of a single living osteoblastic cell measured with an aperture size of 15 x 15 µm$^2$ using infrared synchrotron radiation.

Infrared absorption of single cells, and in particular in cytoplasmic regions, is comparatively small. Therefore, dried specimens were measured in order to test the feasibility of collecting dichroic spectra of single cells. In this approach cellular dynamics can be neglected and the presence of aqueous medium, which would deteriorate S/N in the amide I region due to water absorption, is avoided. Critical-point-dried MC3T3-E1 cells on $CaF_2$ were measured using the PM setup with infrared synchrotron radiation. Figure 4.29 shows optical micrographs of two dried cells which exhibit cellular regions containing fiber-like structures. These skeletal structures are oriented nearly orthogonal to each other. PM dichroic spectra of these cellular regions were recorded using an aperture size of 15 x 50 $\mu m^2$. As a control, an empty $CaF_2$ background was measured. A base line offset with respect to 1715 $cm^{-1}$ was applied to these three PM dichroic spectra seen in Figure 4.29. Dichroic signals are observed in the protein amide I region around 1644 $cm^{-1}$ for the two cell spectra. Their presence is indicative of a preferential orientation of the protein structures. The two dichroic signals are of opposite sign indicating mutually perpendicular infrared linear dichroism. This seems to agree well with the orientation of the observed skeletal structures. Therefore, such spectral signatures may be used to study cytoskeletal orientation and arrangements. These results demonstrate that, in principle, the PM measurements can give information on infrared linear dichroism even in single cells.

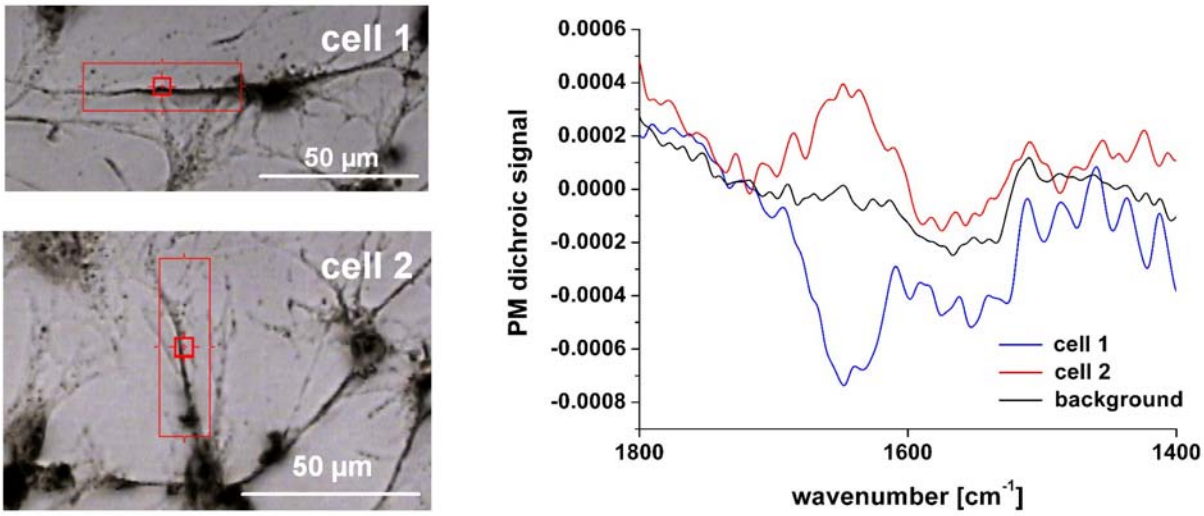

**Figure 4.29.** Optical micrographs (left) and PM dichroic spectra (right) of dried MC3T3-E1 cells on $CaF_2$. The polarized infrared measurements were performed using synchrotron radiation and an aperture size of 15 x 50 $\mu m^2$ in the areas indicated by the outer red rectangles in the images. As a control, an empty $CaF_2$ background was measured. Mutually perpendicular infrared linear dichroism is observed for the two cell spectra in the protein amide I region around 1644 $cm^{-1}$.

It should be noted that the dichroic bands are very small. In fact, 4096 scans were collected in order to obtain spectra with an acceptable S/N in these polarized measurements. For each spectrum, this corresponds to a measurement time which is in excess of 30 min. The measurement time is expected to increase for comparable studies performed in aqueous medium in the microfluidic cuvette. Clearly, this temporal resolution is insufficient to investigate dynamic phenomena such as cytoskeletal rearrangements in a living system.[19,23] This means that Fourier-transform infrared microspectroscopy, even with the use of synchrotron radiation and the PM method, is inadequate for polarized measurements of single living cells. This presents a severe instrumental limitation. Therefore, in this work, polarized measurements on single living cells did not succeed. For such measurements improvements in temporal resolution and sensitivity of approximately two orders of magnitude are necessary. Importantly, novel instrumental developments based on dispersive spectrometers using focal plane array detectors (see Chapter 5) may well meet these requirements, thus making feasible polarized measurements of single living cells.

# 5 Discussion

Infrared spectroscopy is a non-destructive probe and a powerful technique to characterize *in situ* multiphase and multicomponent macromolecular systems. The investigations of multiphase matrices in iPP-LCP model composites and the multicomponent and multiphase wood fibers took advantage of these capabilities. The spectral information is related to submolecular functional groups and molecular-level information can be derived using the molecular vibrations as intrinsic markers.

In the investigations of composite materials spatial resolution is important to be able to discriminate different areas of interest. Compared to optical microscopies such as fluorescence confocal microscopy,[194] infrared microspectroscopy suffers from poor lateral spatial resolution. In a laboratory setup, the actual limit is not dictated by the wavelength of the light but by the brilliance of the thermal source. Diffraction-limited spatial resolution is obtained by using infrared synchrotron radiation.[38] Using infrared synchrotron radiation, the spatial resolution in the presented microspectroscopic experiments was however well matched to the lateral dimensions of single wood fibers and the cytoplasmic areas of interest in single cells, and well suited to map or image heterogeneities in transition metal oxides and the iPP composites. Regardless of the spatial resolution, the spectral information in the probed areas gives also access to lower hierarchical levels down to the molecular scale.

Strong absorption of mid-infrared radiation by water is another limitation in infrared spectroscopy. In this work, the implementation of a microfluidic device was presented. The device was shown to be suitable for the infrared *in situ* measurement of living cells in aqueous medium with concomitant visible observation. Moreover, it was used for the study of the wooden cell wall in the presence of $D_2O$ and dimethylacetamide. The microfluidic cuvette is a versatile device which may be used as a miniincubator and also as a reaction and measurement chamber. Cell culturing times in excess of 48 hours were achieved providing a firm basis to expand on the measurements on single living cells. Further applications of the cuvette are possible in, for example, studies of single wood fibers or other kinds of plant cell walls or cellulose-based composites using temperature variation, enzymatic degradation and chemical modification as external perturbations. Thus, the effects of, for example, drugs or hormones on cells, and of enzymatic or chemical treatments on biological materials may be observed *in situ* by infrared spectroscopy.

Structural anisotropy may be a key material characteristic resulting in anisotropic material properties and optimized function. An additional level of information in the infrared measurements is obtained by using polarized light because, besides the composition and structure, molecular orientation and hence anisotropy can be interrogated. In this work, a polarization modulation apparatus was implemented for the study of small and heterogeneous anisotropic samples. This implementation produced the novel combination of synchrotron-based infrared microspectroscopy with polarization modulation. The instrumental performance was evaluated and the capabilities were demonstrated on different materials systems. Analysis of the spectrally as well as spatially resolved infrared linear dichroism provided new insights into synthetic and biological polymer composites. A further development of the presented method can be the combination with micromechanical examinations.[8] Recently, molecular changes during tensile deformation of single wood fibers were investigated by Raman microscopy.[195] Polarized infrared microspectroscopy may also be applicable because it can be used as a complementary structural analysis tool. To this end, in collaboration with the Abteilung Biomaterialien of the Max-Planck-Institut für Kolloid- und Grenzflächenforschung, preliminary experiments on single wood fibers have been initiated which combine PM dichroic measurements with micromechanical testing (data not shown).

A comprehensive qualitative and quantitative understanding of the structure and composition in complex materials and systems requires the application of several methods for their characterization. It therefore seems to be desirable to use infrared microspectroscopy for materials characterization in a complementary fashion with other techniques in order to derive more extensive information. For example, the hyphenation of fluorescence imaging with synchrotron-based infrared microspectroscoy was reported.[46] An integrated approach to apply different techniques to a single sample is very attractive. It seems feasible in particular at synchrotron radiation sources because of the availability and coexistence of many varied and sophisticated experimental stations and techniques in a single facility. A combination of infrared microspectroscopy with X-ray microspectroscopy and microfocus X-ray diffraction using synchrotron radiation may be pursued.[42,45] However, unified sampling and transfer systems are necessary.

In this work, instrumental and methodical developments were pursued to make possible polarized measurements on single living cells. It was proposed to use polarized infrared spectroscopy to characterize the degree of cytoskeletal order or alignment in a time-resolved fashion. Preliminary experiments were performed on cell ensembles using ATR infrared spectroscopy and on the single cell level using synchrotron-based infrared microspectroscopy and the microfluidic cuvette. It was also demonstrated that polarized measurements with the PM method could resolve the infrared linear dichroism, and hence preferential orientation, of protein structures in single dried cells.

However, it was found that Fourier-transform infrared microspectroscopy is inadequate for polarized measurements of single living cells. The temporal resolution in the measurements attaining the required sensitivity is insufficient. This presents a severe instrumental limitation, and improvements of approximately two orders of magnitude are necessary. Novel instrumental developments may hold the key to overcome this obstacle. Recently, dispersive spectrometers using focal plane array detectors have been implemented.[81-86] Instead of single element detectors, array detectors have multiple detector elements or pixels. In these spectrometers, the exit slit required in classical dispersive spectrometers is absent and a diffraction grating or prism disperses the infrared light along the rows of the array detector. A pixel row in the spectral image corresponds to a single beam spectrum, i.e. intensity as a function of pixel number or wavenumber. Multiple spectral elements are thus collected simultaneously. This means that a multichannel advantage comparable to the Fellgett or multiplex advantage of an interferometer used in Fourier-transform infrared spectroscopy is achieved. The S/N depends on the number of accumulated photons. The integration time needed to acquire a spectrum is significantly shorter than the measurement time for a Fourier-transform infrared spectrum with the same S/N.[196] A temporal resolution of below 100 μs was demonstrated.[85] The second dimension of a focal plane array detector, i.e. the columns, may be exploited in various ways. Several rows can be used for averaging, the so-called pixel binning, in order to increase the S/N of the spectra. This gives a distinct noise level advantage over Fourier-transform infrared spectroscopy. Moreover, two separate and independent spectral images may be detected simultaneously on different areas of the array. A real-time background correction[86] or the simultaneous recording of two mutually orthogonal polarized absorption spectra[83] can be realized by an appropriate arrangement of the optical setup. This possibility of dual channel or even multiple beam experiments makes possible fast and sensitive measurements because instrumental drifts and atmospheric changes during the measurement can be neglected. In contrast to Fourier-transform infrared spectrometers, there are no moving parts in these novel dispersive spectrometers making the instruments robust with regard to mechanical vibrations and temperature instabilities. Very recently, the coupling of an infrared microscope to a dispersive infrared spectrometer with an array detector was demonstrated.[197] The combination of this novel microspectroscopic scheme with infrared synchrotron radiation seems to be a promising further development. A dispersive spectrometer requires an entrance slit. Unlike thermal sources, the throughput of brilliant infrared synchrotron radiation is unaffected by this slit. Thus, the Jacquinot or throughput advantage of Fourier-transform infrared spectroscopy is essentially cancelled. Also, the use of synchrotron radiation will be beneficial for investigations requiring diffraction-limited spatial resolution. Currently, the feasibility of setting up a synchrotron-based infrared microscope using a dispersive infrared spectrometer with an array detector is explored with BESSY. It is anticipated that this instrument will provide significantly enhanced sensitivity and acquisition times and thus make feasible polarized measurements of single living cells.

# 6 Conclusions

In this work, the novel combination of synchrotron-based Fourier-transform infrared microspectroscopy with polarization modulation was implemented. This instrumental development produced a unique microprobe which was designed for the non-destructive *in situ* study of small or heterogeneous anisotropic samples. The performance of the instrument was tested on isotactic polypropylene, transition metal oxides and liquid crystals, thereby evaluating the capabilities of the method. A key feature demonstrated is the ability to spatially resolve infrared linear dichroism down to the diffraction limit by using infrared synchrotron radiation. Another characteristic of great potential is the capability to obtain orientation information in reference-free measurements. The capabilities of the method were further explored and exploited in studies of fiber-reinforced polypropylene model composites and single wood fibers. The reference-free and near-diffraction-limited mapping of infrared linear dichroism in the polypropylene composites was demonstrated. The results on single wood fibers illustrated the capability of the method to investigate *in situ* (bio)polymeric multicomponent and multiphase systems. It was thus shown that the method can provide new insights into synthetic and biological polymer composites. This method is more widely applicable to investigations of complex synthetic and biological materials. Possible further developments include the combination with micromechanical examinations.

A microfluidic infrared transmission cuvette for measurements of complex biological systems in aqueous environments and other liquids was implemented. Specifically, this cuvette was designed and shown to be suitable for the *in situ* measurement of living cells by infrared microspectroscopy with concomitant visible observation. The cuvette was also used for the study of the wooden cell wall in the presence of $D_2O$ and dimethylacetamide. The microfluidic cuvette was thus shown to be a versatile device which may be used as a miniincubator and also as a reaction and infrared measurement chamber with varied possible further applications.

Studies of living cells were performed using attenuated total reflection infrared spectroscopy on cell ensembles, as well as infrared microspectrosocpy in order to approach the single cell level. In particular, using the fungal toxin cytochalasin D, a model system was established for the *in situ* monitoring by infrared spectroscopy of the cytoskeletal response triggered by an external stimulus. Importantly, it was found that Fourier-transform infrared microspectroscopy is inadequate for polarized measurements of single living cells thus precluding single live cell studies of the cytokskeletal arrangement and dynamics. However, a novel microspectroscopic approach based on a dispersive spectrometer using a focal plane array detector is anticipated to make feasible polarized measurements of single living cells.

# References

1. M. C. Flemings, *Ann. Rev. Mater. Sci.*, **1999**, 29, 1-23.

2. B. Bensaude-Vincent, A. Hessenbruch, *Nat. Mat.*, **2004**, 3, 345-347.

3. W. D. Callister, *Materials Science and Engineering - An Introduction*, Wiley, New York, **2000**.

4. P. Fratzl, *Curr. Opin. Colloid Interface Sci.*, **2003**, 8, 32-39.

5. P. Fratzl, *Physik J.*, **2002**, 1(5), 49-55.

6. J. D. Currey, *Science*, **2005**, 309, 253-254.

7. J. Aizenberg, J. C. Weaver, M. S. Thanawala, V. C. Sundar, D. E. Morse, P. Fratzl, *Science*, **2005**, 309, 275-278.

8. I. Burgert, *Am. J. Bot.*, **2006**, 93, 1391-1401.

9. M. A. Meyers, A. Y. M. Lin, Y. Seki, P.-Y. Chen, B. K. Kad, S. Bodde, *JOM*, **2006**, 58, 35-41.

10. A. S. Deshpande, I. Burgert, O. Paris, *Small*, **2006**, 2, 994-998.

11. A. H. Heuer, D. J. Fink, V. J. Laraia, J. L. Arias, P. D. Calvert, K. Kendall, G. L. Messing, J. Blackwell, P. C. Rieke, D. H. Thompson, A. P. Wheeler, A. Veis, A. I. Caplan, *Science*, **1992**, 255, 1098-1105.

12. R. W. Cahn, *Nature*, **1996**, 382, 684.

13. B. L. Smith, T. E. Schäffer, M. Viani, J. B. Thompson, N. A. Frederick, J. Kindt, A. Belcher, G. D. Stucky, D. E. Morse, P. K. Hansma, *Nature*, **1999**, 399, 761-763.

14. P. Fratzl, I. Burgert, H. S. Gupta, *Phys. Chem. Chem. Phys.*, **2004**, 6, 5575-5579.

15. E. Sackmann, *Physik J.*, **2004**, 3(2), 35-42.

16. B. D. Matthews, D. R. Overby, F. J. Alenghat, J. Karavitis, Y. Numaguchi, P. G. Allen, D. E. Ingber, *Biochem. Biophys. Res. Comm.*, **2004**, 313, 758-764.

17. N. Q. Balaban, U. S. Schwarz, D. Riveline, P. Goichberg, G. Tzur, I. Sabanay, D. Mahala, S. Safran, A. Bershadsky, L. Addadi, B. Geiger, *Nat. Cell Biol.*, **2001**, 3, 466-473.

18. A. R. Bausch, F. Ziemann, A. A. Boulbitch, K. Jacobson, E. Sackmann, *Biophys. J.*, **1998**, 75, 2038-2049.

19. B. Geiger, A. Bershadsky, R. Pankov, K. M. Yamada, *Nat. Rev. Mol. Cell Biol.*, **2001**, 2, 793-805.

20. J. A. Theriot, T. J. Mitchison, *Nature*, **1991**, 352, 126-131.

21. M. A. Dichtl, E. Sackmann, *Proc. Natl. Acad. Sci. USA*, **2002**, 99, 6533-6538.

22. M. Arnold, E. A. Cavalcanti-Adam, R. Glass, J. Blümmel, W. Eck, M. Kantlehner, H. Kessler, J. P. Spatz, *ChemPhysChem*, **2004**, 5, 383-388.

23. K. Hu, L. Ji, K. T. Applegate, G. Danuser, C. M. Waterman-Storer, *Science*, **2007**, 315, 111-115.

24. V. K. Kodali, W. Roos, J. P. Spatz, J. E. Curtis, *Soft Matter*, **2007**, 3, 337-348.

25. W. W. Coblentz, *Investigations of Infra-Red Spectra*, Carnegie Institution, Washington, **1905**.

26. H. W. Siesler, K. Holland-Moritz, *Infrared and Raman Spectroscopy of Polymers*, Marcel Dekker, New York, **1980**.

27. H. W. Siesler, *Adv. Polym. Sci.*, **1984**, 65, 1-77.

28. C. Pellerin, M.-E. Rousseau, M. Côté, M. Pézolet, *Macromol. Symp.*, **2005**, 220, 85-98.

29. T. Buffeteau, M. Pézolet, in *Handbook of Vibrational Spectroscopy*, edited by J. M. Chalmers and P. R. Griffiths, Wiley, Chichester, **2002**, pp. 693-710.

30. M. Manfait, T. Theophanides, *Biochem. Biophys. Res. Comm.*, **1983**, 116, 321-326.

31. D. Naumann, *Infrared Phys.*, **1984**, 24, 233-238.

32. D. G. Cameron, A. Martin, D. J. Moffatt, H. H. Mantsch, *Biochemistry*, **1985**, 24, 4355-4359.

33. T. B. Hutson, M. L. Mitchell, J. T. Keller, D. J. Long, M. J. W. Chang, *Anal. Biochem.*, **1988**, 174, 415-422.

34. D. Naumann, D. Helm, H. Labischinski, *Nature*, **1991**, 351, 81-82.

35. R. Barer, A. R. H. Cole, H. W. Thompson, *Nature*, **1949**, 163, 198-201.

36. R. G. Messerschmidt, M. A. Harthcock, *Infrared Microspectroscopy Theory and Applications*, Marcel Dekker, New York, **1988**.

37. A. J. Sommer, in *Handbook of Vibrational Spectroscopy*, edited by J. M. Chalmers and P. R. Griffiths, Wiley, Chichester, **2002**, pp. 1369-1385.

38. G. L. Carr, J. A. Reffner, G. P. Williams, *Rev. Sci. Instrum.*, **1995**, 66, 1490-1492.

39. G. P. Williams, in *Handbook of Vibrational Spectroscopy*, edited by J. M. Chalmers and P. R. Griffiths, Wiley, Chichester, **2002**, pp. 341-348.

40. P. Dumas, L. Miller, *J. Biol. Phys.*, **2003**, 29, 201-218.

41. L. M. Miller, G. D. Smith, G. L. Carr, *J. Biol. Phys.*, **2003**, 29, 219-230.

42. P. Dumas, M. J. Tobin, *Spectrosc. Europe*, **2003**, 15(6), 17-23.

43. P. Dumas, N. Jamin, J. L. Teillaud, L. M. Miller, B. Beccard, *Faraday Discuss.*, **2004**, 126, 289-302.

44. G. Ellis, C. Marco, M. Gómez, *Infrared Phys. Technol.*, **2004**, 45, 349-364.

45. J. Torre, M. Cortázar, M. Gómez, C. Marco, G. Ellis, C. Riekel, P. Dumas, *Macromolecules*, **2006**, 39, 5564-5568.

46. L. M. Miller, P. Dumas, N. Jamin, J. L. Teillaud, J. Miklossy, L. Forro, *Rev. Sci. Instrum.*, **2002**, 73, 1357-1360.

47. K. M. Dokken, L. C. Davis, N. S. Marinkovic, *Appl. Spectrosc. Rev.*, **2005**, 40, 301-326.

48. L. P. Choo, D. L. Wetzel, W. C. Halliday, M. Jackson, S. M. LeVine, H. H. Mantsch, *Biophys. J.*, **1996**, 71, 1672-1679.

49. M. Diem, M. Romeo, C. Matthäus, M. Miljkovic, L. Miller, P. Lasch, *Infrared Phys. Technol.*, **2004**, 45, 331-338.

50. N. Jamin , P. Dumas , J. Moncuit, W. H. Fridman, J. L. Teillaud, G. L. Carr, G. P. Williams, *Cell Mol. Biol.*, **1998**, 44, 9-13.

51. N. Jamin, P. Dumas, J. Moncuit, W. H. Fridman, J.L. Teillaud, G. L. Carr, G. P. Williams, *Proc. Natl. Acad. Sci. USA*, **1998**, 95, 4837-4840.

52. H. N. Holman, M. C. Martin, E. A. Blakely, K. Bjornstad, W. R. McKinney, *Biopolymers*, **2000**, 57, 329-335.

53. D. A. Moss, M. Keese, R. Pepperkok, *Vib. Spectrosc.*, **2005**, 38, 185-191.

54. H. N. Holman, K. A. Bjornstad, M. P. McNamara, M. C. Martin, W. R. McKinney, E. A. Blakely, *J. Biomed. Opt.*, **2002**, 7, 417-424.

55. H. N. Holman, M. C. Martin, W. R. McKinney, *J. Biol. Phys.*, **2003**, 29, 275-286.

56. L. A. Nafie, M. Diem, *Appl. Spectrosc.*, **1979**, 33, 130-135.

57. C. Marcott, *Appl. Spectrosc.*, **1984**, 38, 442-443.

58. T. Buffeteau, B. Desbat, M. Pézolet, J. M. Turlet, *J. Chim. Phys.*, **1993**, 90, 1467-1489.

59. W. Herschel, *Philos. Trans. R. Soc.*, **1800**, 90, 255-283.

60. W. Herschel, *Philos. Trans. R. Soc.*, **1800**, 90, 284-292.

61. E. S. Barr, *Infrared Phys.*, **1961**, 1, 1-4.

62. B. Schrader, *Infrared and Raman Spectroscopy Methods and Applications*, VCH, Weinheim, **1995**.

63. P. R. Griffiths, J. A. de Haseth, *Fourier Transform Infrared Spectrometry*, Wiley, New York**, 1986**.

64. G. L. Carr, P. Dumas, C. J. Hirschmugl, G. P. Williams, *Il Nuovo Cimento*, **1998**, 20D, 375-395.

65. J. Schwinger, *Phys. Rev.*, **1949**, 75, 1912-1925.

66. G. P. Williams, *Nucl. Instrum. Meth.*, **1982**, 195, 383-387.

67. W. D. Duncan, G. P. Williams, *Appl. Opt.*, **1983**, 22, 2914-2923.

68. G. L. Carr, G. P. Williams, *SPIE*, **1997**, 3153, 51-59.

69. G. L. Carr, *Rev. Sci. Instrum.*, **2001**, 72, 1613-1619.

70. M. C. Martin, N. M. Tsvetkova, J. H. Crowe, W. R. McKinney, *Appl. Spectrosc.*, **2001**, 55, 111-113.

71. M. Gensch, K. Hinrichs, A. Röseler, E. H. Korte, U. Schade, *Anal. Bioanal. Chem.*, **2003**, 376, 626-630.

72. U. Schade, A. Röseler, E. H. Korte, M. Scheer, W. B. Peatman, *Nucl. Instrum. Meth. Phys. Res. A*, **2000**, 455, 476-486.

73. R. P. S. M. Lobo, J. D. LaVeigne, D. H. Reitze, D. B. Tanner, G. L. Carr, *Rev. Sci. Instrum.*, **2002**, 73, 1-10.

74. P. R. Griffiths, in *Handbook of Vibrational Spectroscopy*, edited by J. M. Chalmers and P. R. Griffiths, Wiley, Chichester, **2002**, pp. 33-43.

75. P. Connes, *Infrared Phys.*, **1984**, 24, 69-93.

76. P. B. Fellgett, Thesis, University of Cambridge, **1951**.

77. P. B. Fellgett, *Infrared Phys.*, **1984**, 24, 95-98.

78. P. Jacquinot, *17e congrès du GAMS*, Paris, **1954**, 25.

79. P. Jacquinot, *Infrared Phys.*, **1984**, 24, 99-101.

80. J. W. Cooley, J. W. Tukey, *Math. Comput.*, **1965**, 19, 297-301.

81. D. L. Elmore, M.-W. Tsao, S. Frisk, D. B. Chase, J. F. Rabolt, *Appl. Spectrosc.*, **2002**, 56, 145-149.

82. D. L. Elmore, C. L. Leverette, D. B. Chase, A. T. Kalambur, Y. J. Liu, J. F. Rabolt, *Langmuir*, **2003**, 19, 3519-3524.

83. C. Pellerin, C. M. Snively, D. B. Chase, J. F. Rabolt, *Appl. Spectrosc.*, **2004**, 58, 639-646.

84. C. Pellerin, S. Frisk, J. F. Rabolt, D. B. Chase, *Appl. Spectrosc.*, **2004**, 58, 799-803.

85. C. M. Snively, C. Pellerin, J. F. Rabolt, D. B. Chase, D. B., *Anal. Chem.*, **2004**, 76, 1811-1816.

86. I. Pelletier, C. Pellerin, D. B. Chase, J. F. Rabolt, *Appl. Spectrosc.*, 2005, 59, 156-163.

87. E. Y. Jiang, *Advanced FT-IR Spectroscopy Principles, Experiments and Applications*, Thermo Electron Corporation, Madison, **2003**.

88. L. Mertz*,* *Infrared Phys.*, **1967**, 7, 17-23.

89. L. Mertz, *Infrared Phys.*, **1984**, 24, 111-112.

90. E. N. Lewis, P. J. Treado, R. C. Reeder, G. M. Story, A. E. Dowrey, C. Marcott, I. W. Levin, *Anal. Chem.*, **1995**, 67, 3377-3381.

91. E. N. Lewis, I. W. Levin, *Appl. Spectrosc.*, **1995**, 49, 672-678.

92. A. J. Sommer, J. E. Katon, *Appl. Spectrosc.*, **1991**, 45, 1633-1640.

93. K. Nishikida, *Spatial Resolution in Infrared Microscopy and Imaging*, Thermo Electron Corporation, Madison, **2004**.

94. L. M. Miller, R. J. Smith, *Vib. Spectrosc.*, **2005**, 38, 237-240.

95. R. Ikeda, B. Chase, N. Everall, in *Handbook of Vibrational Spectroscopy*, edited by J. M. Chalmers and P. R. Griffiths, Wiley, Chichester, **2002**, pp. 716-730.

96. V. G. Gregoriou, S. Tzavalas, S. T. Bollas, *Appl. Spectrosc.*, **2004**, 58, 655-661.

97. B. Chase, in *Infrared Microspectroscopy Theory and Applications*, edited by R. G. Messerschmidt and M. A. Harthcock, Marcel Dekker, New York, **1988**, pp. 93-102.

98. A. E. Dowrey, C. Marcott, *Appl. Spectrosc.*, **1982**, 36, 414-416.

99. T. Buffeteau, B. Desbat, J. M. Turlet, *Appl. Spectrosc.*, **1991**, 45, 380-389.

100. B. J. Barner, M. J. Green, E. I. Sáez, R. M. Corn, *Anal. Chem.*, **1991**, 63, 55-60.

101. M. J. Green, B. J. Barner, R. M. Corn, *Rev. Sci. Instrum.*, **1991**, 62, 1426-1430.

102. T. Buffeteau, B. Desbat, D. Blaudez, J. M. Turlet, *Appl. Spectrosc.*, **2000**, 54, 1646-1650.

103. B. L. Frey, R. M. Corn, S. C. Weibel, in *Handbook of Vibrational Spectroscopy*, edited by J. M. Chalmers and P. R. Griffiths, Wiley, Chichester, **2002**, pp. 1042-1056.

104. J. Saccani, T. Buffeteau, B. Desbat, D. Blaudez, *Appl. Spectrosc.*, **2003**, 57, 1260-1265.

105. G. Steiner, V. Sablinskas, M. Kitsche, R. Salzer, *Anal. Chem.*, **2006**, 78, 2487-2493.

106. L. A. Nafie, R. K. Dukor, T. B. Freedman, in *Handbook of Vibrational Spectroscopy*, edited by J. M. Chalmers and P. R. Griffiths, Wiley, Chichester, **2002**, pp. 731-744.

107. D. Berthier, T. Buffeteau, J.-M. Léger, R. Oda, I. Huc, *J. Am. Chem. Soc.*, **2002**, 124, 13486-13494.

108. T. Buffeteau, F. Lagugné-Labarthet, C. Sourisseau, *Appl. Spectrosc.*, **2005**, 59, 732-745.

109. I. Noda, A. E. Dowrey, C. Marcott, *Appl. Spectrosc.*, **1988**, 42, 203-217.

110. V. Abetz, G. G. Fuller, R. Stadler, *Makromol. Chem., Macromol. Symp.*, **1991**, 52, 23-40.

111. T. Buffeteau, B. Desbat, L. Bokobza, *Polymer*, **1995**, 36, 4339-4343.

112. T. Buffeteau, M. Pézolet, *Appl. Spectrosc.*, **1996**, 50, 948-955.

113. M. Pézolet, C. Pellerin, R. E. Prud'homme, T. Buffeteau, *Vib. Spectrosc.*, **1998**, 18, 103-110.

114. H. Wang, D. K. Graff, J. R. Schoonover, R. A. Palmer, *Appl. Spectrosc.*, **1999**, 53, 687-696.

115. C. Pellerin, M.-E. Rousseau, R. E. Prud'homme, M. Pézolet, *Appl. Spectrosc.*, **2002**, 56, 17-23.

116. Y. Wang, C. Pellerin, C. G. Bazuin, M. Pézolet, *Macromolecules*, **2005**, 38, 4377-4383.

117. K. W. Hipps, G. A. Crosby, *J. Phys. Chem.*, **1979**, 83, 555-562.

118. Y. Shigematsu, A. Takada, N. Nemoto, K.-H. Nitta, *Rev. Sci. Instrum.*, **2001**, 72, 3927-3932.

119. Y. Song, K.-H. Nitta, N. Nemoto, *Macromolecules*, **2003**, 36, 1955-1961.

120. M. Kölhed, B. Lendl, B. Karlberg, *Analyst*, **2003**, 128, 2-6.

121. R. Masuch, D. A. Moss, *Appl. Spectrosc.*, **2003**, 57, 1407-1418.

122. N. S. Marinkovic, A. R. Adzic, M. Sullivan, K. Kovacs, L. M. Miller, D. L. Rousseau, S.-R. Yeh, M. R. Chance, *Rev. Sci. Instrum.*, **2000**, 71, 4057-4060.

123. P. Hinsmann, J. Frank, P. Svasek, M. Harasek, B. Lendl, *Lab Chip*, **2001**, 1, 16-21.

124. E. Kauffmann, N. C. Darnton, R. H. Austin, C. Batt, K. Gerwert, *Proc. Natl. Acad. Sci. USA*, **2001**, 98, 6646-6649.

125. M. Kakuta, P. Hinsmann, A. Manz, B. Lendl, *Lab Chip*, **2003**, 3, 82-85.

126. S. Kulka, N. Kaun, J. R. Baena, J. Frank, P. Svasek, D. Moss, M. J. Vellekoop, B. Lendl, *Anal. Bioanal. Chem.*, **2004**, 378, 1735-1740.

127. N. Kaun, S. Kulka, J. Frank, U. Schade, M. J. Vellekoop, M. Harasek, B. Lendl, *Analyst*, **2006**, 131, 489-494.

128. M. Kölhed, P. Hinsmann, P. Svasek, J. Frank, B. Karlberg, B. Lendl, *Anal. Chem.*, **2002**, 74, 3843-3848.

129. T. Pan, R. T. Kelly, M. C. Asplund, A. T. Woolley, *J. Chromatogr. A*, **2004**, 1027, 231-235.

130. J. Yan, K. Syoji, J. Tamaki, *J. Vac. Sci. Technol. B*, **2004**, 22, 46-51.

131. G. Kopitkovas, T. Lippert, C. David, A. Wokaun, J. Gobrecht, *Thin Solid Films*, **2004**, 453-454, 31-35.

132. R. Bennewitz, M. Reichling, E. Matthias, *Surf. Sci.*, **1997**, 387, 69-77.

133. F. Costache, J. Reif, *Thin Solid Films*, **2004**, 453-454, 334-339.

134. Y. Maréchal, *J. Phys. Chem.*, **1993**, 97, 2846-2850.

135. K. Rahmelow, W. Hübner, *Appl. Spectrosc.*, **1997**, 51, 160-170.

136. M. Romeo, M. Diem, *Vib. Spectrosc.*, **2005**, 38, 129-132.

137. W. B. Peatman, U. Schade, *Rev. Sci. Instrum.*, **2001**, 72, 1620-1624.

138. U. Schade, A. Röseler, E. H. Korte, F. Bartl, K. P. Hofmann, T. Noll, W. B. Peatman, *Rev. Sci. Instrum.*, **2002**, 73, 1568-1570.

139. M. Abo-Bakr, J. Feikes, K. Holldack, G. Wüstefeld, H.-W. Hübers, *Phys. Rev. Lett.*, **2002**, 88, 254801-1-4.

140. R. S. Sussmann, C. S. J. Pickles, J. R. Brandon, C. J. H. Wort, S. E. Coe, A. Wasenczuk, C. N. Dodge, A. C. Beale, A. J. Krehan, P. Dore, A. Nucara, P. Calvani, *Il Nuovo Cimento*, **1998**, 20D, 503-526.

141. M. Schmidt, U. Schade, M. Grunze, *Infrared Phys. Technol.*, **2006**, 49, 69-73.

142. M. Schmidt, N. Gierlinger, U. Schade, T. Rogge, M. Grunze, *Biopolymers*, **2006**, 83, 546-555.

143. M. Schmidt, J. S. Lee, U. Schade, M. Grunze, K. H. Kim, **2007**, submitted.

144. C. A. McCoy, J. A. de Haseth, *Appl. Spectrosc.*, **1988**, 42, 336-341.

145. B. Lary, Diploma Thesis, Universität Karslruhe and Forschungszentrum Karlsruhe, **2006**.

146. N. F. Kossova, V. G. Vorobjov, H. Büttner, W. Falta, *Jenaer Rundschau*, **1980**, 25, 233-235.

147. T. Miyazawa, *J. Polymer Sci.: Part C Polymer Symposium*, **1964**, 7, 59-84.

148. D. Wade Rafferty, J. L. Koenig, G. Magyar, J. L. West, *Appl. Spectrosc.*, **2002**, 56, 284-287.

149. G. Ellis, M. A. Gómez, C. Marco, *J. Macromol. Sci. B*, **2004**, 43, 191-206.

150. M. Schmidt *et al.*, unpublished results, manuscript in preparation.

151. G. Ellis, private communication.

152. R. M. Brown Jr., I. M. Saxena, K. Kudlicka, *Trends Plant Sci.*, **1996**, 1, 149-156.

153. M. Åkerholm, L. Salmén, *Polymer*, **2001**, 42, 963-969.

154. R. M. Brown Jr., *Pure Appl. Chem.*, **1999**, 71, 767-775.

155. S. Kimura, T. Kondo, *J. Plant Res.*, **2002**, 115, 297-302.

156. M. Jarvis, *Nature*, **2003**, 426, 611-612.

157. R. H. Atalla, D. L. VanderHart, *Science*, **1984**, 223, 283-285.

158. B. Hinterstoisser, L. Salmén, *Cellulose*, **1999**, 6, 251-263.

159. R. H. Atalla, *Am. Chem. Soc. Symp. Ser.*, **1998**, 697, 172-179.

160. M. Åkerholm, L. Salmén, *Holzforschung*, **2003**, 57, 459-465.

161. D. Fengel, G. Wegener, *Wood: chemistry, ultrastructure, reactions*; Walter de Gruyter & Co., Berlin, **1989**.

162. J. Fahlén, L. Salmén, *Biomacromolecules*, **2005**, 6, 433-438.

163. I. Burgert, J. Keckes, K. Frühmann, P. Fratzl, S. E. Tschegg, *Plant Biol.*, **2002**, 4, 9-12.

164. I. Burgert, N. Gierlinger, T. Zimmermann, *Holzforschung*, **2005**, 59, 240-246.

165. Y. Maréchal, H. Chanzy, *J. Mol. Struct.*, **2000**, 523, 183-196.

166. D. Fengel, *Holzforschung*, **1992**, 46, 283-288.

167. C. Y. Liang, R. H. Marchessault, *J. Polym. Sci.*, **1959**, 37, 385-395.

168. R. H. Marchessault, C. Y. Liang, *J. Polym. Sci.*, **1960**, 43, 71-84.

169. J. Sugiyama, J. Persson, H. Chanzy, *Macromolecules*, **1991**, 24, 2461-2466.

170. A. Šturcová, I. His, T. J. Wess, G. Cameron, M. C. Jarvis, *Biomacromolecules*, **2003**, 4, 1589-1595.

171. H. J. Marrinan, J. Mann, *J. Polym. Sci.*, **1956**, 21, 301-311.

172. Y. Hishikawa, E. Togawa, Y. Kataoka, T. Kondo, *Polymer*, **1999**, 40, 7117-7124.

173. Y. Hishikawa, S.-I. Inoue, J. Magoshi, T. Kondo, *Biomacromolecules*, **2005**, 6, 2468-2473.

174. A. Šturcová, I. His, D. C. Apperley, J. Sugiyama, M. C. Jarvis, *Biomacromolecules*, **2004**, 5, 1333-1339.

175. A. J. Michell, *Carbohydr. Res.*, **1990**, 197, 53-60.

176. A. J. Michell, *Carbohydr. Res.*, **1993**, 241, 47-54.

177. D. Fengel, *Holzforschung*, **1993**, 47, 103-108.

178. A.-M. Olsson, L. Salmén, *Carbohydr. Res.*, **2004**, 339, 813-818.

179. A. Björkman, *Cellulose Chem. Technol.*, **2002**, 36, 3-35.

180. K. Haxaire, Y. Maréchal, M. Milas, M. Rinaudo, *Biopolymers*, **2003**, 2, 10-20.

181. T. Kondo, C. Sawatari, *Polymer*, **1996**, 37, 393-399.

182. K. Wickholm, P. T. Larsson, T. Iversen, *Carbohydr. Res.*, **1998**, 312, 123-129.

183. K. Wickholm, E. L. Hult, P. T. Larsson, T. Iversen, H. Lennholm, *Cellulose*, **2001**, 8, 139-148.

184. P. P. Girard, E. A. Cavalcanti-Adam, R. Kemkemer, J. P. Spatz, *Soft Matter*, **2007**, 3, 307-326.

185. M. Schmidt, T. Wolfram, M. Rumpler, C. P. Tripp, M. Grunze, *Biointer*phases, **2007**, 2, 1-5.

186. G. D. Sockalingum, W. Bouhedja, P. Pina, P. Allouch, C. Bloy, M. Manfait, *Cell. Mol. Biol.*, **1998**, 44, 261-269.

187. M. K. Alam, J. A. Timlin, L. E. Martin, D. Williams, C. R. Lyons, K. Garrison, B. Hjelle, *Vib. Spectrosc.*, **2004**, 34, 3-11.

188. K. Maquelin, L.-P. Choo-Smith, C. Kirschner, N. A. Ngo-Thi, D. Naumann, G. J. Puppels, in *Handbook of Vibrational Spectroscopy*, edited by J. M. Chalmers and P. R. Griffiths, Wiley, Chichester, **2002**, pp. 3308-3334.

189. S. J. Parikh, J. Chorover, *Langmuir*, **2006**, 22, 8492-8500.

190. L. A. Thomson, F. C. Law, N. Rushton, J. Franks, *Biomaterials*, **1991**, 12, 37-40.

191. J. A. Cooper, *J. Cell Biol.*, **1987**, 105, 1473-1478.

192. K. P. Ishida, P. R. Griffiths, *Appl. Spectrosc.*, **1993**, 47, 584-589.

193. M. J. Romeo, B. Bird, T. Chernenko, C. Matthäus, M. Diem, 4th International Conference on Advanced Vibrational Spectroscopy, Corfu, **2007**, p. 112.

194. D. M. Shotton, *J. Cell Sci.*, **1989**, 94, 175-206.

195. N. Gierlinger, M. Schwanninger, A. Reinecke, I. Burgert, *Biomacromolecules*, **2006**, 7, 2077-2081.

196. U. Schade, private communication.

197. A. J. Sommer, 4th International Conference on Advanced Vibrational Spectroscopy, Corfu, **2007**, p. 17.

# Abbreviations

| | |
|---|---|
| ac | alternating current |
| ATCC | American Type Culture Collection |
| ATR | attenuated total reflection |
| BESSY | Berliner Elektronenspeicherring-Gesellschaft für Synchrotronstrahlung |
| dc | direct current |
| DMAc | dimethylacetamide |
| DTGS | deuterated triglycine sulfate |
| E7 | a mixture of cyanobi- and terphenyls |
| EDTA | ethylenediamine tetraacetic acid |
| iPP | isotactic polypropylene |
| IR | infrared |
| IRIS | infrared initiative synchrotron radiation |
| IRLD | infrared linear dichroism |
| IRRAS | infrared reflection-absorption spectroscopy |
| KRS-5 | thallium bromide iodide |
| LCP | liquid crystal polymer |
| MCT | mercury cadmium telluride |
| PBS | phosphate buffered saline |
| PEM | photoelastic modulator |
| Pen/Strep | penicillin/streptomycin |
| PM | polarization modulation |
| Ref. | reference |
| S/N | signal-to-noise ratio |
| SP | source power |
| TC | transcrystalline |
| UV | ultraviolet |
| VCD | vibrational circular dichroism |
| VLD | vibrational linear dichroism |

# List of Publications

L. V. Moroz, M. Schmidt, U. Schade, T. Hiroi, M. A. Ivanova, Synchrotron-based infrared microspectroscopy as a useful tool to study hydration states of meteorite constituents, *Meteorit. Planet. Sci.*, **2006**, 41, 1219-1230.

M. Schmidt, U. Schade, M. Grunze, Microspectroscopic observation of vibrational linear dichroism using polarization-modulated infrared synchrotron radiation, *Infrared Phys. Technol.*, **2006**, 49, 69-73.

M. Schmidt, N. Gierlinger, U. Schade, T. Rogge, M. Grunze, Polarized Infrared Microspectroscopy of Single Spruce Fibers: Hydrogen Bonding in Wood Polymers, *Biopolymers*, **2006**, 83, 546-555.

M. Schmidt, T. Wolfram, M. Rumpler, C. P. Tripp, M. Grunze, Live cell adhesion assay with attenuated total reflection infrared spectroscopy, *Biointer*phases, **2007**, 2, 1-5.

M. Schmidt, J. S. Lee, U. Schade, M. Grunze, K. H. Kim, Anisotropy studied by polarization-modulated Fourier-transform infrared reflection difference microspectroscopy, **2007**, submitted.

# Acknowledgements

This work would not have been possible without the support and contributions from a great number of people.

First and foremost, I am greatly indebted to my supervisor Prof. Dr. Michael Grunze for giving me the terrific opportunity to work on this research topic and the freedom to experience the various stimulating areas and places involved in this interdisciplinary project, for his continuous support throughout this work and for many helpful discussions.

I would like to thank Prof. Dr. Joachim Spatz for his kind agreement to review this dissertation.

I am deeply grateful to Dr. Ulrich Schade who made my time at BESSY a very informative, fruitful and, equally important, a very enjoyable experience which forms the core of my work.

I would like to express my gratitude to Dr. Monika Rumpler and Dr. Notburga Gierlinger from the MPI KG in Potsdam for the very pleasant, instructive and productive time we worked together.

I thank Dr. Tilmann Rogge for his very kind guidance and cooperation during my time at the IMT in the Forschungszentrum Karlsruhe.

I would like to thank Dr. Tobias Wolfram, Dr. Jörg Bewersdorf and Prof. Dr. Michael Grunze for making my stay at the IMB at the Jackson Laboratory a very memorable and pleasant experience.

I thank Dr. Jong Seok Lee and Dr. Michele Ortolani from BESSY for the very friendly and helpful collaboration.

I thank Dr. Axel Rosenhahn, Dr. Reiner Dahint, Mrs. Edeltraud Boczek, Mr. Robert Läufer and all colleagues in Heidelberg for their help and support.

I would like to thank Prof. Dr. Wolfgang Eberhardt, Prof. Dr. Peter Fratzl and Prof. Dr. Volker Saile that I could spend and enjoy my time as a guest in their research institutes.

I also thank the many colleagues and staff in Berlin, Potsdam, Karlsruhe and Bar Harbor for their support and helpful discussions.

I would also like to thank Dr. Gary Ellis from the CSIC in Madrid, Prof. Dr. Carl Tripp from the UMaine and Dr. Ljuba Moroz from the DLR for the very interesting collaborations and discussions.

Last but by no means least, I would like to thank Barbara, my parents and my grandmother for their help and encouragement.

Hiermit erkläre ich an Eides Statt, dass ich die vorliegende Dissertation selbst verfasst und mich dabei keiner anderen als der von mir bezeichneten Quellen und Hilfsmittel bedient habe. Ich habe an keiner anderen Stelle ein Prüfungsverfahren beantragt oder die Dissertation in dieser oder anderer Form bereits anderweitig als Prüfungsarbeit verwendet oder einer anderen Fakultät als Dissertation vorgelegt.

Berlin, den 27. August 2007